

## An ACA Survey of [C I] $^3P_1-^3P_0$ , CO $J=4-3$ , and Dust Continuum in Nearby U/LIRGs

TOMONARI MICHİYAMA,<sup>1,2,3</sup> TOSHIKI SAITO,<sup>4,5,3</sup> KEN-ICHI TADAKI,<sup>3</sup> JUNKO UEDA,<sup>3</sup> MING-YANG ZHUANG,<sup>1,6</sup>  
JUAN MOLINA,<sup>1</sup> BUMHYUN LEE,<sup>1</sup> RAN WANG,<sup>1,6</sup> ALBERTO BOLATTO,<sup>7</sup> DAISUKE IONO,<sup>3,8</sup> KOUICHIRO NAKANISHI,<sup>3,8</sup>  
TAKUMA IZUMI,<sup>3,8</sup> TAKUJI YAMASHITA,<sup>3</sup> AND LUIS C. HO<sup>1,6</sup>

<sup>1</sup>*Kavli Institute for Astronomy and Astrophysics, Peking University, 5 Yiheyuan Road, Haidian District, Beijing 100871, P.R.China*

<sup>2</sup>*Department of Earth and Space Science, Osaka University, 1-1 Machikaneyama, Toyonaka, Osaka 560-0043, Japan*

<sup>3</sup>*National Astronomical Observatory of Japan, National Institutes of Natural Sciences, 2-21-1 Osawa, Mitaka, Tokyo, 181-8588*

<sup>4</sup>*Max-Planck-Institut für Astronomie, Königstuhl 17, 69117 Heidelberg, Germany*

<sup>5</sup>*Department of Physics, General Studies, College of Engineering, Nihon University, 1 Nakagawara, Tokusada, Tamuramachi, Koriyama, Fukushima, 963-8642, Japan*

<sup>6</sup>*Department of Astronomy, School of Physics, Peking University, Beijing 100871, China*

<sup>7</sup>*Department of Astronomy and Laboratory for Millimeter-Wave Astronomy, University of Maryland, College Park, MD 20742, USA*

<sup>8</sup>*Department of Astronomical Science, The Graduate University for Advanced Studies, SOKENDAI, 2-21-1 Osawa, Mitaka, Tokyo 181-8588*

(Accepted July 28, 2021)

Submitted to ApJS

### ABSTRACT

We present the results of surveying [C I]  $^3P_1-^3P_0$ ,  $^{12}\text{CO } J=4-3$ , and 630  $\mu\text{m}$  dust continuum emission for 36 nearby ultra/luminous infrared galaxies (U/LIRGs) using the Band 8 receiver mounted on the Atacama Compact Array (ACA) of the Atacama Large Millimeter/submillimeter Array. We describe the survey, observations, data reduction, and results; the main results are as follows. (i) We confirmed that [C I]  $^3P_1-^3P_0$  has a linear relationship with both the  $^{12}\text{CO } J=4-3$  and 630  $\mu\text{m}$  continuum. (ii) In NGC 6052 and NGC 7679,  $^{12}\text{CO } J=4-3$  was detected but [C I]  $^3P_1-^3P_0$  was not detected with a [C I]  $^3P_1-^3P_0$  /  $^{12}\text{CO } J=4-3$  ratio of  $\lesssim 0.08$ . Two possible scenarios of weak [C I]  $^3P_1-^3P_0$  emission are C<sup>0</sup>-poor/CO-rich environments or an environment with an extremely large [C I]  $^3P_1-^3P_0$  missing flux. (iii) There is no clear evidence showing that galaxy mergers, AGNs, and dust temperatures control the ratios of [C I]  $^3P_1-^3P_0$  /  $^{12}\text{CO } J=4-3$  and  $L'_{[\text{CI}](1-0)} / L_{630\mu\text{m}}$ . (iv) We compare our nearby U/LIRGs with high- $z$  galaxies, such as galaxies on the star formation main sequence (MS) at  $z \sim 1$  and submillimeter galaxies (SMGs) at  $z = 2 - 4$ . We found that the mean value for the [C I]  $^3P_1-^3P_0$  /  $^{12}\text{CO } J=4-3$  ratio of U/LIRGs is similar to that of SMGs but smaller than that of galaxies on the MS.

**Keywords:** Galaxy evolution (594), Extragalactic astronomy (506), Submillimeter astronomy (1647), Starburst galaxies (1570), Luminous infrared galaxies (946), Ultraluminous infrared galaxies (1735), Galaxy collisions (585), Interstellar medium (847), Interstellar line emission (844), CO line emission (262)

### 1. INTRODUCTION

The molecular hydrogen gas mass ( $M_{\text{H}_2}$ ) of galaxies is a fundamental observable quantity that is directly linked to galaxy evolution. As cold  $\text{H}_2$  does not radiate strong emission, astronomers use carbon monoxide

(CO<sup>1</sup>) as a tracer of the extragalactic cold molecular gas mass (e.g., Bolatto et al. 2013). The  $J=1-0$  ground rotational transition of CO (hereafter CO (1–0)) has low excitation energy and the emission falls in the transparent atmospheric window (at a frequency of 115 GHz and a wavelength of 2.6 mm). For high- $z$  galaxies, the observed frequency of low- $J$  CO lines is shifted out of

Corresponding author: Tomonari Michiyama  
t.michiyama.astr@gmail.com

<sup>1</sup> We use the term “CO” to infer  $^{12}\text{C}^{16}\text{O}$  throughout this paper.

the main high-transparency atmospheric window (i.e.,  $< 80$  GHz) and we cannot use powerful telescopes – such as the Atacama Large Millimeter/submillimeter Array (ALMA) – to observe low- $J$  CO lines until the lowest frequency band of ALMA (band 1) becomes available in the near future. Therefore, detecting low- $J$  CO lines requires long integration radio observation, even for bright objects (e.g., Carilli & Walter 2013). We thus need to develop alternative methods to measure  $M_{\text{H}_2}$ , which can be observed at a higher frequency (shorter wavelength) than CO (1–0) emission.

One possible method is to observe the mid- and high- $J$  CO lines ( $J_{\text{upper}} \geq 4$ ) (e.g., Solomon & Vanden Bout 2005; Carilli & Walter 2013). For example, CO (4–3) line emits at a frequency of 460 GHz (corresponding to a wavelength of  $650 \mu\text{m}$ ). However, higher- $J$  CO lines are sensitive to highly excited gases (i.e., warm and dense) that would occupy a minor fraction of the total molecular mass. The assumption of the line ratios, that is, CO (4–3)/CO (1–0), makes non-negligible systematic errors to measure the bulk of the molecular gas using higher- $J$  CO lines (e.g., Carilli & Walter 2013). Therefore, astronomers have developed various alternative methods.

One proposed method is to use the lower forbidden  $^3P$  fine structure line of atomic carbon – i.e., [C I]  $^3P_1 - ^3P_0$ , hereafter referred to as [C I] (1–0) – which emits at a frequency of 492 GHz (corresponding to a wavelength of  $609 \mu\text{m}$ ). For example, [C I] observations in Galactic clouds have shown that [C I] distributions coincide with those of CO (Ojha et al. 2001; Oka et al. 2001; Ikeda et al. 2002; Kramer et al. 2008; Burton et al. 2015; Izumi et al. 2020a), suggesting that [C I] (1–0) luminosity can trace the bulk of molecular gas. Besides, Israel & Baas (2001, 2002, 2003) reported bright [C I] emission at the center of nearby galaxies. Papadopoulos et al. (2004) proposed that [C I] is superior to CO for measuring  $M_{\text{H}_2}$ , especially in the UV intense diffuse region ( $\sim 10^2 - 10^3 \text{ cm}^{-3}$ ) and/or metal-poor environments due to the dissociation of CO. Subsequently, Papadopoulos & Greve (2004) applied the [C I] method for two Ultra/ infrared luminous galaxies: U/LIRGs – Arp 220 and NGC 1614 – and demonstrated that the molecular gas mass inferred from [C I] (1–0) luminosity is consistent with that from CO observations. Many studies have investigated the [C I] properties of galaxies using the data obtained by the Herschel Space Observatory (e.g., Israel et al. 2015; Kamenetzky et al. 2016; Jiao et al. 2017; Jiao et al. 2019; Crocker et al. 2019). Theoretical modeling suggests that [C I] is a better tracer of  $M_{\text{H}_2}$  than CO (1–0) in several environments, such as metal-poor environments or those with a high-cosmic

rays, and active galactic nuclei (AGNs) (e.g., Bisbas et al. 2015; Papadopoulos et al. 2018; Clark et al. 2019). More recently, high-frequency receivers (e.g., Band 8 and 10 receivers) on ALMA have also enabled investigation of the spatial distribution of atomic carbon in nearby galaxies (e.g., Krips et al. 2016; Ciccone et al. 2018; Izumi et al. 2018; Miyamoto et al. 2018; Salak et al. 2019; Izumi et al. 2020b; Saito et al. 2020). In addition, [C I] measurements of bright high- $z$  galaxies, such as gravitational lensing galaxies and submillimeter galaxies (SMGs) (e.g., Walter et al. 2011; Alaghband-Zadeh et al. 2013; Bothwell et al. 2017; Yang et al. 2017; Andreani et al. 2018; Cañameras et al. 2018; Harrington et al. 2018; Tadaki et al. 2018; Dannerbauer et al. 2019; Jin et al. 2019; Cortzen et al. 2020), and galaxies on main sequence (MS; e.g., Popping et al. 2017; Talia et al. 2018; Valentino et al. 2018; Bourne et al. 2019; Valentino et al. 2020; Lee et al. 2021) are increasingly available.

The other proposed method uses the submillimeter dust continuum emission (Eales et al. 2012; Magdis et al. 2012; Scoville et al. 2014). Scoville et al. (2016) derived the same empirical calibration constant from 350 GHz ( $\lambda = 850 \mu\text{m}$ ) continuum flux to the interstellar medium (ISM) mass among local star-forming galaxies, molecular clouds of the Milky Way, and high-redshift SMGs; this suggests that the Rayleigh-Jeans tail of the dust emission can be used as an accurate and very efficient probe of the ISM in galaxies.

Before applying these new methods to measure  $M_{\text{H}_2}$  in high- $z$  galaxies, it is necessary to investigate the experimental relationship between CO, [C I], and the dust continuum in well-studied nearby galaxies. For example, Michiyama et al. (2020) discovered a [C I]-faint CO-bright gas-rich galaxy (NGC 6052), implying a large galaxy-to-galaxy variation with respect to the [C I]/CO ratio and the importance of a systematic comparison between CO and [C I]. Here, we expand the analysis of Michiyama et al. (2020) by a survey of [C I] (1–0), CO (4–3), and dust continuum in U/LIRGs, using the Band 8 receiver mounted on the Atacama Compact (Morita) Array (ACA). This project can improve the sensitivity and resolution of legacy Herschel results in terms of the higher sensitivity and the higher resolution (i.e., Herschel’s beam is  $\sim 45''$  and the sensitivity is  $\sim 0.5 \text{ mJy}$  whereas ACA’s beam is  $\sim 3''$  and the sensitivity is  $\sim 0.05 \text{ mJy}$ ).

In Section 2, we describe the survey design, supplemental data, observation, data reduction and data analysis. In Section 3, we summarize the results of the survey. In Section 4, we investigate the correlation between [C I] (1–0), CO (4–3), and the dust continuum.

In addition, the details of [C I]-faint CO-bright gas-rich galaxy, NGC 7679, are explained. We investigated whether AGNs, mergers, and dust temperatures control the ratio of [C I]/CO. Finally, we compare our nearby U/LIRGs and high- $z$  galaxies ( $z \sim 1$  galaxies on MS and  $z = 2 - 4$  SMGs). Section 5 provides a summary of the study. We use the cosmological parameters for a  $\Lambda$ CDM,  $H_0 = 67.8$ ,  $\Omega_m = 0.308$ , and  $\Omega_\Lambda = 0.692$  (Planck Collaboration et al. 2016).

## 2. SURVEY

### 2.1. Sample Selection

The ACA Band 8 U/LIRG survey was designed to observe [C I] (1–0), CO (4–3), and dust continuum emission for nearby ultraluminous infrared galaxies (ULIRGs:  $10^{12} L_\odot < L_{\text{TIR}} < 10^{13} L_\odot$ ) and luminous infrared galaxies (LIRGs:  $10^{11} L_\odot < L_{\text{TIR}} < 10^{12} L_\odot$ ), where the  $L_{\text{TIR}}$  is the total infrared luminosity integrated from 8–1000  $\mu\text{m}$ . We observed 36<sup>2</sup> U/LIRGs. We selected 12 ULIRGs<sup>3</sup> from the IRAS Revised Bright Galaxy Sample (Sanders et al. 2003), whose declinations were below 20 degrees and exhibited no strong atmospheric absorption around [C I] (1–0) or CO (4–3). We selected 24 LIRGs, from which CO (1–0) was detected in literature by cross-matching the CO (1–0) samples compiled by Kamenetzky et al. (2016) and the references therein. The list of targets is listed in Table A.1.

### 2.2. Supplemental data

Several galaxies were observed using the Spectral and Photometric Imaging Receiver Fourier Transform Spectrometer (SPIRE/FTS) mounted on the Herschel Space Observatory (Kamenetzky et al. 2016; Lu et al. 2017), which provides the total [C I] (1–0) and CO (4–3) flux. The galaxy-integrated global properties such as SFR, dust mass ( $M_{\text{dust}}$ ), dust temperature ( $T_{\text{dust}}$ ), and  $L_{\text{TIR}}$  were estimated based on continuum spectrum fitting (SED fitting) by Shangguan et al. (2019)<sup>4</sup>. The CO (1–0) velocity integrated flux obtained by single dish telescopes was compiled by Kamenetzky et al. (2016), which corresponds to a 45'' aperture after aperture correction. The supplemental information is summarized

in Table A.2

A histogram of the SFRs of the sample sources is presented in Figure 1.

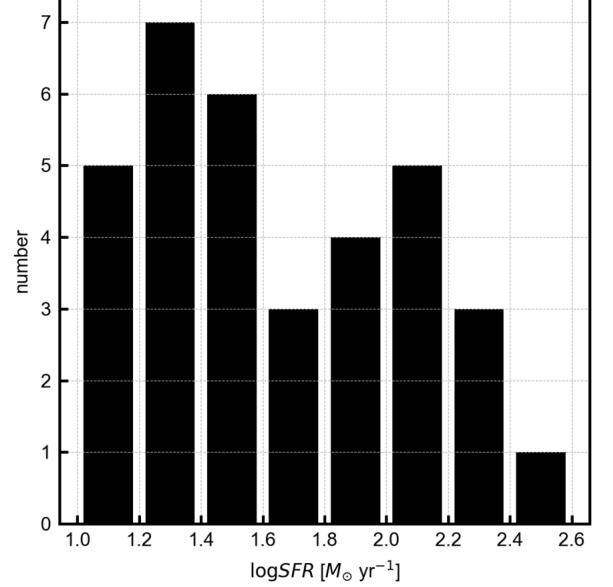


**Figure 1.** A histogram of SFR for our ACA Band 8 U/LIRGs survey.

### 2.3. Observation

Single pointing mode ACA observations were performed during the cycle 6 season (ALMA project ID: 2018.1.00994.S, PI: T.Michiyama). For NGC 232, IRAS F10565+2448, and ESO 069-IG006, the fainter pairs of the interacting system were also observed. Among the 36 U/LIRGs, only CO (4–3) observations were completed in NGC 5990 and IRAS 19542+1110 and only [C I] (1–0) observations were completed in UGC 02982. The details – e.g., date, typical system temperature, and the number of antennas – are summarized in Table A.3, which are based on QA0 reports provided by the ALMA observatory. The detailed information in each observation run is shown in the weblog provided by the ALMA observatory.

Most important are the small field of view (FoV) and small maximum recovery scale (MRS) because the observation was a single-point snapshot ( $\sim 5$  min integration) without a total power array. The FoV is defined as:

$$\text{FoV} = 1.13 \frac{\lambda_{\text{sky}}}{D_{\text{ant}}}, \quad (1)$$

<sup>2</sup> We observed 39 U/LIRGs, however, we do not investigate UGC 02338, IRAS 05442+1732, and NGC 7771. In the case of UGC 02338 and IRAS 05442+1732, the target information were wrong due to artificial mistake. For NGC 7771, the final images were uncertain due to technical issues and it was considered as QA2 fail from observatory.

<sup>3</sup> NGC 6240 satisfies our criteria but was not observed due to duplication issue.

<sup>4</sup>  $T_{\text{dust}}$  and  $L_{\text{TIR}}$  is estimated with the same method explained in Shangguan et al. (2019) in private communication.





for lines and

$$S_{\text{cont}} < 3 \times \sigma_{\text{cont}} \sqrt{\frac{N_S}{N_B}} \quad (5)$$

for continuum emission, where  $\sigma_{\text{ch}}$  is the RMS level of the channel map,  $\Delta V_{\text{ch}}$  is the velocity resolution,  $N_{\text{ch}} = \text{FWHM}/\Delta V_{\text{ch}}$ ,  $N_S$  is the the number of pixels for the source size, and  $N_B$  is the number of pixels for the synthesized beam. The equations are from [Hainline et al. \(2004\)](#). If CO (4–3) is detected and [C I] (1–0) is not, we assume that  $N_{\text{ch}}$  and  $N_S$  of [C I] (1–0) are the same as CO (4–3), where  $N_{\text{ch}}$  and  $N_S$  are calculated based on the FWHM value of the velocity width and source size measured in Table A.5. If both CO (4–3) and [C I] (1–0) are not detected, we assume that the FWHM of line width is  $150 \text{ km s}^{-1}$  and  $N_S = 3 \times N_B$ . However, these upper limits were not included in the discussion section. We note that some [C I] (1–0) emission is on the edge of the spectral window because of the incorrect redshift entered in observation requests in some galaxies (e.g., IRAS F05189-2524). In this case, we assume the same line profile as CO (4–3) to calculate the total [C I] (1–0) flux.

### 3.2. Missing Flux

As explained in Section 2.3, the ACA single-point observation without the total power array may not cover the total flux. In Table A.5, the SPIRE/FTS velocity integrated [C I] (1–0) and CO (4–3) fluxes from [Kamenetzky et al. \(2016\)](#) are listed if accessible. The typical ACA RF is approximately  $\sim 59 \%$  and  $\sim 69 \%$  for [C I] (1–0) and CO (4–3), respectively. The CO (4–3) and [C I] (1–0) lines are close enough in frequency that they are both observed with similar uv-coverage, tracing similar spatial scales in the sample galaxies. Therefore, we argue that the resultant line ratios between CO (4–3) and [C I] (1–0) provided here are a reasonable representation of the line ratios, despite the missing flux of order 30-40%. The extrapolated total dust continuum flux densities are listed in Table A.6, whenever the dust mass was estimated in [Shangguan et al. \(2019\)](#)<sup>6</sup>. We found that the typically RF for continuum emission was 46 % and 52 %, for the 609 and 650  $\mu\text{m}$  continuum flux density, respectively. The RF for individual galaxies is derived from the ratio between the continuum flux density by the ACA and continuum spectrum fitting. The typical RF suggests that almost half of the continuum flux density comes outside the FoV or from a structure that is larger than MRS. We note that the SPIRE

beam is  $45''.5$  at the CO (4–3) transition but the ACA FoV is  $23''.5$  (shown as magenta circles in Figure A.1). Therefore, a large missing flux might be observed, especially, for galaxies with small luminosity distances (e.g.,  $D < 100 \text{ Mpc}$ ). The individual notes for galaxies that have a large missing flux (e.g., IC 4280) are given in Section A.3.

### 3.3. Luminosity

The luminosities for the lines are measured using

$$L_{\text{line}} [L_{\odot}] = 1.04 \times 10^{-3} S_{\text{line}} \Delta v \nu_{\text{rest}} (1+z)^{-1} D_L^2 \quad (6)$$

and

$$L'_{\text{line}} [\text{K km s}^{-1} \text{ pc}^2] = 3.25 \times 10^7 S_{\text{line}} \Delta v \nu_{\text{obs}}^{-2} (1+z)^{-3} D_L^2, \quad (7)$$

where  $\nu_{\text{rest}}$  is the rest frequency of the line emission in GHz,  $z$  is the redshift,  $D_L$  is the luminosity distance in Mpc, and  $\nu_{\text{obs}} = \nu_{\text{rest}}/(1+z)$  is the sky (observed) frequency in GHz ([Solomon & Vanden Bout 2005](#)). We used  $L'_{\text{line}}$  to calculate the molecular gas mass (Section A.4) and  $L_{\text{line}}$  for the photodissociation region (PDR) modeling (Section 4.3).

The ACA continuum flux density at the rest frames of 609  $\mu\text{m}$  and 650  $\mu\text{m}$  ( $S_{609}$  and  $S_{650}$ ) are converted to the 630  $\mu\text{m}$  specific luminosity  $L_{\nu(630\mu\text{m})}$  based on a formulation in [Scoville et al. \(2016\)](#),

$$L_{\nu(630\mu\text{m})} [\text{erg s}^{-1} \text{ Hz}^{-1}] = (1.19 \times 10^{27}) \times \left( \frac{\nu_{630\mu\text{m}}}{\nu_{\text{obs}}(1+z)} \right)^{3.8} \times \frac{D_L^2}{(1+z)} \times \frac{\Gamma_{\text{RJ}}(T_{\text{dust}}, \nu_{630\mu\text{m}}, 0)}{\Gamma_{\text{RJ}}(T_{\text{dust}}, \nu_{\text{obs}}, z)} \times S_{\nu}. \quad (8)$$

where  $S_{\nu}$  is  $(S_{609} + S_{650})/2$  in Jy and  $\nu_{\text{obs}}$  is the average of the red-shifted sky frequency<sup>7</sup>. If either  $S_{609}$  or  $S_{650}$  were detected, we used the flux density and frequency of the detected signal. We assume the dust temperature of  $T_{\text{dust}} = 25 \text{ K}$  for simple analyses.  $\Gamma_{\text{RJ}}$  is the correction for departure in the rest frame of the Planck function from Rayleigh–Jeans given by

$$\Gamma_{\text{RJ}}(T_{\text{dust}}, \nu, z) = \frac{h\nu(1+z)/kT_{\text{dust}}}{e^{h\nu(1+z)/kT_{\text{dust}}} - 1}. \quad (9)$$

The derived luminosities are listed in Table A.7. The ratios among the derived luminosities are listed in Table A.8.

<sup>6</sup> Dust continuum fluxes are provided by Jinyi Shangguan in private communication.

<sup>7</sup> The red-shifted sky frequencies are labeled in Figure A.1(d) and (h).

### 3.4. Molecular gas mass

We supplementally estimated  $M_{\text{H}_2}$  from CO (1–0), [C I] (1–0), CO (4–3), and the continuum, respectively (See detail in Section A.4 and Table A.9). We assumed a simple luminosity-to- $M_{\text{H}_2}$  conversion factor. We note that the main purpose of this study is not to investigate the effect of the systematic uncertainties introduced by the various assumptions when estimating  $M_{\text{H}_2}$ .

## 4. DISCUSSION

Figure 2 shows the relationship between [C I] (1–0), CO (4–3), and 630  $\mu\text{m}$  continuum luminosities. The linear regression lines (gray lines) for detected galaxies were calculated using the PYTHON package of `linmix` developed by Kelly (2007). Minimum, maximum, average, median, and standard errors of the  $L_{[\text{CI}](1-0)}/L_{\text{CO}(4-3)}$ ,  $L_{630\mu\text{m}}/L'_{[\text{CI}](1-0)}$ , and  $L_{630\mu\text{m}}/L'_{\text{CO}(4-3)}$  in our targets are shown in Table 1. The correlations are naturally explained because  $L'_{[\text{CI}](1-0)}$ ,  $L'_{\text{CO}(4-3)}$ , and  $L_{630\mu\text{m}}$  could be used to measure  $M_{\text{H}_2}$  (Section A.4). The scatter for the correlations could reflect the systematic uncertainties introduced by the various assumptions when measuring  $M_{\text{H}_2}$ . Figure 2 (a) shows that the upper limits for the non-detections, i.e.,  $L'_{[\text{CI}](1-0)}/L'_{\text{CO}(4-3)} < 0.08$  in NGC 6052 and  $L'_{[\text{CI}](1-0)}/L'_{\text{CO}(4-3)} < 0.08$  for NGC 7679 is  $> 4$  times smaller than the typical  $L'_{[\text{CI}](1-0)}/L'_{\text{CO}(4-3)}$  ratio of 0.34 (see Section 4.1 in detail). In Section 4.2, we further investigate a diverse range of galaxies in terms of  $L'_{[\text{CI}](1-0)}/L'_{\text{CO}(4-3)}$  and  $L'_{[\text{CI}](1-0)}/L_{630\mu\text{m}}$ .

Figure 3 shows the FWHM of the [C I] (1–0) and CO (4–3) line profiles. In most case, the line shapes of [C I] (1–0) and CO (4–3) lines and `mom1` and `mom2` maps appear similar (Figure A.1), implying that the kinematical properties of the [C I] (1–0) and CO (4–3) are the same for molecular gas distributions at the  $\sim\text{kpc}$  scale. We manually selected galaxies used in Figure 3, which can be well fitted by single Gaussian components (i.e., the used spectra are marked in Figure A.1.) For example, we do not include NGC 232-2 (NGC 235) because the S/N of the spectrum is low. We also avoid double peak emission, because a single Gaussian fitting may not work well (e.g., IC4280). However, this manual selection did not impact the results of this study.

### 4.1. [C I] non-detection

ALMA/ACA recently identified a galaxy, NGC 6052 (Michiyama et al. 2020), which may be a counterexample to the recent concept of the ubiquitous [C I]/CO distribution during the cloud lifetime and the C<sup>0</sup>-rich/CO-poor region due to the CO dissociation process, proposed by e.g., Papadopoulos et al. (2004, 2018). During

**Table 1.** Summary of statistics for the ratios between [C I] (1–0), CO (4–3) and 630  $\mu\text{m}$

	min,max	ave	med	SE	$N$
$L_{[\text{CI}](1-0)}/L_{\text{CO}(4-3)}$	0.1,1.5	0.5	0.4	0.05	31
$F_{[\text{CI}](1-0)}^{\text{P}}/F_{\text{CO}(4-3)}^{\text{P}}$	0.2,1.1	0.4	0.4	0.05	20
$L'_{[\text{CI}](1-0)}/L_{630\mu\text{m}} \times 10^{-22}$	0.6,7	3.3	3.6	0.3	32
$F_{[\text{CI}](1-0)}^{\text{P}}/S_{609}$	1.3,37	9.8	7.7	1.6	27
$L'_{\text{CO}(4-3)}/L_{630\mu\text{m}} \times 10^{-22}$	1.6,21	9.1	8.1	0.9	32
$F_{\text{CO}(4-3)}^{\text{P}}/S_{650}$	4.9,63	31	26	3.0	32

NOTE—the minimum (min), maximum (max), average (ave), median (med), and standard error (SE=SD/ $\sqrt{N}$ , where SD is the standard deviation and  $N$  is the sample size) of each combination of the ratios. Non-detection cases are included in the median calculation; however, the other statistics are calculated without non-detection cases.  $F^{\text{P}}$  indicates the peak flux density (in the unit of Jy) calculated by Gaussian spectrum line fitting (Figure A.1). The units of  $L_{\text{line}}$ ,  $L'_{\text{line}}$ ,  $L_{630\mu\text{m}}$ , and  $S_{\text{cont}}$ , are  $L_{\odot}$ , K km s<sup>−1</sup> pc<sup>2</sup>, erg s<sup>−1</sup> Hz<sup>−1</sup>, and Jy, respectively.

this survey, we further discovered the [CI] non-detection case of gas-rich type 2 AGN, NGC 7679. Figure 4 shows that the upper limits of [C I] are small when we compare the global properties of galaxies, i.e.,  $M_{\text{dust}}$ , SFR, and  $L'_{\text{CO}(1-0)}$ , demonstrating that NGC 6052 and NGC 7679 are candidates for the [C I]-dark galaxies. Two possible scenarios of weak [C I] (1–0) emission are C<sup>0</sup>-poor/CO-rich environments or an environment with an extremely large [C I] (1–0) missing flux. A direct comparison of [C I] and CO in the same uv-plane is necessary to distinguish between these two scenarios.

If the C<sup>0</sup>-poor/CO-rich scenario is true, we may be able to use the [C I]-deficit to identify young starbursts (suggested in NGC 6052; Michiyama et al. 2020). Young starbursts are also observed in NGC 7679 as well. For example, Gu et al. (2001) detected clear higher-order Balmer absorption lines implying the presence of active star-forming regions in the central  $2'' \times 2''$  region. By modeling the spectrum, they found that young ( $< 10$  Myr) and intermediate ( $\sim 100$  Myr) stellar age populations are dominant in the nuclear region of NGC 7679. In addition, Gu et al. (2001) compared the UV spectra of NGC 7679 and NGC 5135. Among our samples, NGC 7679 showed the smallest  $L_{[\text{CI}](1-0)}/L_{\text{CO}(4-3)}$  of  $< 0.08$ , and NGC 5135 has the largest  $L_{[\text{CI}](1-0)}/L_{\text{CO}(4-3)}$  of  $1.1 \pm 0.48$ . Gu et al. (2001) demonstrated that the stellar wind absorption line, such as the P-Cygni profile of C IV  $\lambda 1550$ , is more significant in NGC 7679 than that in NGC 5135; this also sug-

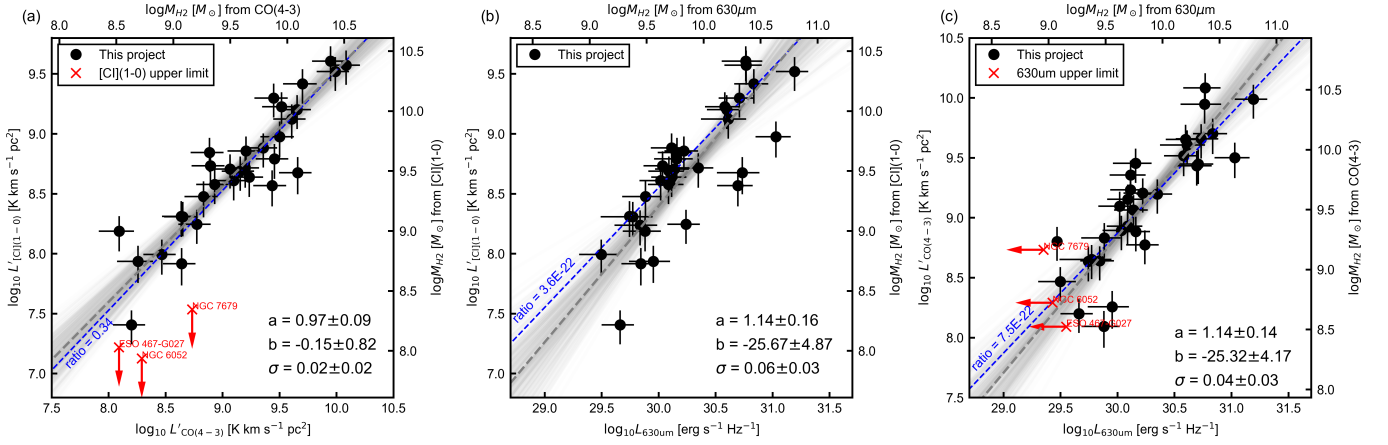


**Figure 2.** The relation between luminosities of (a) CO (4–3) and [C I] (1–0), (b) 630  $\mu\text{m}$  and [C I] (1–0), and (c) 630  $\mu\text{m}$  and CO (4–3) obtained by this project. The top and right-hand axes of each panel supplementally display the data in terms of  $M_{\text{H}_2}$  estimated in Section A.4. In each panel, the blue-dashed line indicates the median of the ratio between both quantities. The median is calculated including non-detection galaxies. The linear regression lines (grey lines) for detected galaxies are calculated by the PYTHON package `linmix` developed by Kelly (2007). The grey-dashed indicates the best fit. The grey translucent lines indicate samples from the posterior distribution. The  $a$  and  $b$  values for the fitting results ( $y = ax + b$ ) and the intrinsic scatter ( $\sigma$ ) are shown at the right bottom corner. The red arrows indicate the upper limits in the case of [C I] (1–0) and 630  $\mu\text{m}$  non-detection.

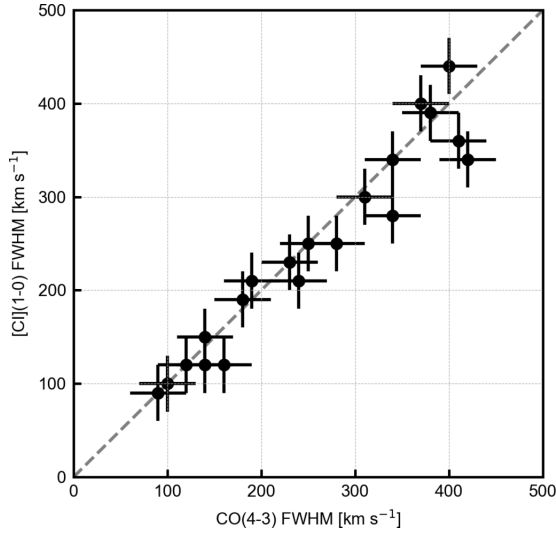


**Figure 3.** The FWHM of [C I] (1–0) and CO (4–3) line profiles. A constant  $1\sigma$  error of  $30 \text{ km s}^{-1}$  is applied. The grey dashed line has a slope of unity.

gests the younger stellar population in NGC 7679 than NGC 5135 while both galaxies host type 2 AGNs. The nuclear starburst activity in NGC 7679 may be related to the tidal interaction with NGC 7682 (with a separation of  $\sim 90 \text{ kpc}$ ). The keywords “galaxy interaction” and “young starburst” are common among NGC 7679 and NGC 6052 (Michiyama et al. 2020), whose [C I] (1–0) was not detected in our survey. The “[C I]-deficit” would be a hint to understand the timescale triggered by a galaxy interaction.

If an extremely large [C I] (1–0) missing flux scenario is true (i.e.,  $> 90\%$  of [C I] (1–0) flux is resolved out / outside the FoV). This implies that [C I] is not associated with the compact molecular gas, which is a direct material for star formation. In this case, [C I] emission may be associated with atomic hydrogen (H I) rather than with the molecular ( $\text{H}_2$ ) phase. If the spatial structure is completely different between CO and [C I], the comparison with dust distributions traced by the Band 8 continuum and HI high-resolution map – which are accessible by cm telescopes (e.g., Very Large Telescope) – are important for comprehensively understanding the different gas phases traced by CO/C I/H I and dust.

#### 4.2. What controls [C I] luminosities in galaxies?

In this section, we attempt to determine the cause of the variation in  $L'_{[\text{C I}](1-0)}/L'_{\text{CO}(4-3)}$  and  $L'_{[\text{C I}](1-0)}/L'_{630\mu\text{m}}$ . In particular, we investigate the effects of galaxy merger activities, AGN, and dust temperature. In this section, we conclude that observed [C I] luminosities are not correlated with the inferred mergers/AGNs and  $T_{\text{dust}}$ . The details are as follows.

##### 4.2.1. Galaxy merger

Galaxy mergers are one possible event that affects [C I]/CO ratio. For example, Michiyama et al. (2020) show that the small [C I]/CO line ratio in NGC 6052 is possibly due to the dense gas compressed at the collision front. In addition, the other [C I] non-detected galaxy, NGC 7679, also shows a young starburst, pos-

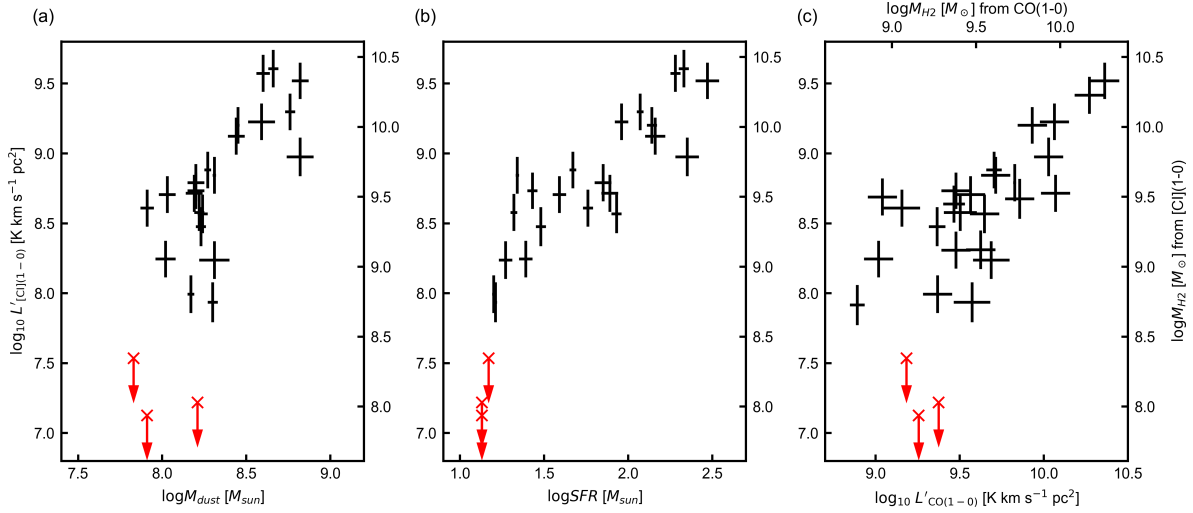


**Figure 4.** The relation between [C I] (1–0) luminosity and global properties of galaxies, i.e., (a)  $M_{\text{dust}}$ , (b) SFR, and (c) CO (1–0) luminosity.

sibly triggered by a galaxy interaction (see details in Section 4.1). Therefore, a small [C I]/CO ratio may be common in merging galaxies. We apply the selection criteria of merging galaxies used in Shanguan et al. (2019) and used a t-test between the merger and non-merger groups (Figure 5a). There was no significant difference in the mean values of  $L'_{[\text{C I}](1-0)}/L'_{\text{CO}(4-3)}$  and  $L'_{[\text{C I}](1-0)}/L_{630\mu\text{m}}$  between merger and non-merger groups, suggesting that a merger process may not be a significant factor for controlling the [C I]/CO ratio. In the case of NGC 6052 and NGC 7679, we may see a very rare phase (e.g., very young starburst) during the merger process.

#### 4.2.2. AGN

AGN is a possible event that affects the [C I]/CO ratio. For example, Meijerink & Spaans (2005) and Meijerink et al. (2007) demonstrated that the abundance of atomic carbon relative to CO will increase due to CO dissociation in X-ray dominated regions (XDRs), where strong X-rays from the central AGN control the chemical and physical properties of the ambient gas. In addition, Izumi et al. (2020b) have investigated the [C I] and CO distribution around the AGN of NGC 7469 with  $\sim 100$  pc resolution and found that the [C I] (1–0)/ $^{12}\text{CO}$  (2–1) ratio was 20 times higher around the AGN than the starburst ring outside; this indicates that [C I] enhancement can be used to identify dust-obscured AGNs. They believed that an elevated  $\text{C}^0/\text{CO}$  ratio (as expected in the XDR models) is required to explain the [C I]-enhancement.

We applied the AGN selection criteria used by Shanguan et al. (2019) to identify AGNs among our ob-

served nearby U/LIRGs. We used a t-test to determine if there was a significant difference ( $p < 0.05$  or not) between the mean values ( $L'_{[\text{C I}](1-0)}/L'_{\text{CO}(4-3)}$  and  $L'_{[\text{C I}](1-0)}/L_{630\mu\text{m}}$ ) of the AGN and non-AGN groups (Figure 5b). There is no significant difference between the AGNs and non-AGN for  $L'_{[\text{C I}](1-0)}/L'_{\text{CO}(4-3)}$  and  $L'_{[\text{C I}](1-0)}/L_{630\mu\text{m}}$ . We note that our ACA spatial resolution is  $\sim 1$  kpc. To understand the AGN properties, we need to achieve a higher resolution, as in Izumi et al. (2020b). For example,  $L_{[\text{C I}](1-0)}/L_{\text{CO}(4-3)}$  is  $0.19 \pm 0.08$  for NGC 7469 in our survey, which is below the average value of observed galaxies. This suggests that AGN enhances the [C I]/CO ratio on a small scale ( $\sim 100$  pc), but AGN cannot control the ratio in star-forming regions outside ( $>1$  kpc). A higher spatial resolution is necessary to understand the [C I] properties of AGNs.

#### 4.2.3. Dust temperature

As explained in equation (A3), the conversion from continuum flux density to  $M_{\text{H}_2}$  depends on the assumption of the dust temperature (i.e.,  $\Gamma$  in equation 9 depends on dust temperature). For example, assuming  $T_{\text{dust}} = 20$  K, the value of  $M_{\text{H}_2}$  is approximately 1.1 times higher than that assuming  $T_{\text{dust}} = 40$  K in equation (A3). Therefore, the line-to-continuum ratio may depend on the dust temperature. Figure 5(c2) shows that there is no evidence that the dust temperature controls the ratios of  $L'_{[\text{C I}](1-0)}/L_{630\mu\text{m}}$ , suggesting that the dust temperature (i.e., conversion from  $630\mu\text{m}$  to  $850\mu\text{m}$ ) is not the main systematic error in equation (A3).

Conversely, Figure 5(c1) suggests a negative relationship (i.e., lower  $T_{\text{dust}}$  may indicate higher  $L'_{[\text{C I}](1-0)}/L'_{\text{CO}(4-3)}$ ,  $p = 0.04$ ). This indicates that the excitation of [C I] and/or CO may be related to dust



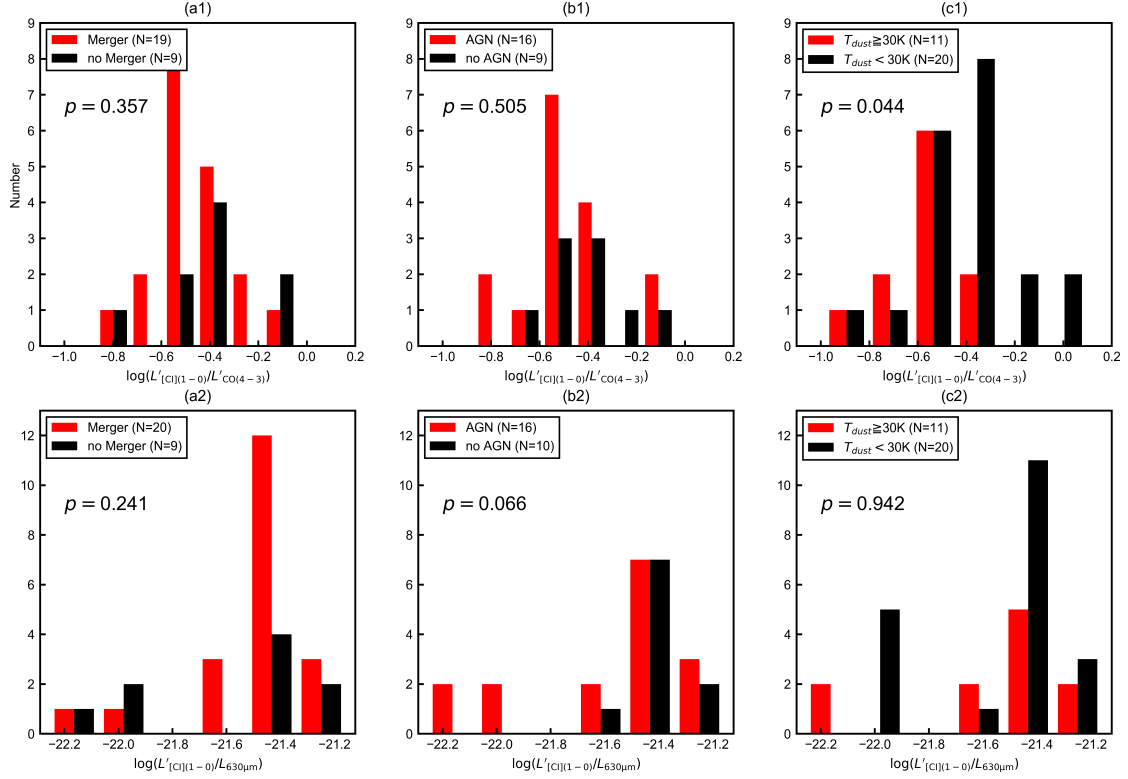


**Figure 5.** (left) The distribution of (a1)  $L'_{[\text{CII}](1-0)}/L'_{\text{CO}(4-3)}$  and (a2)  $L'_{[\text{CII}](1-0)}/L_{630\mu\text{m}}$  for merger (red) and non-merger (black) galaxies. The p-value of the t-test between mergers and non-mergers is shown in each panel. There was no significant difference between mergers and non-mergers in each plot. (middle) The distribution of (b1)  $L'_{[\text{CII}](1-0)}/L'_{\text{CO}(4-3)}$  and (b2)  $L'_{[\text{CII}](1-0)}/L_{630\mu\text{m}}$  for AGNs (red) and non-AGNs (black), respectively. There is no significant difference between AGNs and non-AGNs in each plot. (right) The distribution of (c1)  $L'_{[\text{CII}](1-0)}/L'_{\text{CO}(4-3)}$  and (c2)  $L'_{[\text{CII}](1-0)}/L_{630\mu\text{m}}$  for galaxies with  $T_{\text{dust}} \geq 30$  K (red) and  $T_{\text{dust}} < 30$  K (black), respectively. The p-value of the t-test between high- and low-dust temperature is shown in each panel. There is possibly a negative relationship (i.e., lower  $T_{\text{dust}}$  may indicate higher  $L'_{[\text{CII}](1-0)}/L'_{\text{CO}(4-3)}$ ,  $p = 0.044$ ) in panel (c1).

temperature. For example, a positive correlation is seen between  $T_{\text{dust}}$  and CO or [C I] excitation conditions in spatially resolved studies in very nearby galaxies (i.e.,  $D_L < 20$  Mpc, Koda et al. 2020; Jiao et al. 2019), and a positive correlation was observed between  $T_{\text{dust}}$  and the [C I] excitation temperatures that is estimated based on [C I] (2–1)/[C I] (1–0) ratio (Jiao et al. 2019). However, the range of  $T_{\text{dust}}$  and the number of samples are limited in our analysis and a further complete survey, including multi-[C I] and CO transitions by ALMA, is necessary to understand the CO and [C I] excitation condition.

#### 4.3. Comparison with high- $z$ galaxies

The secondary aim of this study was to compare our nearby U/LIRGs with high- $z$  galaxies. In the previous sections, we investigated the uncertainty of the usage of Band 8 information, that is, [C I] (1–0), CO (4–3), and the dust continuum as a tracer of bulk  $M_{\text{H}_2}$  of the galaxies. However, the most important reason for using Band 8 measurements is that we can directly compare nearby and high- $z$  galaxies.

Using the high- $z$  [C I] (1–0) sample compiled by Valentino et al. (2018, 2020), we investigated the properties of high- $z$  and nearby galaxies in this section. We compared three groups: 29 nearby U/LIRGs from our survey, 22 galaxies on the main sequence at  $z \sim 1$  ( $z \sim 1$  MS), and 27 galaxies at  $z = 2 - 4$  who are categorized as SMGs ( $z = 2 - 4$  SMGs) from Valentino et al. (2018, 2020).

We compared the nearby U/LIRGs,  $z \sim 1$  MS, and  $z = 2 - 4$  SMGs on the plane of  $L_{[\text{CII}](1-0)}/L_{\text{TIR}}$  and  $L_{[\text{CII}](1-0)}/L_{\text{CO}(4-3)}$ . The physical parameters of the PDR can be constrained in this plane (Alaghband-Zadeh et al. 2013; Bothwell et al. 2017; Valentino et al. 2018, 2020). We used the Photodissociation Region Toolbox (PDRT<sup>8</sup>; Kaufman et al. 1999, 2006; Pound & Wolfire 2008). This enabled us to investigate the density of H nuclei ( $n_{\text{H}}$  in units of  $\text{cm}^{-3}$ ) and incident far-ultraviolet (FUV) radiation field ( $U_{\text{uv}}$ ), assuming the

<sup>8</sup> <http://dustem.astro.umd.edu/pdrt/>

plane-parallel PDR model. The  $U_{\text{uv}}$  corresponds to photons at  $6 \text{ eV} \leq h\nu < 13.6 \text{ eV}$  in the unit of the average interstellar radiation field in the vicinity of the Sun ( $G_0$ ). The model provides the line intensities for each combination of  $n_{\text{H}}$  and  $U_{\text{uv}}$  by self-consistently solving for radiation transfer, thermal balance, and chemical processes.

Figure 6 shows  $L_{[\text{C I}](1-0)}/L_{\text{TIR}}$  versus  $L_{[\text{C I}](1-0)}/L_{\text{CO}(4-3)}$  for nearby U/LIRGs,  $z \sim 1$  MS, and  $z = 2 - 4$  SMGs. For nearby U/LIRGs, we use  $L_{\text{TIR}}$  from SED fitting (AGN contribution is subtracted) and assume that the typical ACA recovered [C I] flux is  $\sim 59\%$  when we calculate  $L_{[\text{C I}](1-0)}/L_{\text{TIR}}$ . The tracks for constant  $n_{\text{H}}$  and  $U_{\text{uv}}$  are indicated by the green solid and magenta dashed lines, respectively. According to a plane-parallel PDR geometry, the smaller [C I] (1-0)/CO (4-3) ratio indicates the denser PDR because UV radiation cannot penetrate deeply into the molecular medium. For example, the small line ratio (e.g.,  $L_{[\text{C I}](1-0)}/L_{\text{CO}(4-3)} < 0.1$ ) means high density ( $> 10^5 \text{ cm}^{-3}$ ). The small  $L_{[\text{C I}](1-0)}/L_{\text{TIR}}$  is indicative of a high  $U_{\text{uv}}$ . We found that the [C I] (1-0) weak galaxies such as NGC 6052 and NGC 7679 (e.g.,  $L_{[\text{C I}](1-0)}/L_{\text{CO}(4-3)} < 0.1$ ) are rare, including the high- $z$  galaxies (see also Israel & Baas 2002; Israel et al. 2015).

We used a t-test to determine if there is a significant difference among nearby U/LIRGs,  $z \sim 1$  MS, and  $z = 2 - 4$  SMGs in terms of  $L_{[\text{C I}](1-0)}/L_{\text{CO}(4-3)}$ . Figure 7 demonstrates that the distribution of  $L_{[\text{C I}](1-0)}/L_{\text{CO}(4-3)}$  in nearby U/LIRGs is the same as SMGs but is significantly different from MS. For example, the median value of  $L_{[\text{C I}](1-0)}/L_{\text{CO}(4-3)}$  is 0.42, 0.47, and 0.66 for nearby U/LIRGs,  $z = 2 - 4$  SMG, and  $z \sim 1$  MS, respectively. This means that the typical density is approximately 1.5 times larger in U/LIRGs and SMGs than in MS galaxies. We note that this suggestion, as shown in Figure 7(a), does not strongly depend on the missing flux issue of our ACA survey.

## 5. SUMMARY

We present our recent ACA band 8 observations of [C I] (1-0), CO (4-3), and dust continuum emission in 36 nearby U/LIRGs. The main results are as follows.

- Correlations were confirmed among  $L_{[\text{C I}](1-0)}$ ,  $L_{\text{CO}(4-3)}$ , and  $L_{630\mu\text{m}}$ . However, there was variation in the ratios among the three observables. For example, the range of [C I] (1-0)/CO (4-3) luminosity ratio is (0.1-1.1), including the [C I] (1-0) non-detection case for a ratio of  $< 0.08$  (i.e., NGC 6052 and NGC 7679).
- The observed [C I] luminosities did not correlate with inferred  $T_{\text{dust}}$ , or AGN/merger morphology.

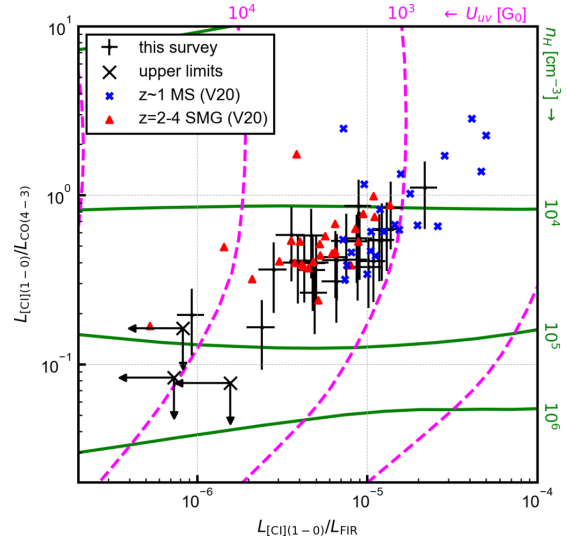


**Figure 6.**  $L_{[\text{C I}](1-0)}/L_{\text{CO}(4-3)}$  versus  $L_{[\text{C I}](1-0)}/L_{\text{TIR}}$  for our U/LIRGs (black),  $z=2-4$  SMGs (red), and  $z \sim 1$  MS (blue). The arrows indicate the [C I] (1-0) upper limits. The green solid and magenta dashed lines indicate the theoretical tracks (based on PDRT) for constant  $n_{\text{H}} [\text{cm}^{-3}]$  and  $U_{\text{uv}} [G_0]$ , respectively ( $G_0 = 1.6 \times 10^{-3} \text{ ergs cm}^{-2} \text{ s}^{-1}$ ; Habing 1968). We assume that the typical [C I] (1-0) recovered flux of 59%. The term “V20” indicates galaxies compiled by Valentino et al. (2020).

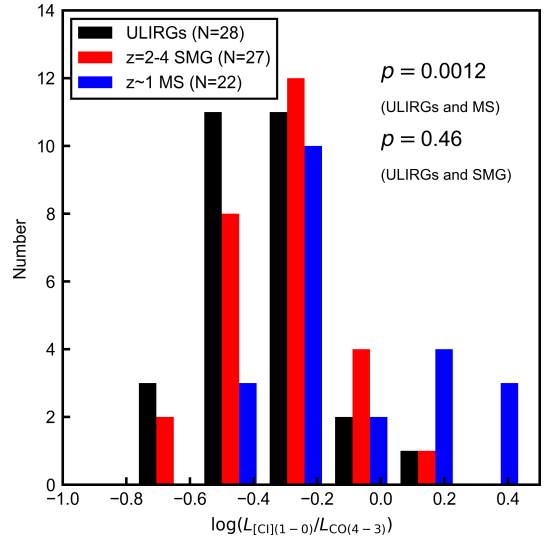


**Figure 7.** The distribution of  $L_{[\text{C I}](1-0)}/L_{\text{CO}(4-3)}$  for our nearby U/LIRGs (black),  $z=2-4$  SMGs (red), and  $z \sim 1$  MS (blue). The t-test p-values between U/LIRGs and MS and U/LIRGs and SMGs are shown. There is a significant difference between U/LIRGs and MS but the distributions of U/LIRGs and SMGs are the same. The  $N$  value means the number of galaxies used in this statistical test.

- As a case study for specific targets, we compare two AGN host galaxies; i.e., NGC 7679, which exhibits the smallest  $L_{[\text{C I}](1-0)}/L_{\text{CO}(4-3)} < 0.08$ , and NGC 5135, which exhibits the largest  $L_{[\text{C I}](1-0)}/L_{\text{CO}(4-3)} = 1.1 \pm 0.48$ . We found that the evidence of young starburst activity was more robust in NGC 7679 than in NGC 5135 and star formation activities in NGC 7679 may be related to the tidal interaction with the pair galaxy besides.
- We compare our nearby U/LIRGs and high- $z$  galaxies, such as  $z \sim 1$  galaxies on MS and  $z = 2 - 4$  SMGs. The mean value of the [C I] (1-0)/CO(4-3) ratio of U/LIRGs is similar to that of SMGs but smaller than that of galaxies on MS. This possibly indicates a higher hydrogen density in U/LIRGs and SMGs than MS when we assume a simple photodissociation model.

#### ACKNOWLEDGMENTS

This work was supported by the National Science Foundation of China (11721303, 11991052) and the National Key R&D Program of China (2016YFA0400702). This paper makes use of the following ALMA data: ADS/JAO.ALMA #2018.1 00994. ALMA is a partnership of ESO (representing its member states), NSF (USA) and NINS (Japan), together with NRC (Canada), MOST and ASIAA (Taiwan), and KASI (Republic of Korea), in cooperation with the Republic of Chile. The Joint ALMA Observatory is operated by ESO, AUI/NRAO and NAOJ. DI is supported by JSPS KAKENHI Grant Number JP18H03725. The authors appreciate Prof. Masami Ouchi (The University of Tokyo), Prof. Takuya Hashimoto (Tsukuba University), and Prof. Yoshiyuki Inoue (Osaka University) who provided a comfortable and fruitful research environment during the COVID-19 pandemic time.

#### REFERENCES

- |   |  |
|---|--|
| <p>Alaghband-Zadeh, S., Chapman, S. C., Swinbank, A. M., et al. 2013, MNRAS, 435, 1493, doi: <a href="https://doi.org/10.1093/mnras/stt1390">10.1093/mnras/stt1390</a></p> <p>Andreani, P., Retana-Montenegro, E., Zhang, Z.-Y., et al. 2018, A&amp;A, 615, A142, doi: <a href="https://doi.org/10.1051/0004-6361/201732560">10.1051/0004-6361/201732560</a></p> <p>Bisbas, T. G., Papadopoulos, P. P., &amp; Viti, S. 2015, ApJ, 803, 37, doi: <a href="https://doi.org/10.1088/0004-637X/803/1/37">10.1088/0004-637X/803/1/37</a></p> | <p>Bolatto, A. D., Wolfire, M., &amp; Leroy, A. K. 2013, ARA&amp;A, 51, 207, doi: <a href="https://doi.org/10.1146/annurev-astro-082812-140944">10.1146/annurev-astro-082812-140944</a></p> <p>Bothwell, M. S., Aguirre, J. E., Aravena, M., et al. 2017, MNRAS, 466, 2825, doi: <a href="https://doi.org/10.1093/mnras/stw3270">10.1093/mnras/stw3270</a></p> <p>Bourne, N., Dunlop, J. S., Simpson, J. M., et al. 2019, MNRAS, 482, 3135, doi: <a href="https://doi.org/10.1093/mnras/sty2773">10.1093/mnras/sty2773</a></p> <p>Burton, M. G., Ashley, M. C. B., Braiding, C., et al. 2015, ApJ, 811, 13, doi: <a href="https://doi.org/10.1088/0004-637X/811/1/13">10.1088/0004-637X/811/1/13</a></p> |
|---|--|

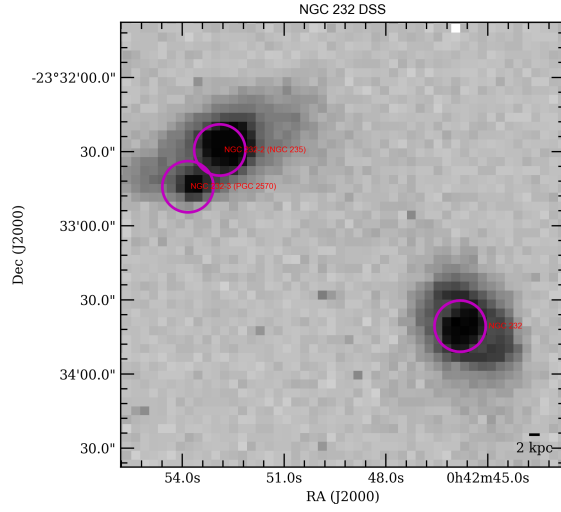
- Cañameras, R., Yang, C., Nesvadba, N. P. H., et al. 2018, *A&A*, 620, A61, doi: [10.1051/0004-6361/201833625](https://doi.org/10.1051/0004-6361/201833625)
- Carilli, C. L., & Walter, F. 2013, *ARA&A*, 51, 105, doi: [10.1146/annurev-astro-082812-140953](https://doi.org/10.1146/annurev-astro-082812-140953)
- Casey, C. M., Narayanan, D., & Cooray, A. 2014, *PhR*, 541, 45, doi: [10.1016/j.physrep.2014.02.009](https://doi.org/10.1016/j.physrep.2014.02.009)
- Cicone, C., Severgnini, P., Papadopoulos, P. P., et al. 2018, *ApJ*, 863, 143, doi: [10.3847/1538-4357/aad32a](https://doi.org/10.3847/1538-4357/aad32a)
- Clark, P. C., Glover, S. C. O., Ragan, S. E., & Duarte-Cabral, A. 2019, *MNRAS*, 486, 4622, doi: [10.1093/mnras/stz1119](https://doi.org/10.1093/mnras/stz1119)
- Cortzen, I., Magdis, G. E., Valentino, F., et al. 2020, *A&A*, 634, L14, doi: [10.1051/0004-6361/201937217](https://doi.org/10.1051/0004-6361/201937217)
- Crocker, A. F., Pellegrini, E., Smith, J. D. T., et al. 2019, *ApJ*, 887, 105, doi: [10.3847/1538-4357/ab4196](https://doi.org/10.3847/1538-4357/ab4196)
- Dannerbauer, H., Harrington, K., Díaz-Sánchez, A., et al. 2019, *AJ*, 158, 34, doi: [10.3847/1538-3881/aaf50b](https://doi.org/10.3847/1538-3881/aaf50b)
- Dunne, L., Maddox, S. J., Vlahakis, C., & Gomez, H. L. 2021, *MNRAS*, 501, 2573, doi: [10.1093/mnras/staa3526](https://doi.org/10.1093/mnras/staa3526)
- Eales, S., Smith, M. W. L., Auld, R., et al. 2012, *ApJ*, 761, 168, doi: [10.1088/0004-637X/761/2/168](https://doi.org/10.1088/0004-637X/761/2/168)
- Espada, D., Martin, S., Verley, S., et al. 2018, *ApJ*, 866, 77, doi: [10.3847/1538-4357/aae07e](https://doi.org/10.3847/1538-4357/aae07e)
- Fixsen, D. J., Bennett, C. L., & Mather, J. C. 1999, *ApJ*, 526, 207, doi: [10.1086/307962](https://doi.org/10.1086/307962)
- González-Alfonso, E., Fischer, J., Graciá-Carpio, J., et al. 2012, *A&A*, 541, A4, doi: [10.1051/0004-6361/201118029](https://doi.org/10.1051/0004-6361/201118029)
- Gu, Q. S., Huang, J. H., de Diego, J. A., et al. 2001, *A&A*, 374, 932, doi: [10.1051/0004-6361:20010806](https://doi.org/10.1051/0004-6361:20010806)
- Habing, H. J. 1968, *BAN*, 19, 421
- Hainline, L. J., Scoville, N. Z., Yun, M. S., et al. 2004, *ApJ*, 609, 61, doi: [10.1086/420920](https://doi.org/10.1086/420920)
- Harrington, K. C., Yun, M. S., Magnelli, B., et al. 2018, *MNRAS*, 474, 3866, doi: [10.1093/mnras/stx3043](https://doi.org/10.1093/mnras/stx3043)
- Ikedo, M., Oka, T., Tatematsu, K., Sekimoto, Y., & Yamamoto, S. 2002, *ApJS*, 139, 467, doi: [10.1086/338761](https://doi.org/10.1086/338761)
- Israel, F. P. 2020, *A&A*, 635, A131, doi: [10.1051/0004-6361/201834198](https://doi.org/10.1051/0004-6361/201834198)
- Israel, F. P., & Baas, F. 2001, *A&A*, 371, 433, doi: [10.1051/0004-6361:20010354](https://doi.org/10.1051/0004-6361:20010354)
- . 2002, *A&A*, 383, 82, doi: [10.1051/0004-6361:20011736](https://doi.org/10.1051/0004-6361:20011736)
- . 2003, *A&A*, 404, 495, doi: [10.1051/0004-6361:20030479](https://doi.org/10.1051/0004-6361:20030479)
- Israel, F. P., Rosenberg, M. J. F., & van der Werf, P. 2015, *A&A*, 578, A95, doi: [10.1051/0004-6361/201425175](https://doi.org/10.1051/0004-6361/201425175)
- Izumi, N., Fukui, Y., Tachihara, K., et al. 2020a, arXiv e-prints, arXiv:2012.01330. <https://arxiv.org/abs/2012.01330>
- Izumi, T., Wada, K., Fukushige, R., Hamamura, S., & Kohno, K. 2018, *ApJ*, 867, 48, doi: [10.3847/1538-4357/aad20b](https://doi.org/10.3847/1538-4357/aad20b)
- Izumi, T., Nguyen, D. D., Imanishi, M., et al. 2020b, arXiv e-prints, arXiv:2006.09406. <https://arxiv.org/abs/2006.09406>
- Jiao, Q., Zhao, Y., Zhu, M., et al. 2017, *The Astrophysical Journal*, 840, L18, doi: [10.3847/2041-8213/aa6f0f](https://doi.org/10.3847/2041-8213/aa6f0f)
- Jiao, Q., Zhao, Y., Lu, N., et al. 2019, *ApJ*, 880, 133, doi: [10.3847/1538-4357/ab29ed](https://doi.org/10.3847/1538-4357/ab29ed)
- Jin, S., Daddi, E., Magdis, G. E., et al. 2019, *ApJ*, 887, 144, doi: [10.3847/1538-4357/ab55d6](https://doi.org/10.3847/1538-4357/ab55d6)
- Kamenetzky, J., Rangwala, N., Glenn, J., Maloney, P. R., & Conley, A. 2016, *The Astrophysical Journal*, 829, 93, doi: [10.3847/0004-637x/829/2/93](https://doi.org/10.3847/0004-637x/829/2/93)
- Kaufman, M. J., Wolfire, M. G., & Hollenbach, D. J. 2006, *ApJ*, 644, 283, doi: [10.1086/503596](https://doi.org/10.1086/503596)
- Kaufman, M. J., Wolfire, M. G., Hollenbach, D. J., & Luhman, M. L. 1999, *ApJ*, 527, 795, doi: [10.1086/308102](https://doi.org/10.1086/308102)
- Kelly, B. C. 2007, *ApJ*, 665, 1489, doi: [10.1086/519947](https://doi.org/10.1086/519947)
- Koda, J., Sawada, T., Sakamoto, K., et al. 2020, *ApJL*, 890, L10, doi: [10.3847/2041-8213/ab70b7](https://doi.org/10.3847/2041-8213/ab70b7)
- Kramer, C., Cubick, M., Röllig, M., et al. 2008, *A&A*, 477, 547, doi: [10.1051/0004-6361:20077815](https://doi.org/10.1051/0004-6361:20077815)
- Krips, M., Martín, S., Sakamoto, K., et al. 2016, *A&A*, 592, L3, doi: [10.1051/0004-6361/201628882](https://doi.org/10.1051/0004-6361/201628882)
- Larson, K. L., Sanders, D. B., Barnes, J. E., et al. 2016, *ApJ*, 825, 128, doi: [10.3847/0004-637X/825/2/128](https://doi.org/10.3847/0004-637X/825/2/128)
- Lee, M. M., Tanaka, I., Iono, D., et al. 2021, arXiv e-prints, arXiv:2101.04691. <https://arxiv.org/abs/2101.04691>
- Lu, N., Zhao, Y., Díaz-Santos, T., et al. 2017 (IOP Publishing), 1, doi: [10.3847/1538-4365/aa6476](https://doi.org/10.3847/1538-4365/aa6476)
- Magdis, G. E., Daddi, E., Béthermin, M., et al. 2012, *ApJ*, 760, 6, doi: [10.1088/0004-637X/760/1/6](https://doi.org/10.1088/0004-637X/760/1/6)
- McMullin, J. P., Waters, B., Schiebel, D., Young, W., & Golap, K. 2007, *Astronomical Society of the Pacific Conference Series*, Vol. 376, CASA Architecture and Applications, ed. R. A. Shaw, F. Hill, & D. J. Bell, 127
- Meijerink, R., & Spaans, M. 2005, *A&A*, 436, 397, doi: [10.1051/0004-6361:20042398](https://doi.org/10.1051/0004-6361:20042398)
- Meijerink, R., Spaans, M., & Israel, F. P. 2007, *A&A*, 461, 793, doi: [10.1051/0004-6361:20066130](https://doi.org/10.1051/0004-6361:20066130)
- Michiyama, T., Ueda, J., Tadaki, K.-i., et al. 2020, arXiv e-prints, arXiv:2006.10059. <https://arxiv.org/abs/2006.10059>
- Miyamoto, Y., Seta, M., Nakai, N., et al. 2018, *PASJ*, 70, L1, doi: [10.1093/pasj/psy016](https://doi.org/10.1093/pasj/psy016)
- Ojha, R., Stark, A. A., Hsieh, H. H., et al. 2001, *ApJ*, 548, 253, doi: [10.1086/318693](https://doi.org/10.1086/318693)
- Oka, T., Yamamoto, S., Iwata, M., et al. 2001, *ApJ*, 558, 176, doi: [10.1086/321536](https://doi.org/10.1086/321536)
- Papadopoulos, P. P., Bisbas, T. G., & Zhang, Z.-Y. 2018, *MNRAS*, 478, 1716, doi: [10.1093/mnras/sty1077](https://doi.org/10.1093/mnras/sty1077)



- Papadopoulos, P. P., & Greve, T. R. 2004, *ApJL*, 615, L29, doi: [10.1086/426059](https://doi.org/10.1086/426059)
- Papadopoulos, P. P., Thi, W. F., & Viti, S. 2004, *MNRAS*, 351, 147, doi: [10.1111/j.1365-2966.2004.07762.x](https://doi.org/10.1111/j.1365-2966.2004.07762.x)
- Planck Collaboration, Ade, P. A. R., Aghanim, N., et al. 2016, *A&A*, 594, A13, doi: [10.1051/0004-6361/201525830](https://doi.org/10.1051/0004-6361/201525830)
- Popping, G., Decarli, R., Man, A. W. S., et al. 2017, *A&A*, 602, A11, doi: [10.1051/0004-6361/201730391](https://doi.org/10.1051/0004-6361/201730391)
- Pound, M. W., & Wolfire, M. G. 2008, *Astronomical Society of the Pacific Conference Series*, Vol. 394, *The Photo Dissociation Region Toolbox*, ed. R. W. Argyle, P. S. Bunclark, & J. R. Lewis, 654
- Rose, M., Tadhunter, C., Ramos Almeida, C., et al. 2018, *MNRAS*, 474, 128, doi: [10.1093/mnras/stx2590](https://doi.org/10.1093/mnras/stx2590)
- Saito, T., Michiyama, T., Liu, D., et al. 2020, *MNRAS*, 497, 3591, doi: [10.1093/mnras/staa2086](https://doi.org/10.1093/mnras/staa2086)
- Salak, D., Nakai, N., Seta, M., & Miyamoto, Y. 2019, *ApJ*, 887, 143, doi: [10.3847/1538-4357/ab55dc](https://doi.org/10.3847/1538-4357/ab55dc)
- Sanders, D. B., Mazzarella, J. M., Kim, D. C., Surace, J. A., & Soifer, B. T. 2003, *AJ*, 126, 1607, doi: [10.1086/376841](https://doi.org/10.1086/376841)
- Scoville, N., Aussel, H., Sheth, K., et al. 2014, *ApJ*, 783, 84, doi: [10.1088/0004-637X/783/2/84](https://doi.org/10.1088/0004-637X/783/2/84)
- Scoville, N., Sheth, K., Aussel, H., et al. 2016, *ApJ*, 820, 83, doi: [10.3847/0004-637X/820/2/83](https://doi.org/10.3847/0004-637X/820/2/83)
- Shangguan, J., Ho, L. C., Li, R., et al. 2019, *ApJ*, 870, 104, doi: [10.3847/1538-4357/aaf21a](https://doi.org/10.3847/1538-4357/aaf21a)
- Solomon, P. M., & Vanden Bout, P. A. 2005, *ARA&A*, 43, 677, doi: [10.1146/annurev.astro.43.051804.102221](https://doi.org/10.1146/annurev.astro.43.051804.102221)
- Tadaki, K., Iono, D., Yun, M. S., et al. 2018, *Nature*, 560, 613, doi: [10.1038/s41586-018-0443-1](https://doi.org/10.1038/s41586-018-0443-1)
- Talia, M., Pozzi, F., Vallini, L., et al. 2018, *MNRAS*, 476, 3956, doi: [10.1093/mnras/sty481](https://doi.org/10.1093/mnras/sty481)
- Valentino, F., Magdis, G. E., Daddi, E., et al. 2018, *ApJ*, 869, 27, doi: [10.3847/1538-4357/aaeb88](https://doi.org/10.3847/1538-4357/aaeb88)
- . 2020, *ApJ*, 890, 24, doi: [10.3847/1538-4357/ab6603](https://doi.org/10.3847/1538-4357/ab6603)
- Veilleux, S., Meléndez, M., Sturm, E., et al. 2013, *ApJ*, 776, 27, doi: [10.1088/0004-637X/776/1/27](https://doi.org/10.1088/0004-637X/776/1/27)
- Walter, F., Weiß, A., Downes, D., Decarli, R., & Henkel, C. 2011, *ApJ*, 730, 18, doi: [10.1088/0004-637X/730/1/18](https://doi.org/10.1088/0004-637X/730/1/18)
- Weiß, A., Walter, F., & Scoville, N. Z. 2005, *A&A*, 438, 533, doi: [10.1051/0004-6361:20052667](https://doi.org/10.1051/0004-6361:20052667)
- Yang, C., Omont, A., Beelen, A., et al. 2017, *A&A*, 608, A144, doi: [10.1051/0004-6361/201731391](https://doi.org/10.1051/0004-6361/201731391)

## APPENDIX

## A. APPENDIX

A.1. *Figures*

**Figure A1.1.** The optical image obtained by Digitized Sky Survey (DSS), the fits images are obtained by astroquery.skyview modules in Python. The magenta circle indicates the [C I](1–0) FoV.

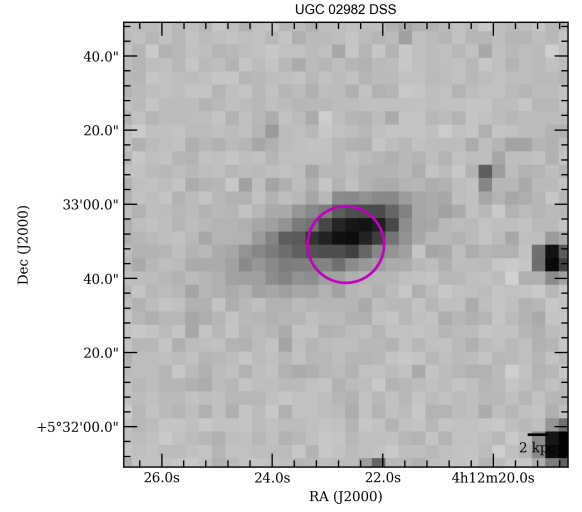


**Figure A1.3.** Same as Figure A1.1.

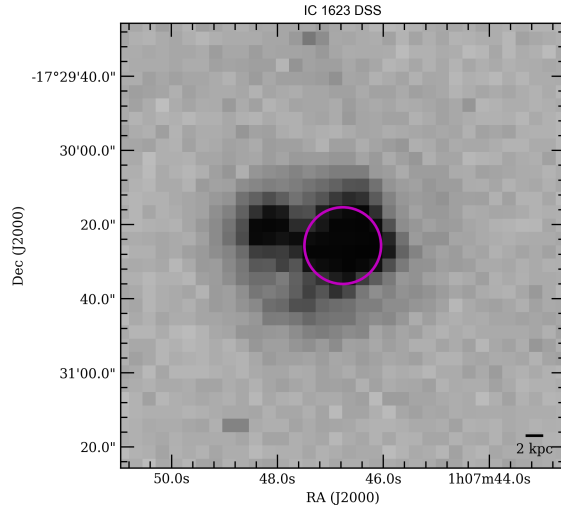


**Figure A1.2.** Same as Figure A1.1.

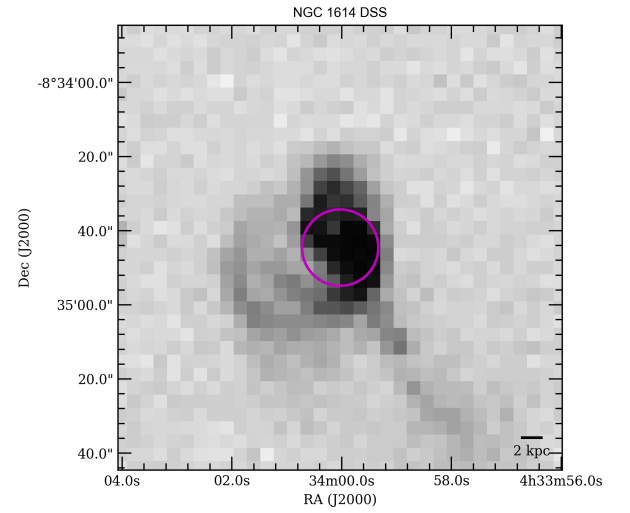


**Figure A1.4.** Same as Figure A1.1.

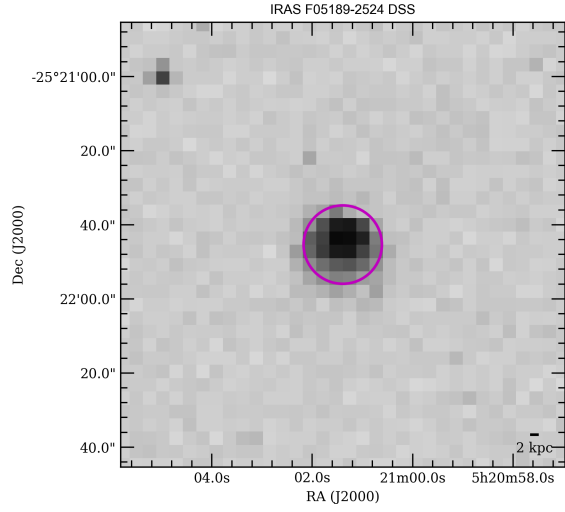


**Figure A1.5.** Same as Figure A1.1.

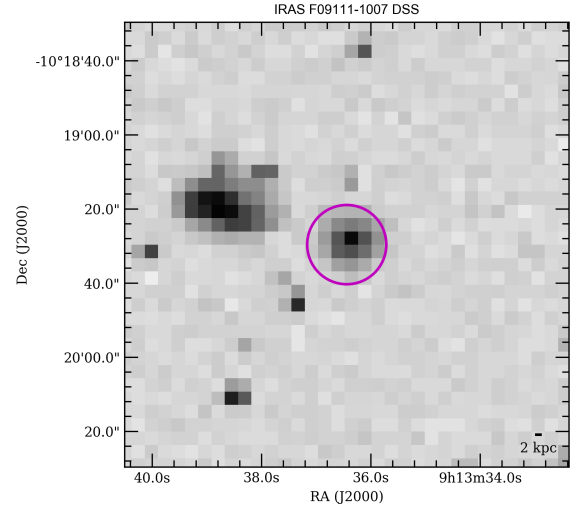


**Figure A1.7.** Same as Figure A1.1.

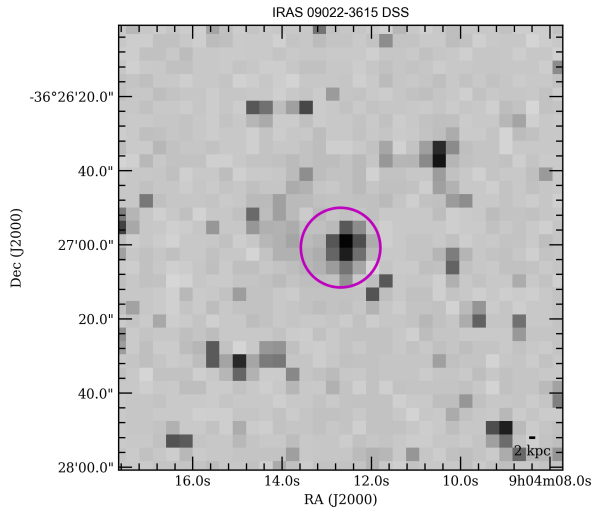


**Figure A1.6.** Same as Figure A1.1.

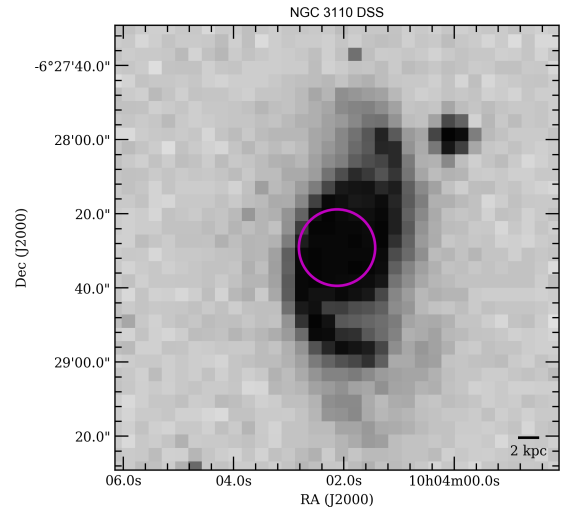


**Figure A1.8.** Same as Figure A1.1.



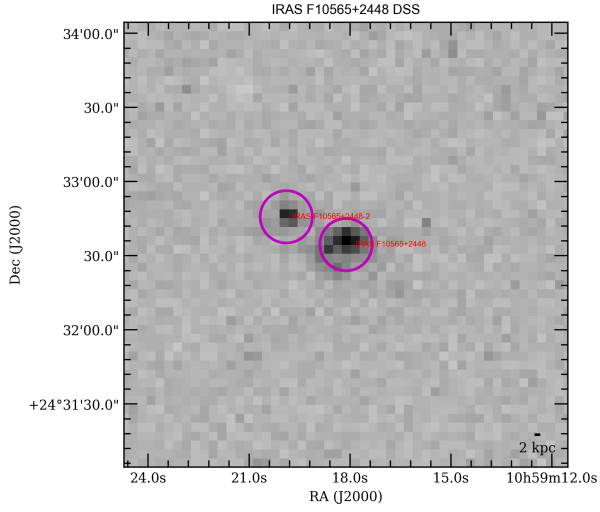


Figure A1.9. Same as Figure A1.1.

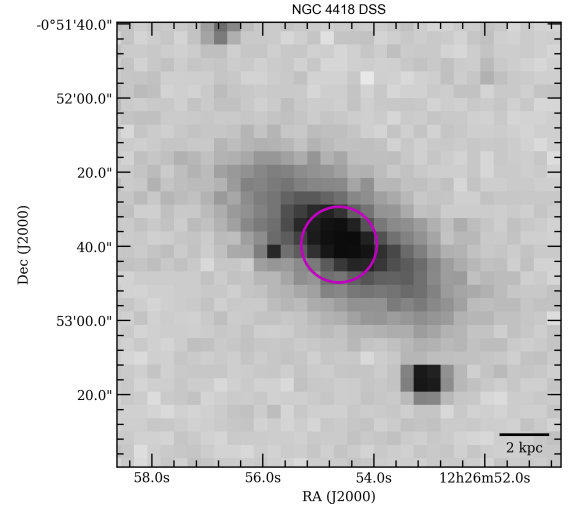


Figure A1.11. Same as Figure A1.1.

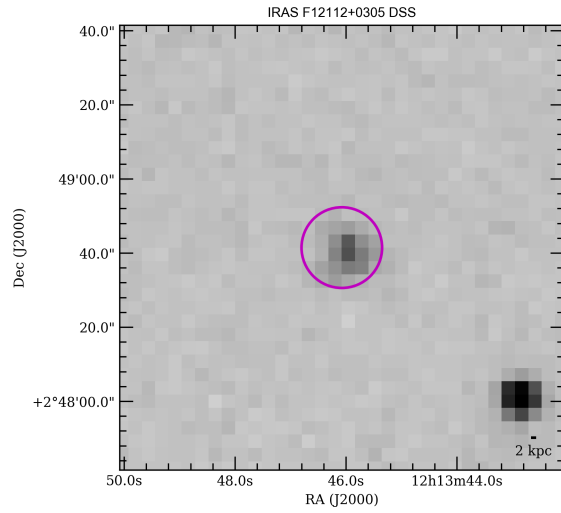


Figure A1.10. Same as Figure A1.1.

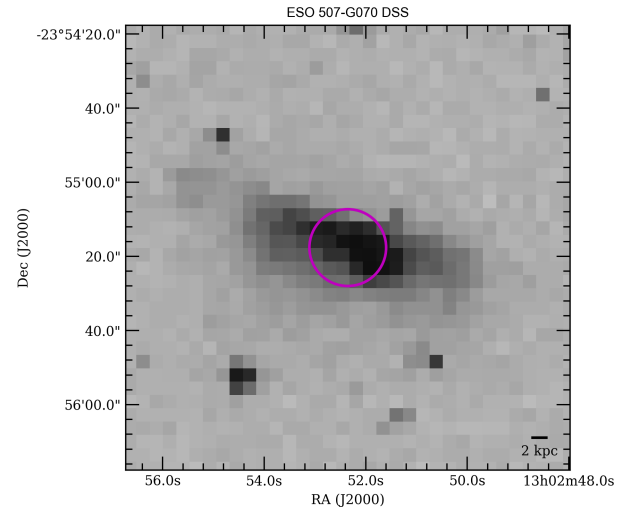
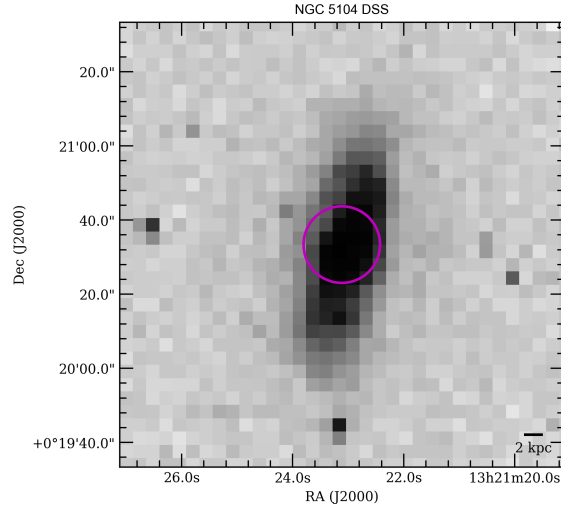
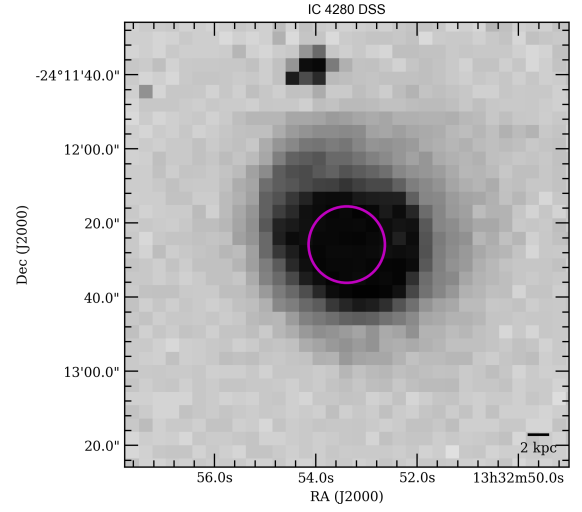


Figure A1.12. Same as Figure A1.1.



**Figure A1.13.** Same as Figure A1.1.



**Figure A1.15.** Same as Figure A1.1.

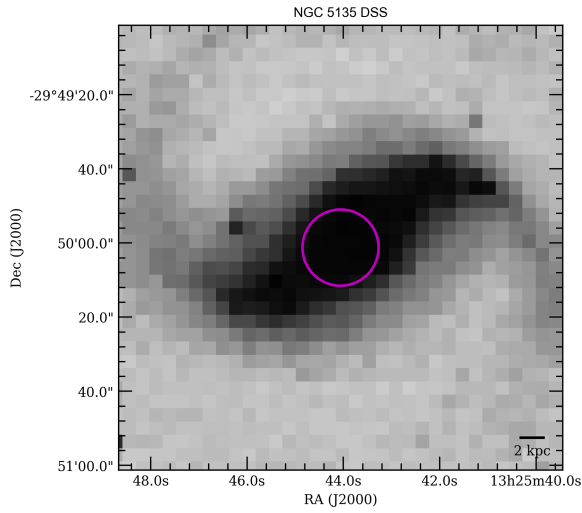


**Figure A1.14.** Same as Figure A1.1.



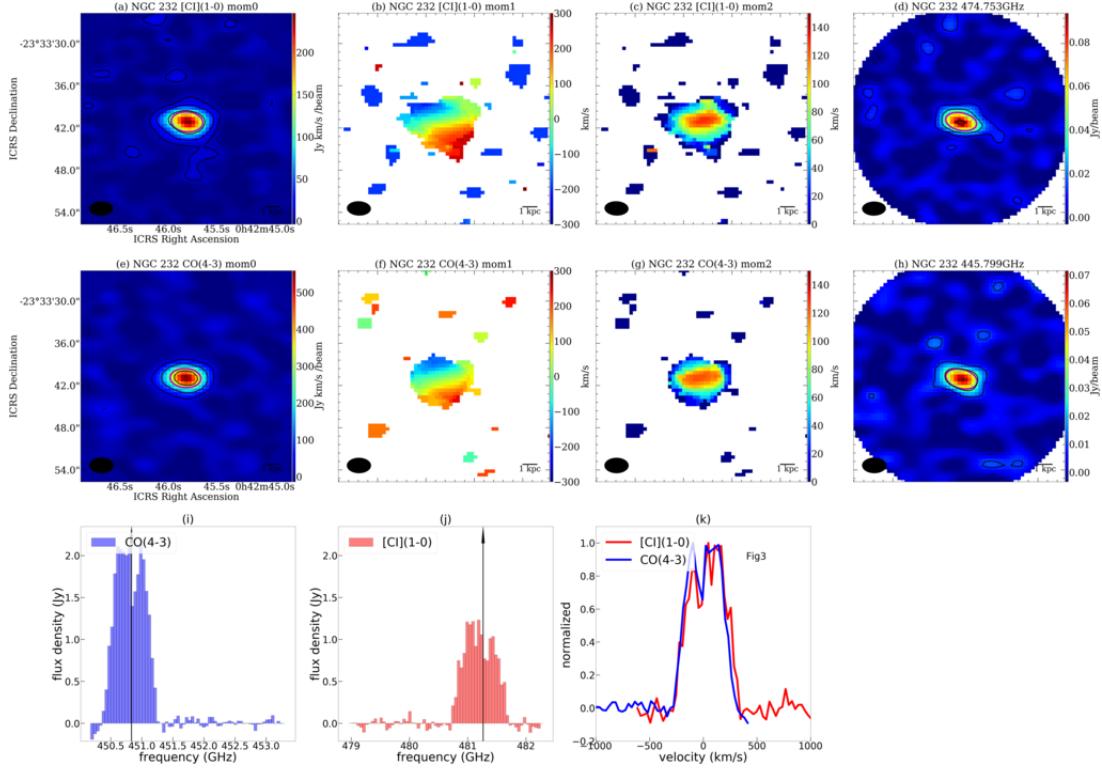


**Figure A2.1.** (a) The velocity integrated intensity map (mom0) of [C I] (1–0) emission line. The  $n$ th contours are at  $3n\sigma$  where  $\sigma$  is the rms level of the map shown in Table A.4. The magenta circle indicates the ACA FoV calculated by equation 1. (b) The velocity field map (mom1) of [C I] (1–0) emission line. (c) The velocity dispersion map (mom2) of [C I] (1–0) emission line. The mom1 and mom2 maps are made by clipping  $3\sigma$  emission in data cube. (d) The continuum emission map associated with [C I] (1–0) observation. The  $n$ th contours are at  $3n\sigma$  where  $\sigma$  is the rms level of the map shown in Table A.4. (e)–(h) The same map with (a)–(d) but for CO (4–3) emission. (i) and (j) The CO (4–3) and [C I] (1–0) spectrum with the aperture of FoV. The spectrum were derived from `specflux` task in `CASA`. (k) The normalized CO (4–3) and [C I] (1–0) spectrum. The velocity is calculated as the offset from the systematic velocity shown in Table A.1. In the case of CO (4–3) detection and [C I] (1–0) non-detection, [C I] (1–0) moment maps are made by assuming same velocity range for integration. If both CO (4–3) and [C I] (1–0) are non-detection, we integrated  $\pm 200 \text{ km s}^{-1}$  from systematic velocities.



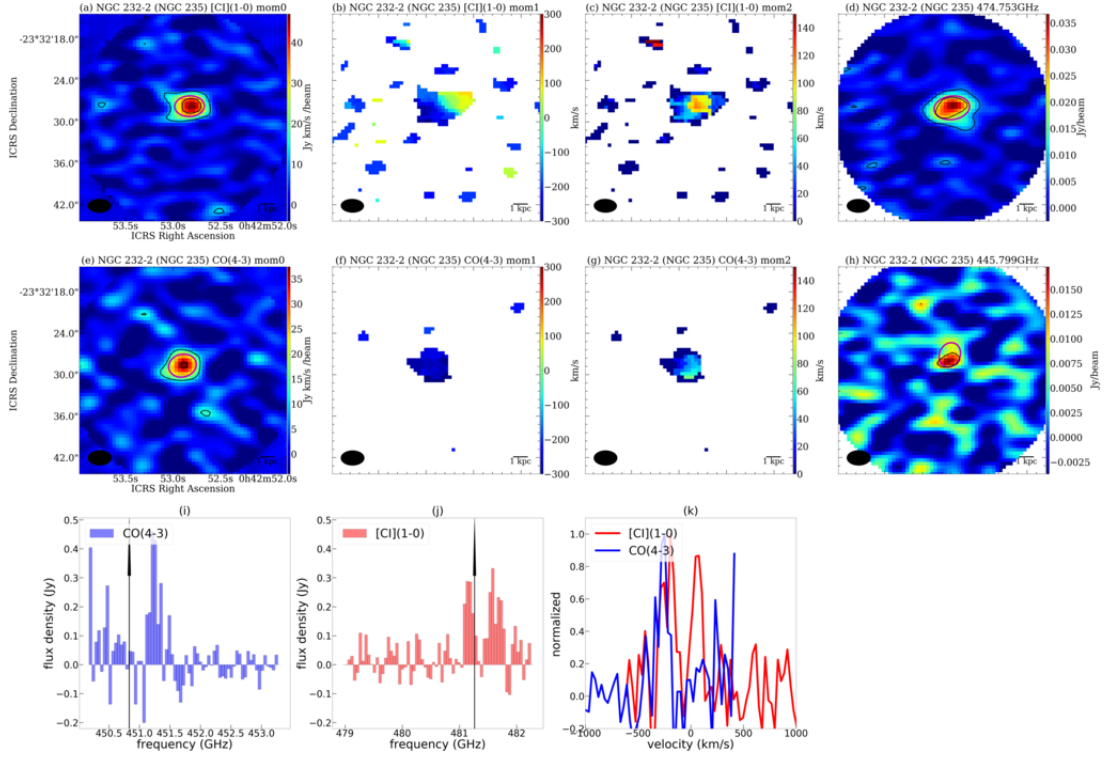


Figure A2.2. Same as Figure A2.1.

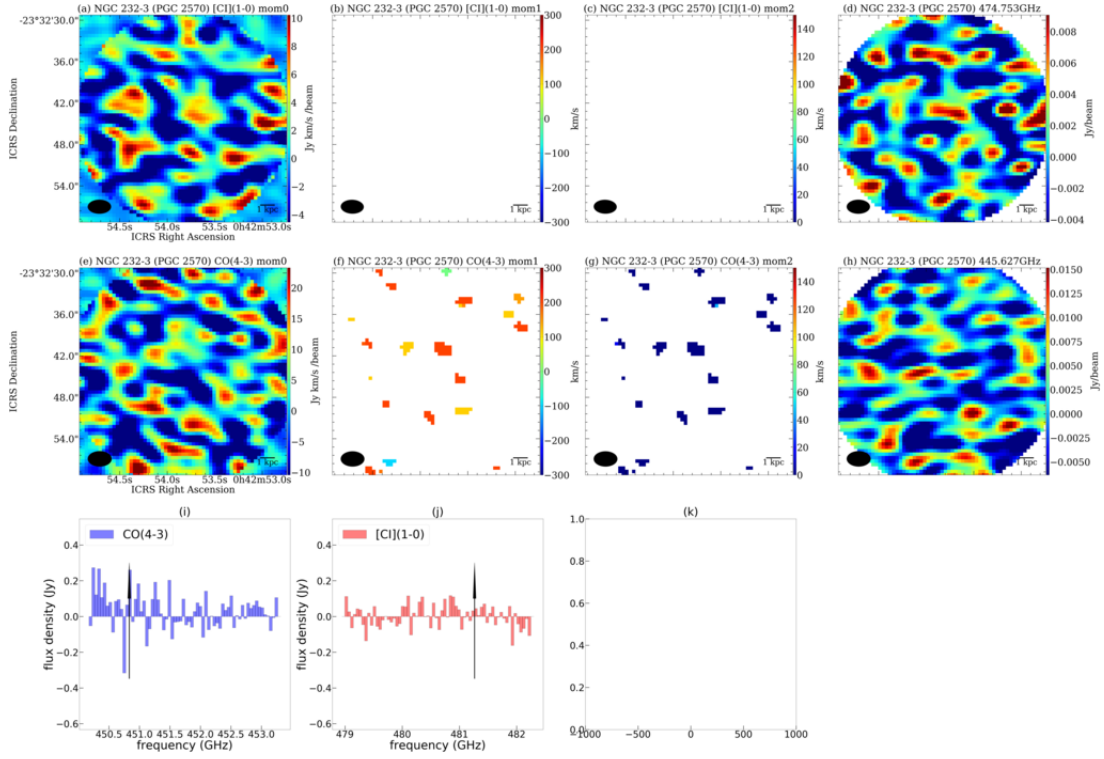


Figure A2.3. Same as Figure A2.1.

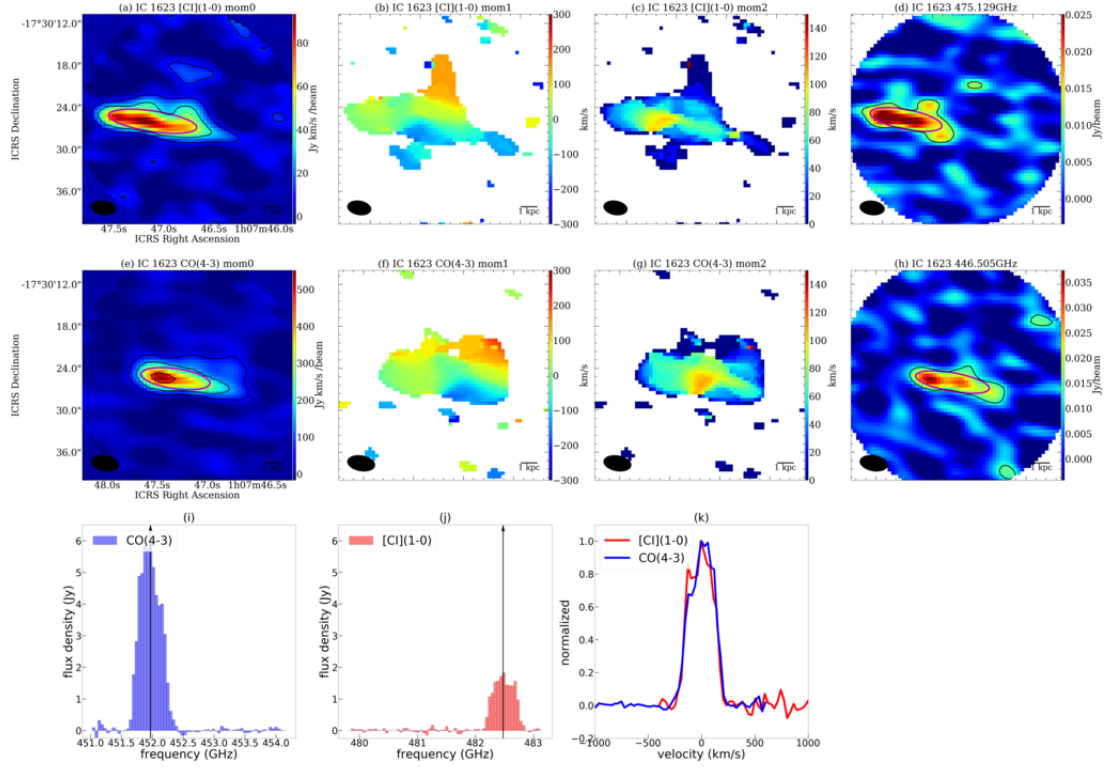


Figure A2.4. Same as Figure A2.1.

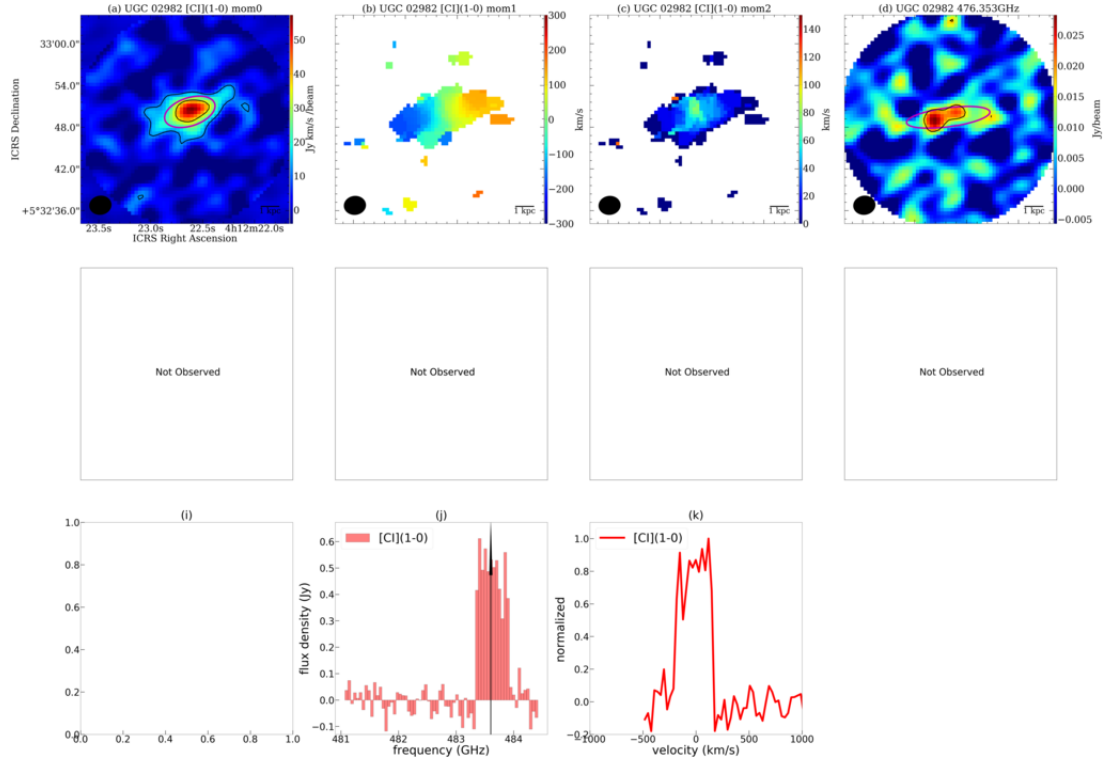


Figure A2.5. Same as Figure A2.1.

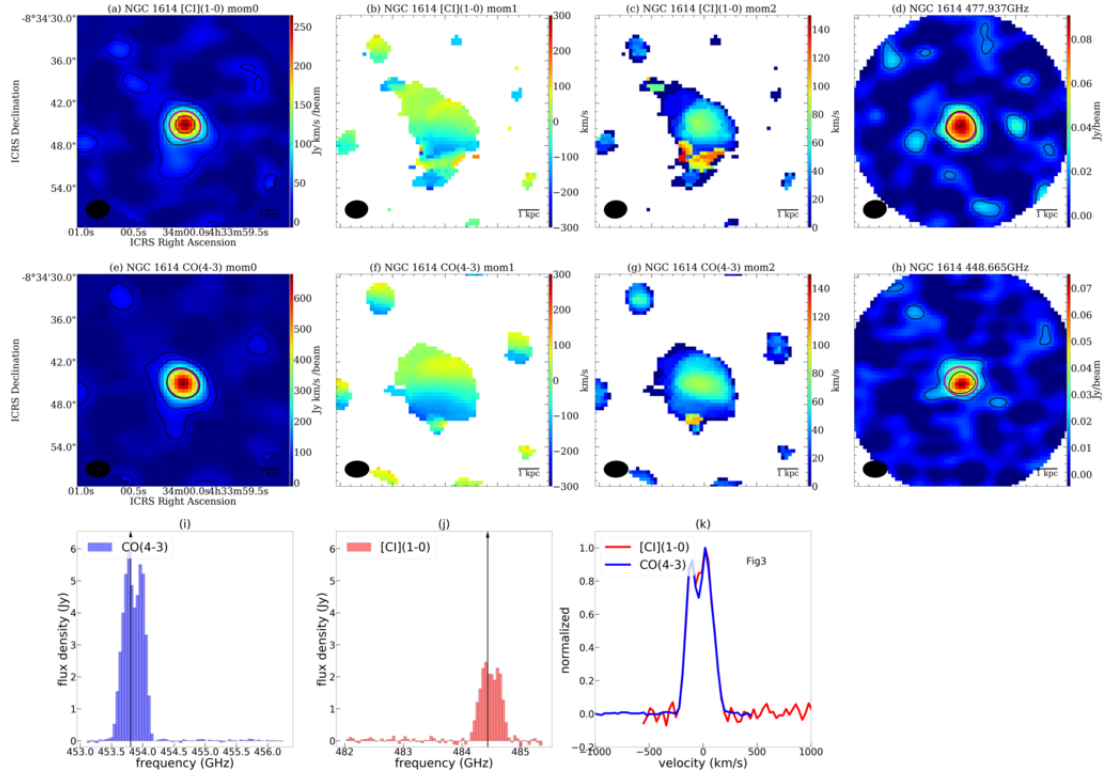


Figure A2.6. Same as Figure A2.1.

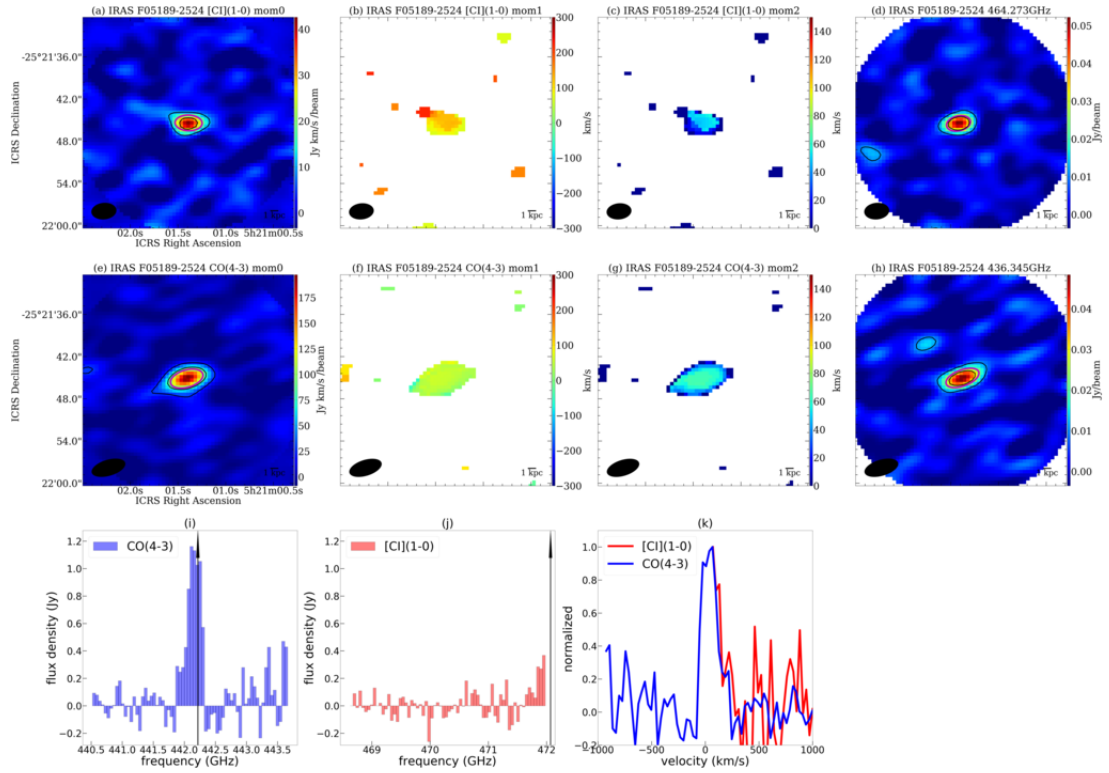


Figure A2.7. Same as Figure A2.1.

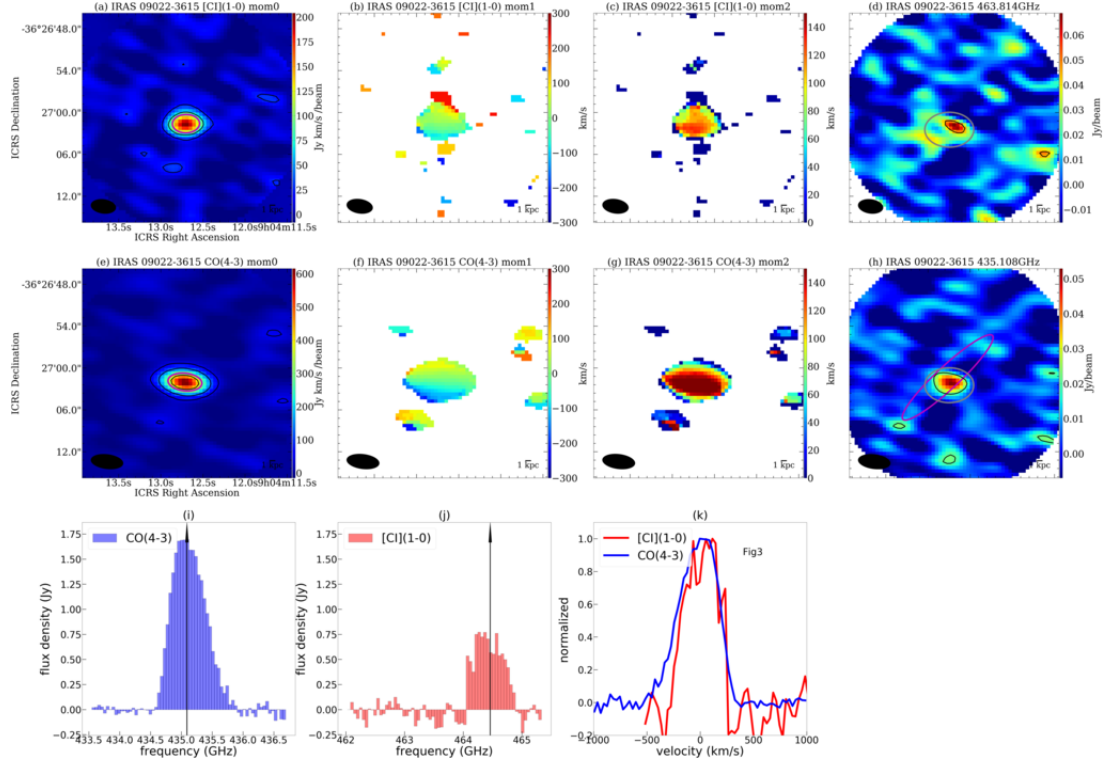


Figure A2.8. Same as Figure A2.1.

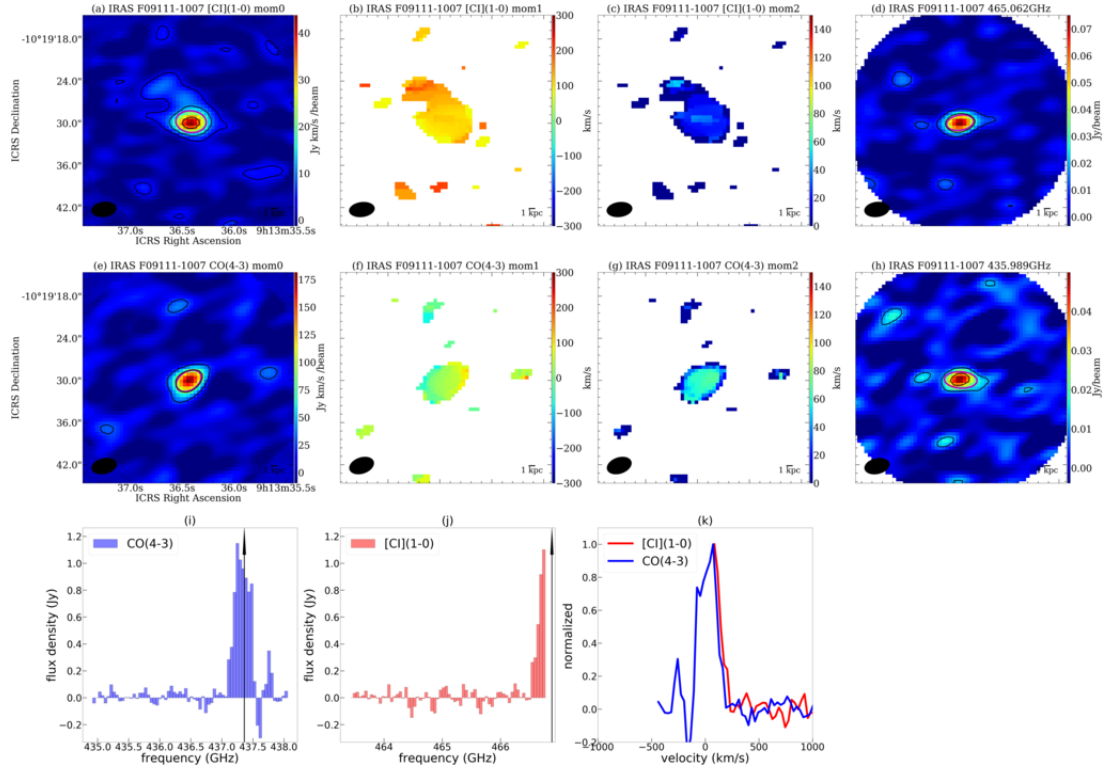


Figure A2.9. Same as Figure A2.1.

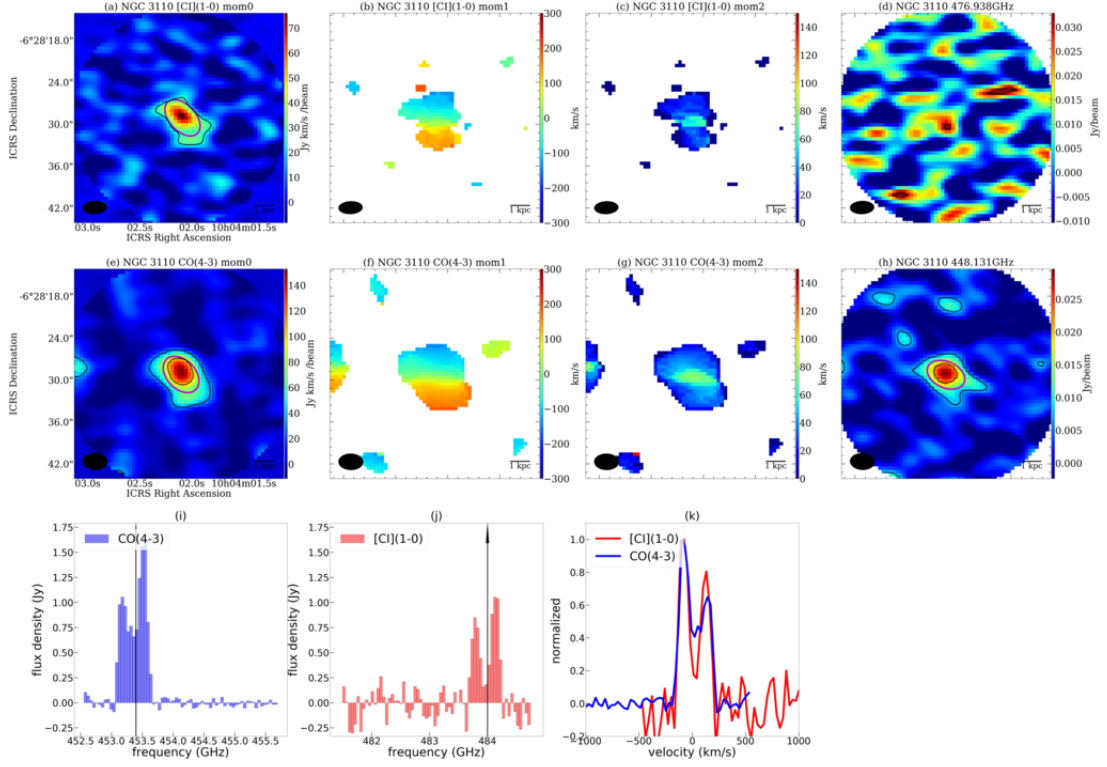


Figure A2.10. Same as Figure A2.1.

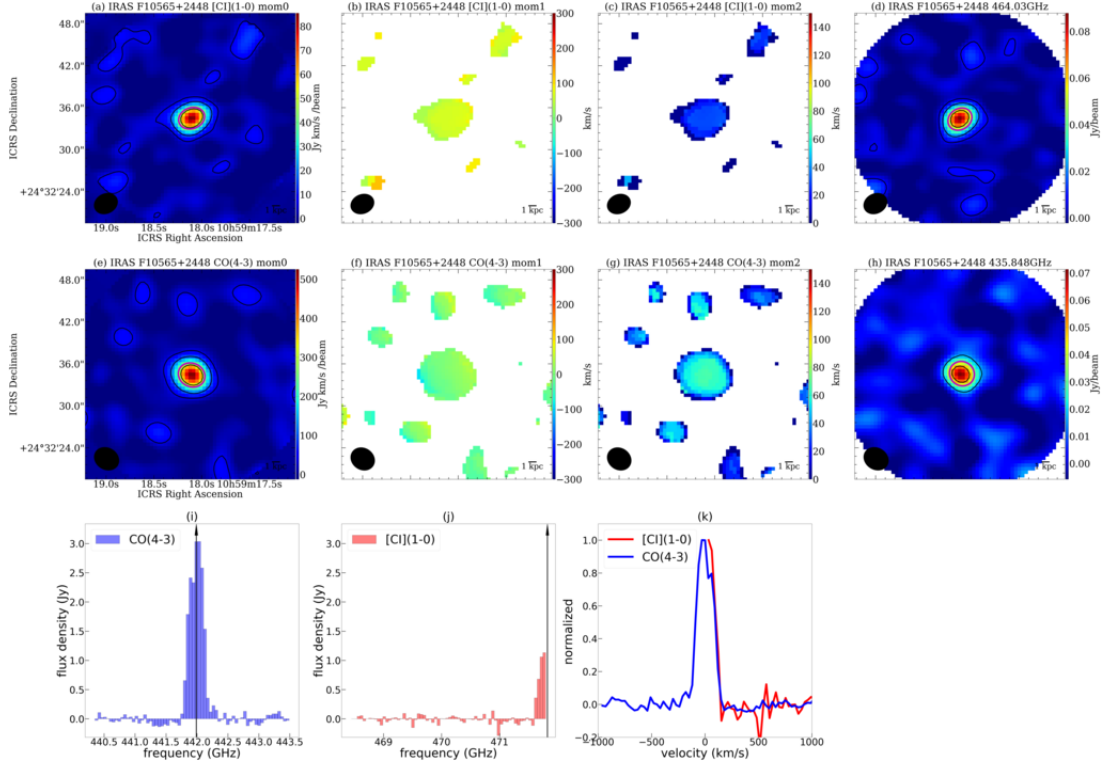


Figure A2.11. Same as Figure A2.1.



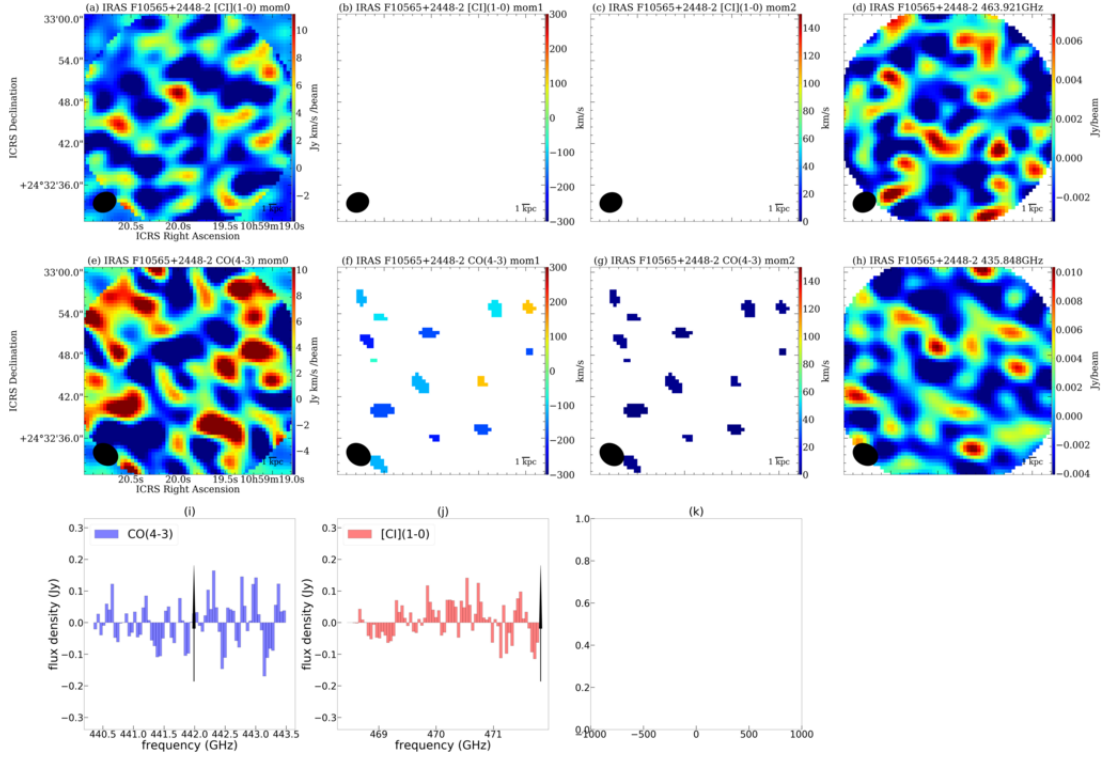


Figure A2.12. Same as Figure A2.1.

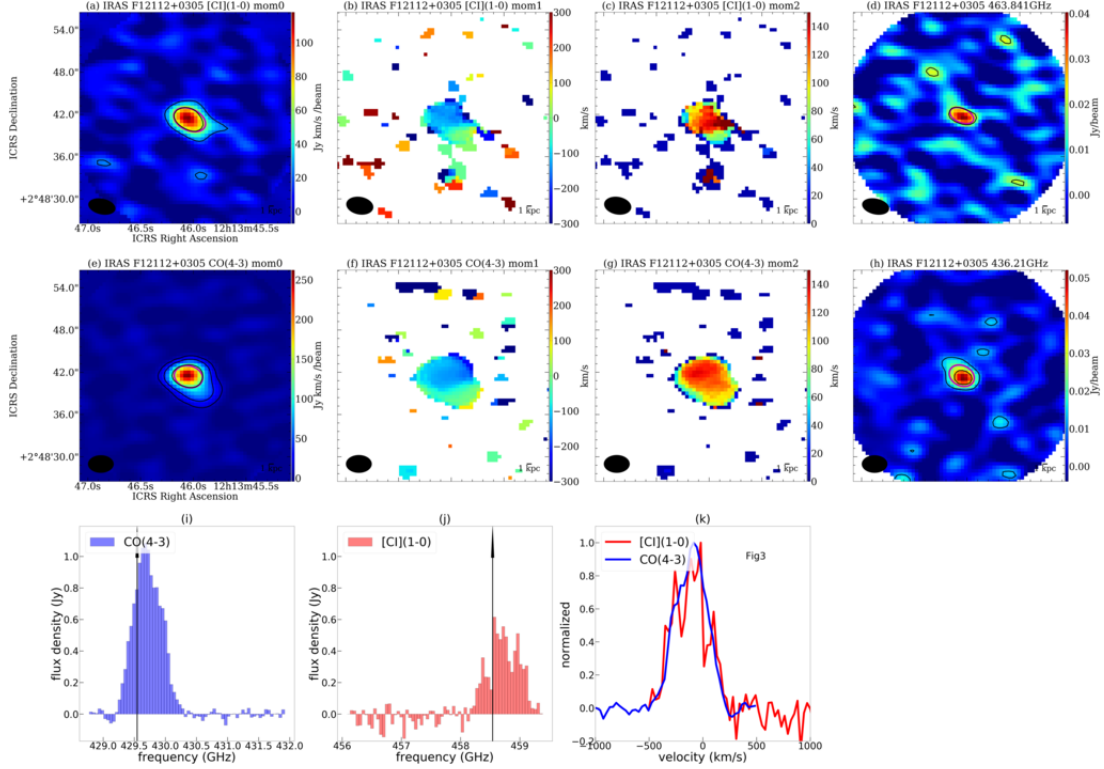


Figure A2.13. Same as Figure A2.1.

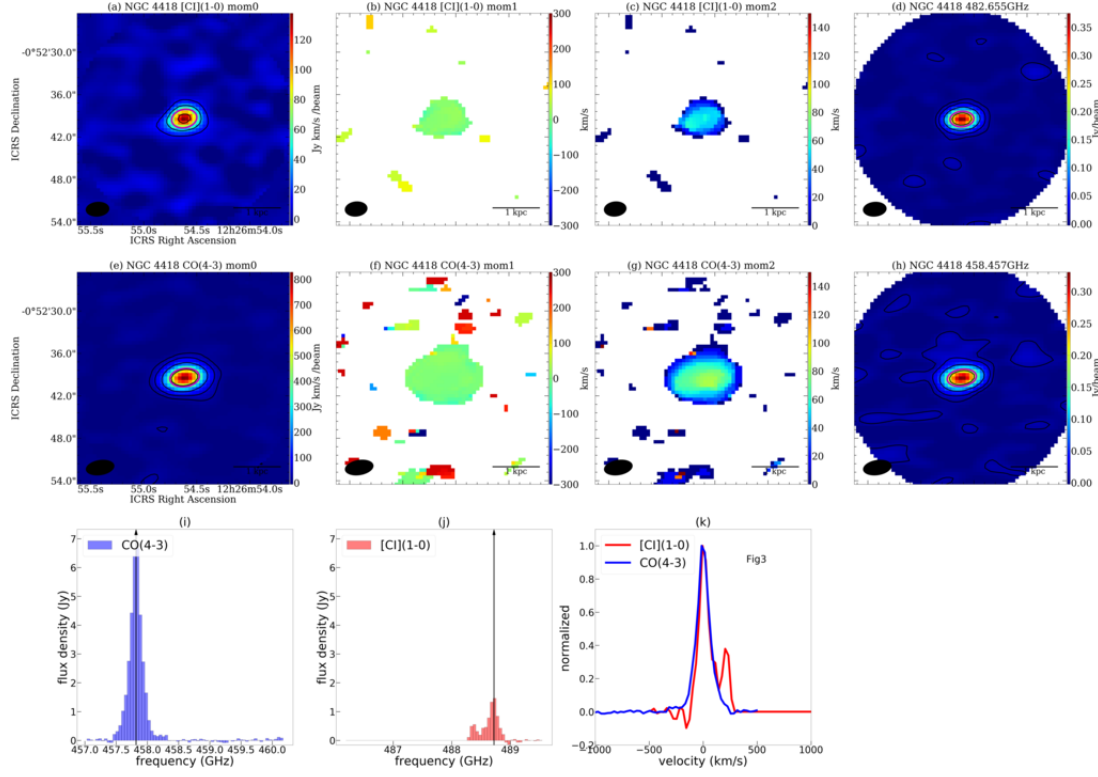


Figure A2.14. Same as Figure A2.1.

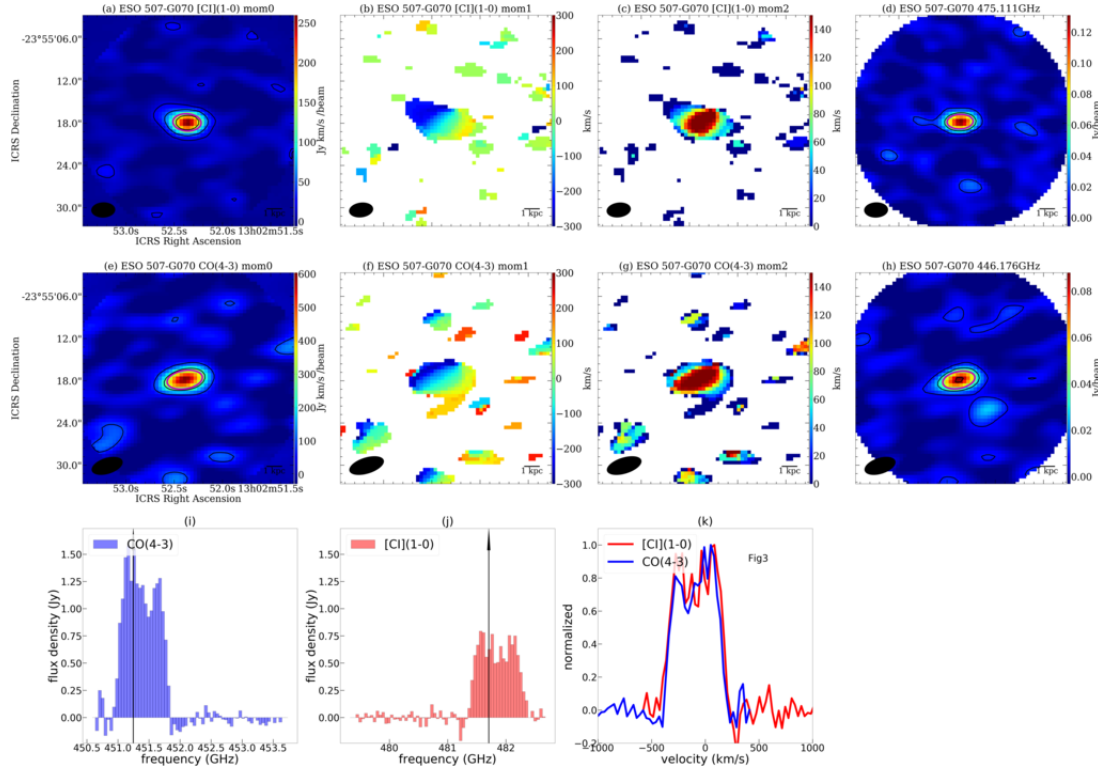


Figure A2.15. Same as Figure A2.1.



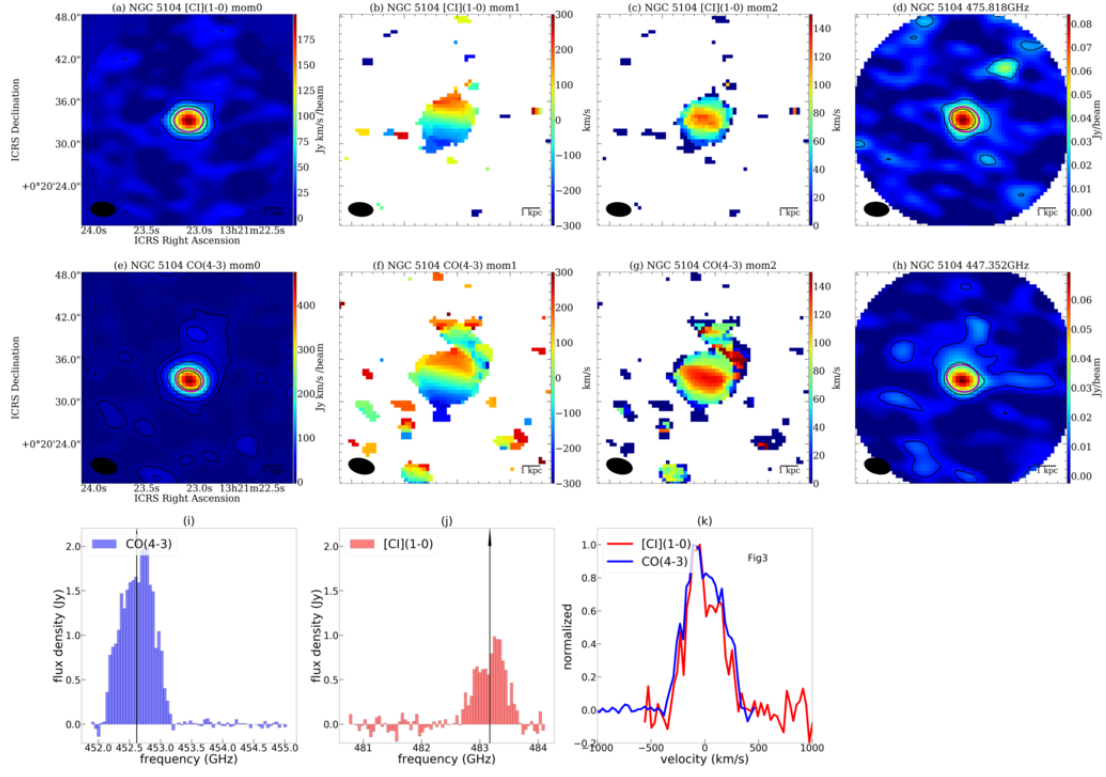


Figure A2.16. Same as Figure A2.1.

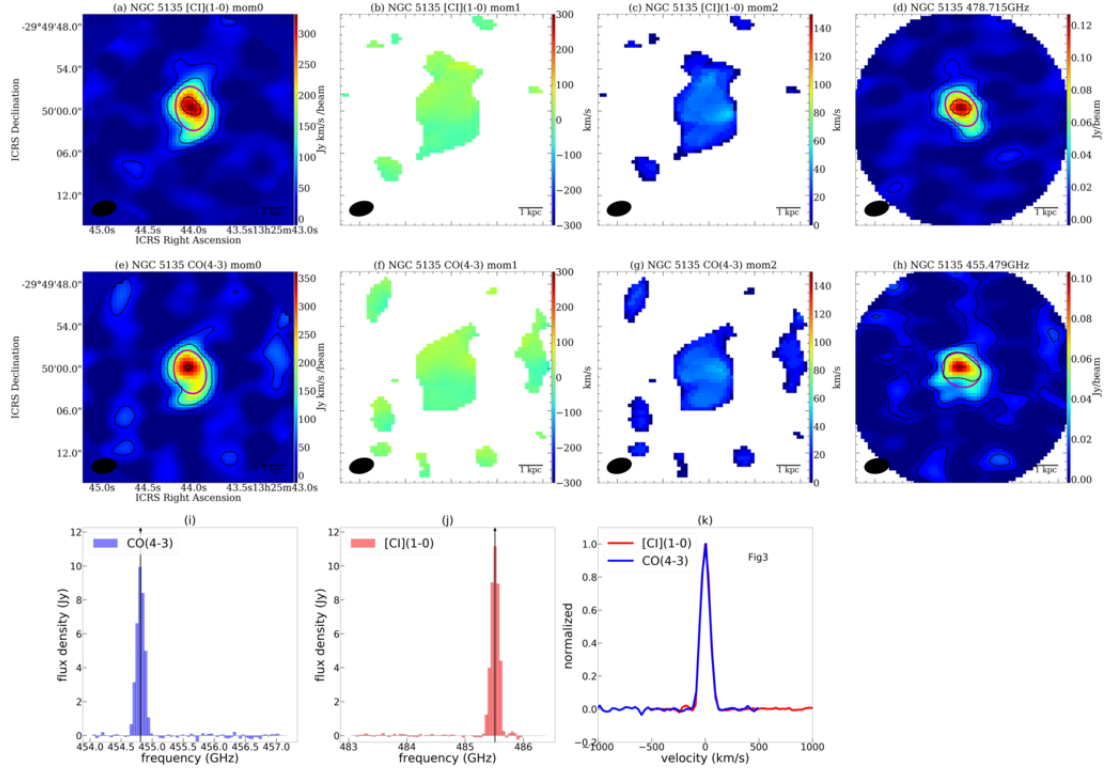


Figure A2.17. Same as Figure A2.1.

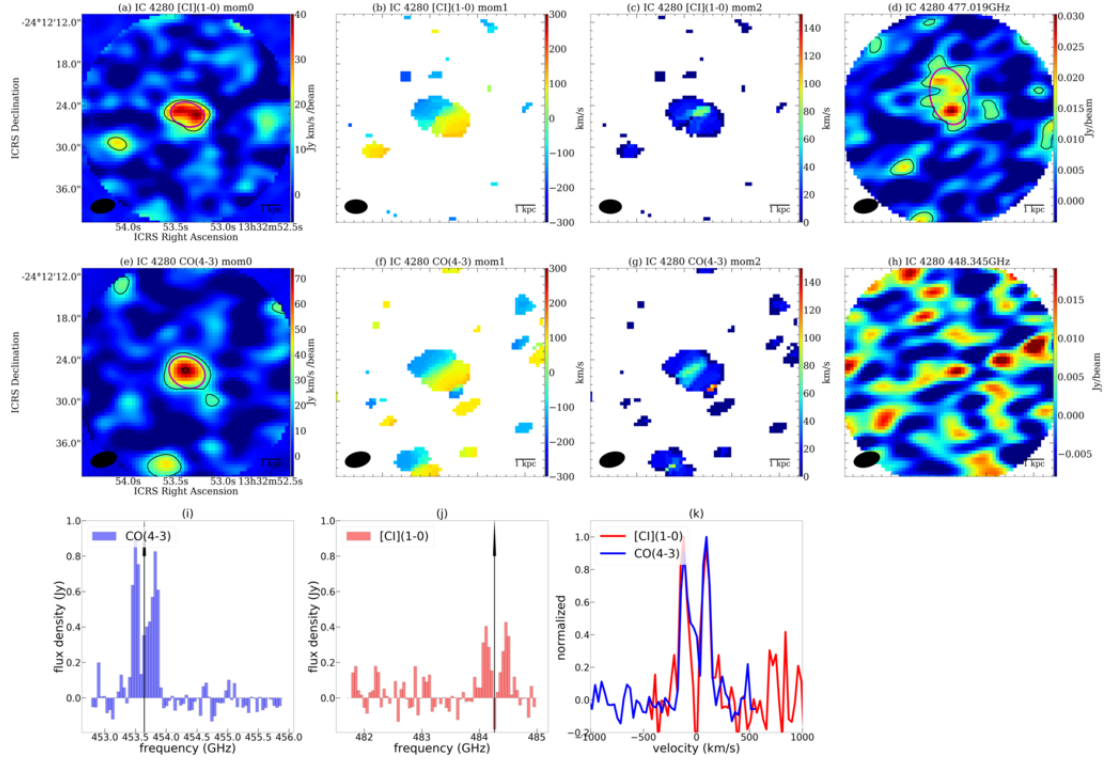


Figure A2.18. Same as Figure A2.1.

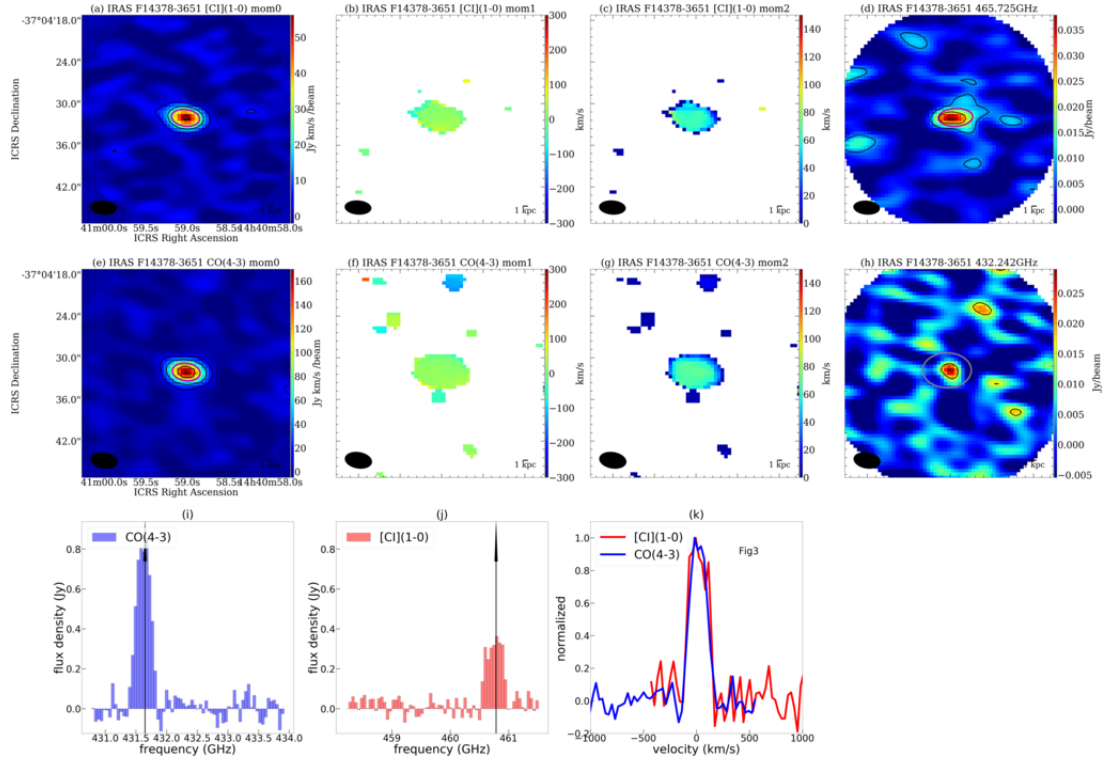


Figure A2.19. Same as Figure A2.1.

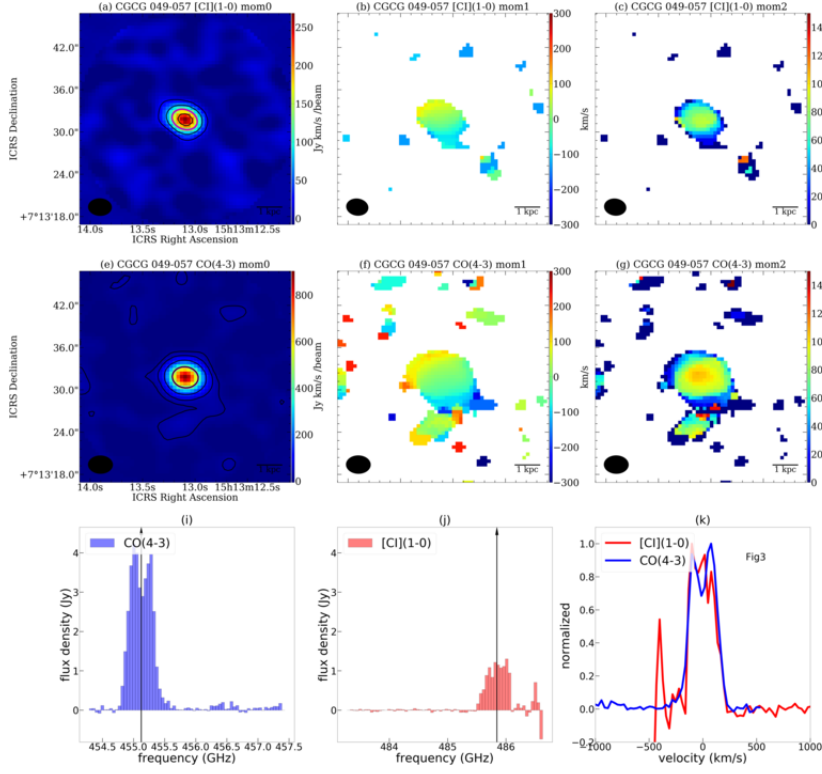


Figure A2.20. Same as Figure A2.1.

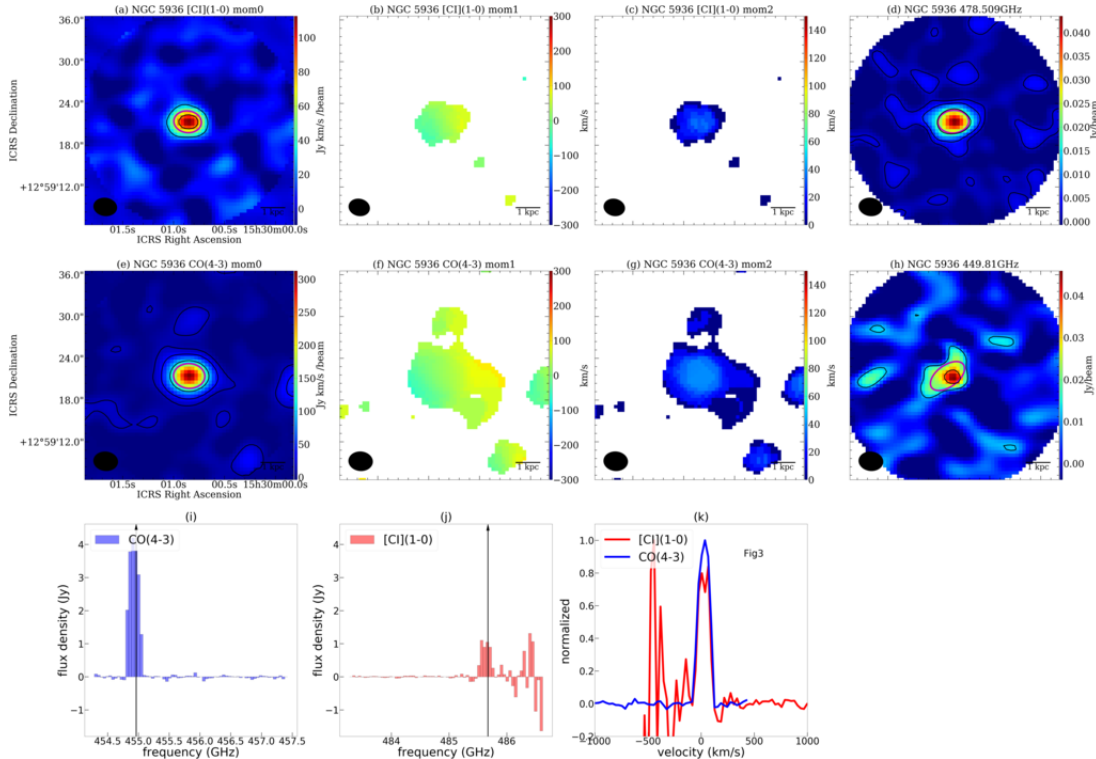


Figure A2.21. Same as Figure A2.1.

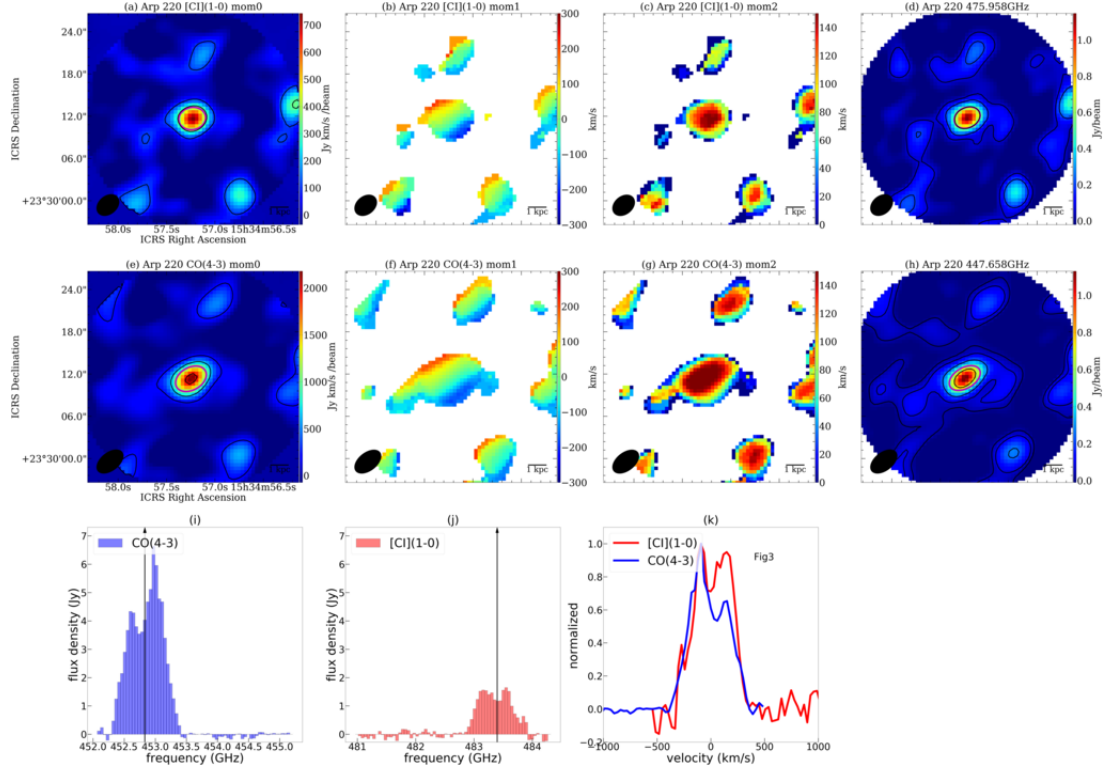


Figure A2.22. Same as Figure A2.1.

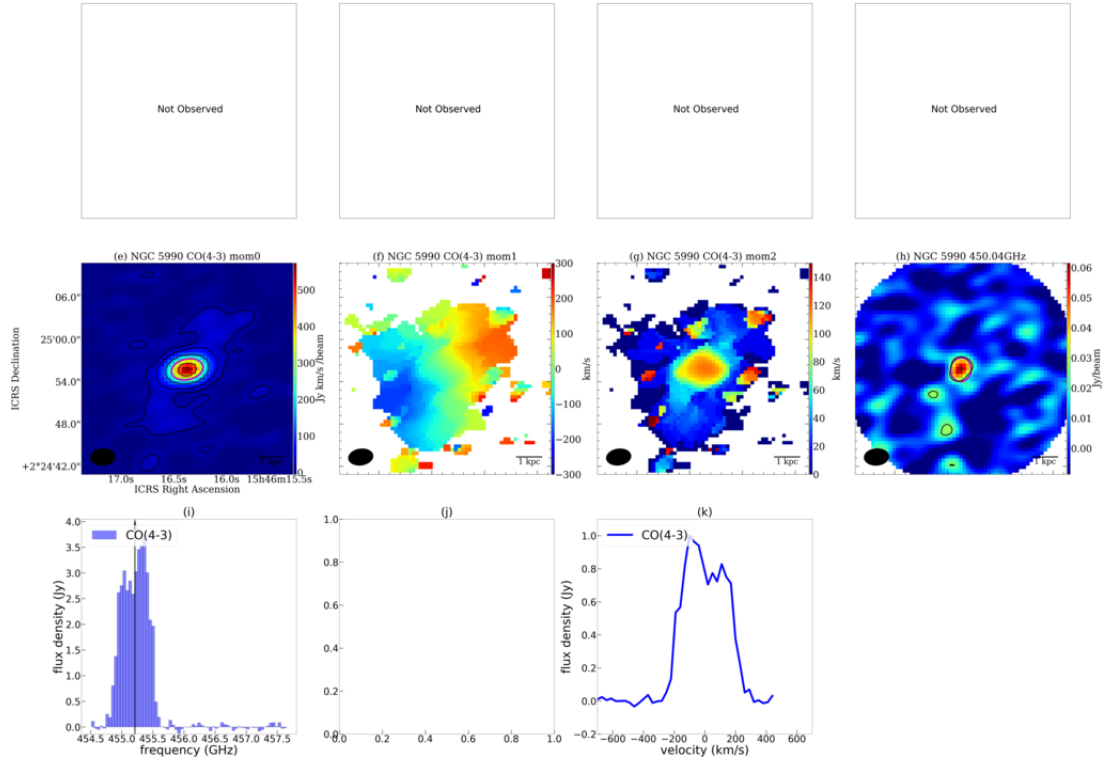


Figure A2.23. Same as Figure A2.1.

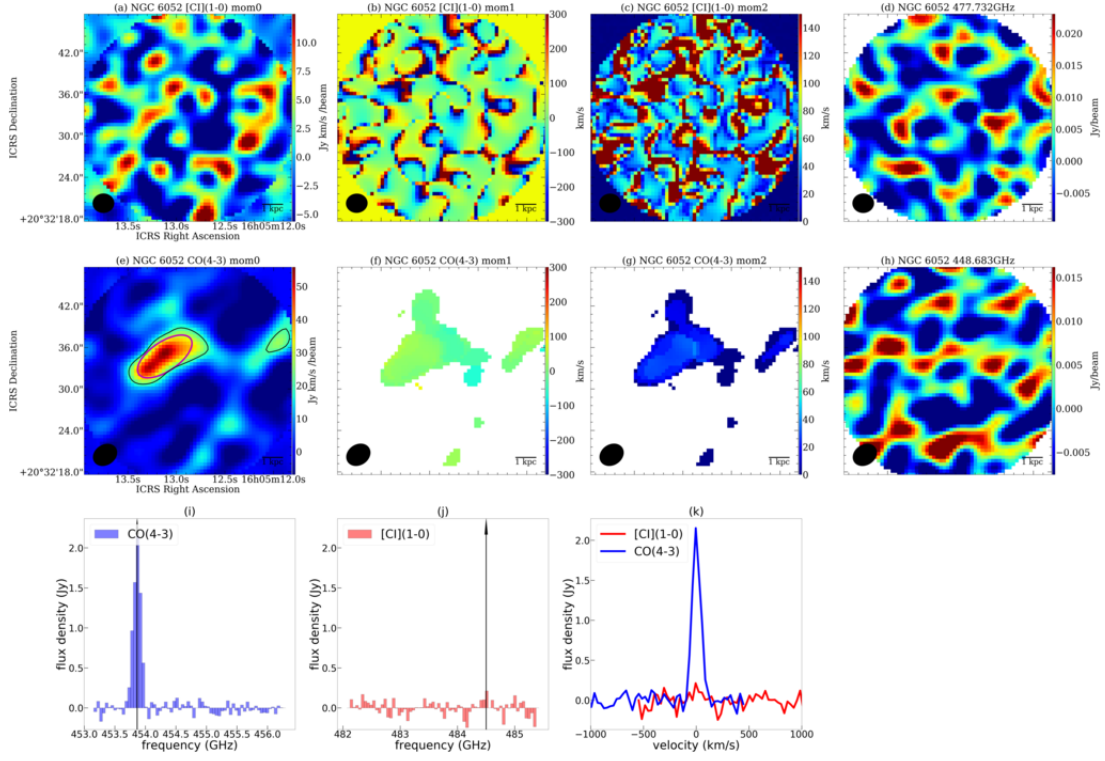


Figure A2.24. Same as Figure A2.1.

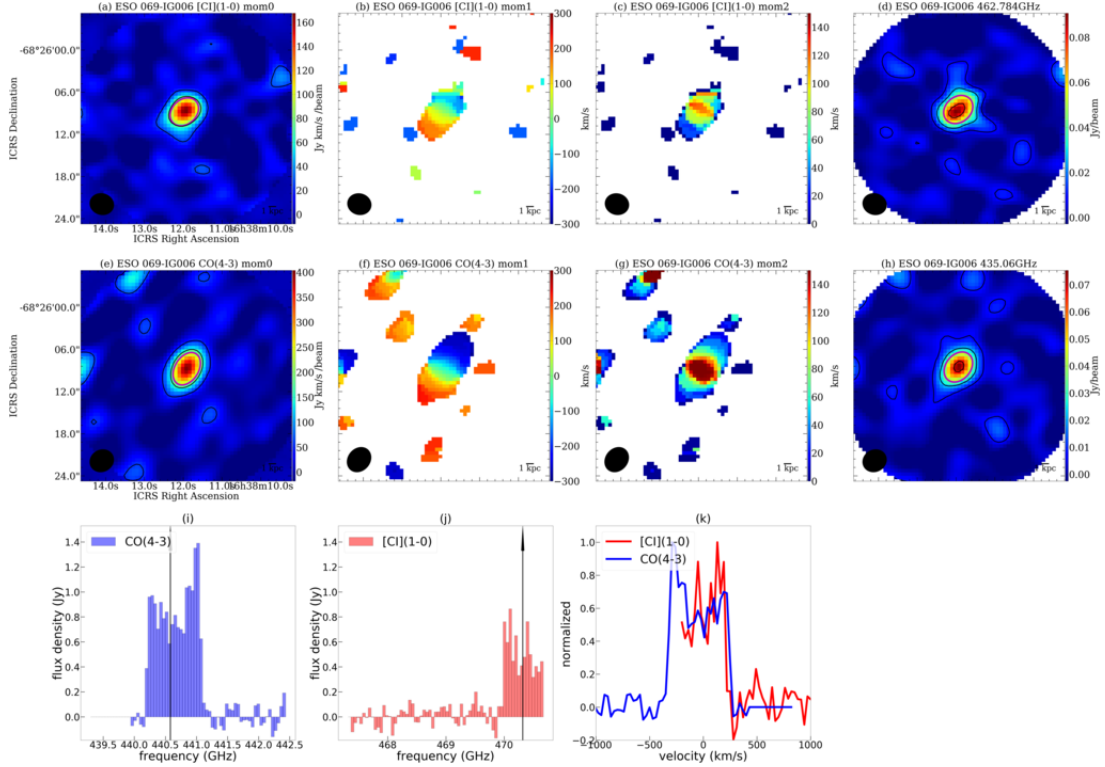


Figure A2.25. Same as Figure A2.1.



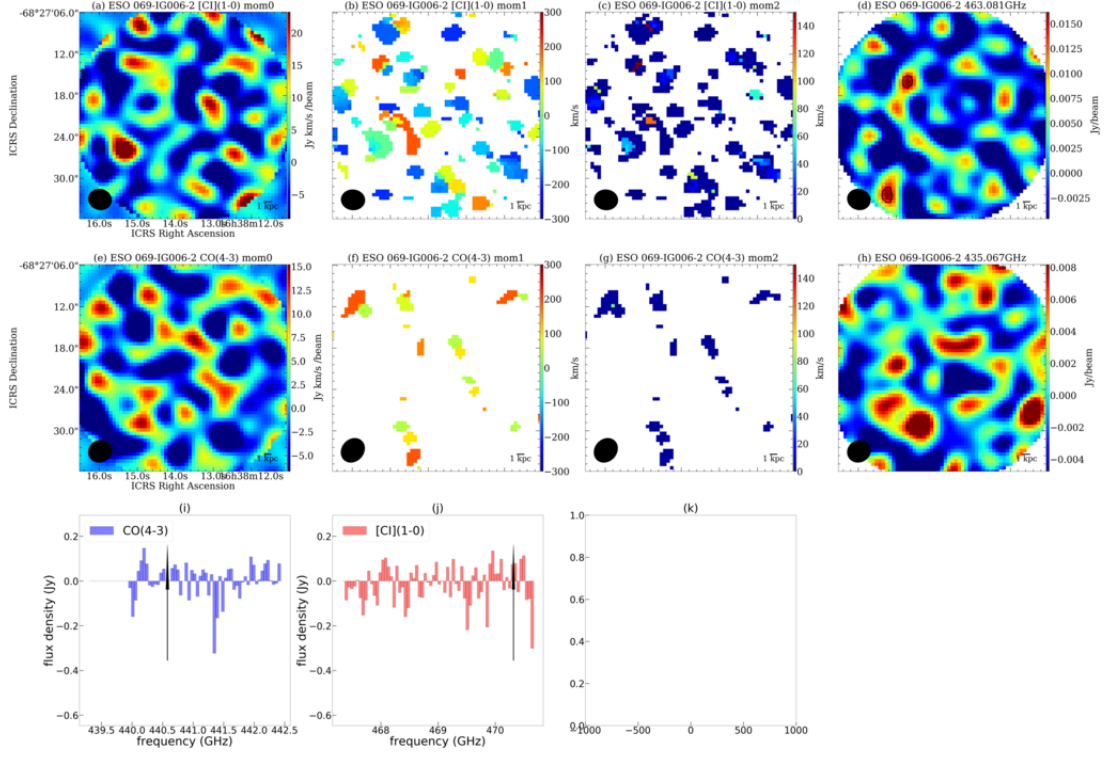


Figure A2.26. Same as Figure A2.1.

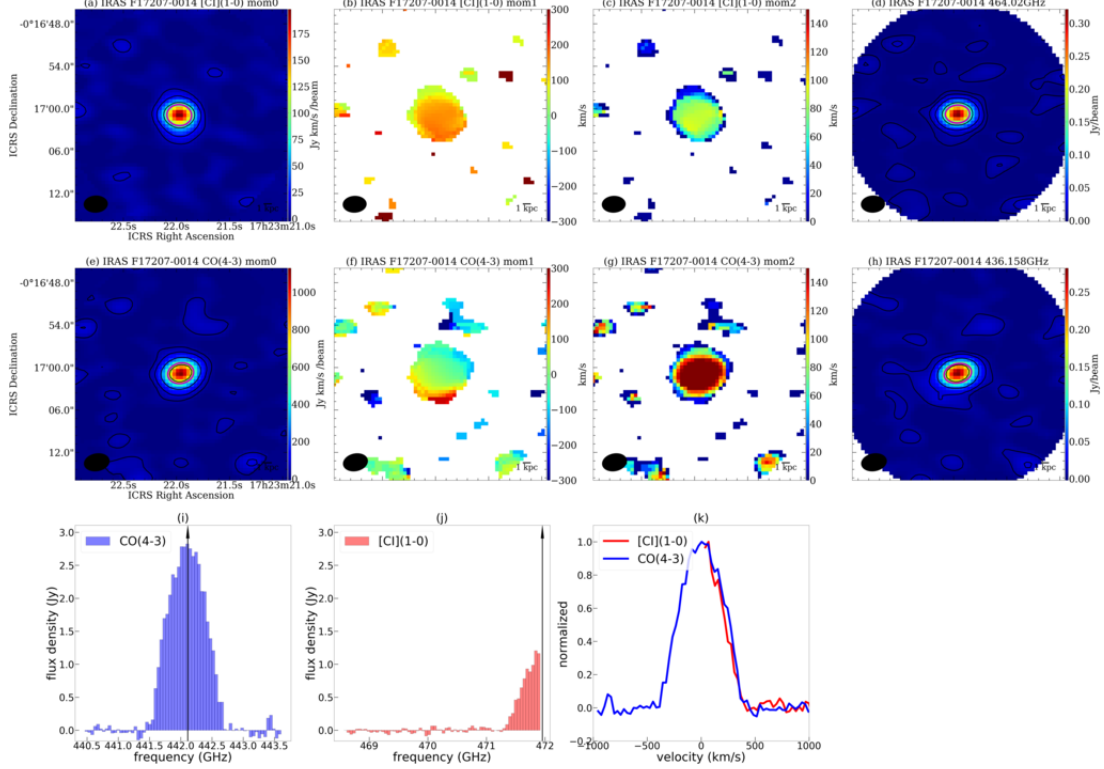


Figure A2.27. Same as Figure A2.1.

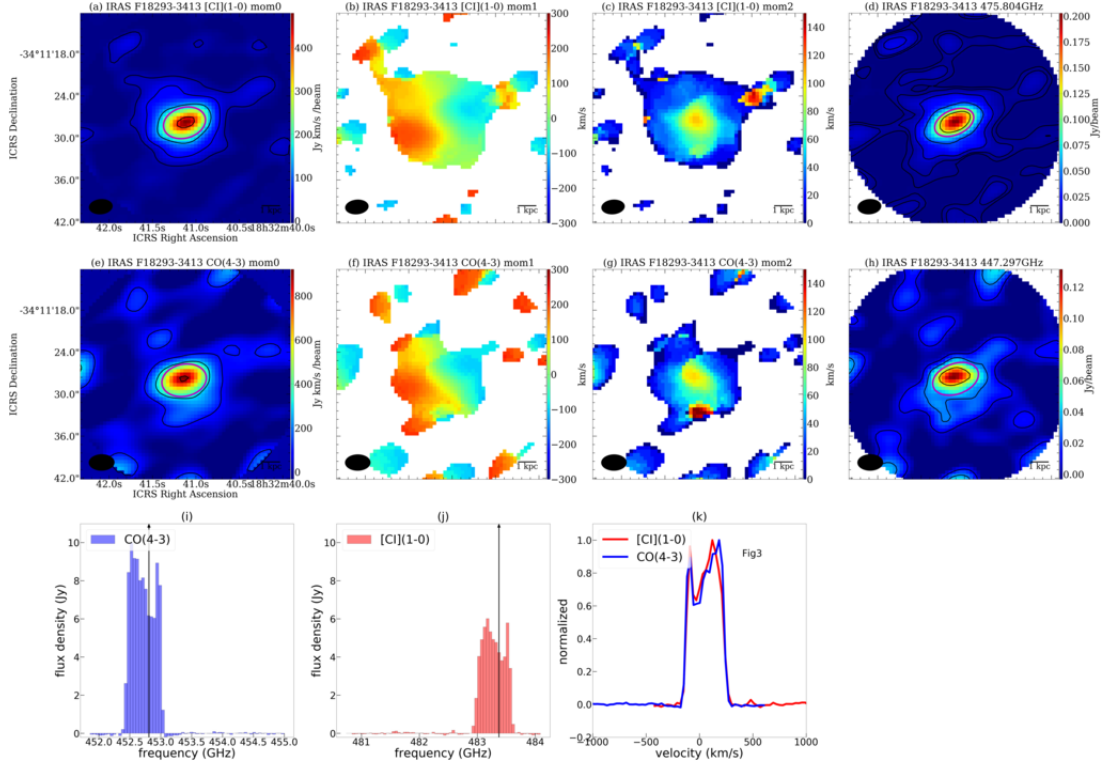


Figure A2.28. Same as Figure A2.1.

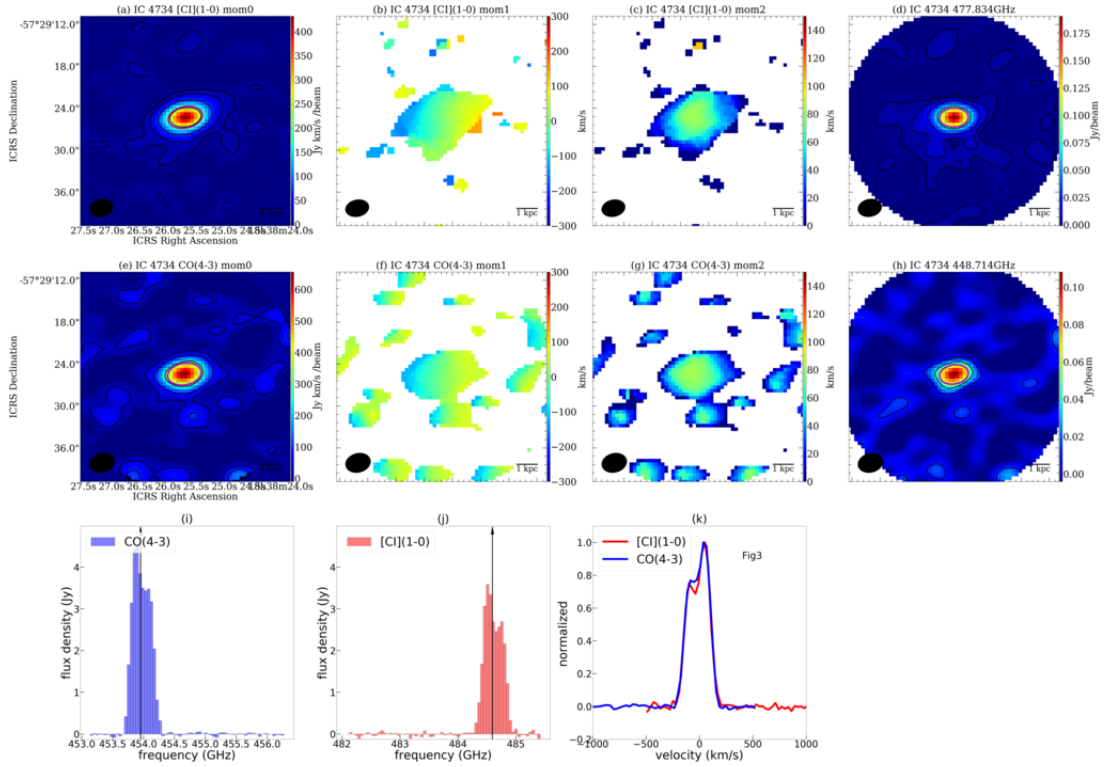


Figure A2.29. Same as Figure A2.1.



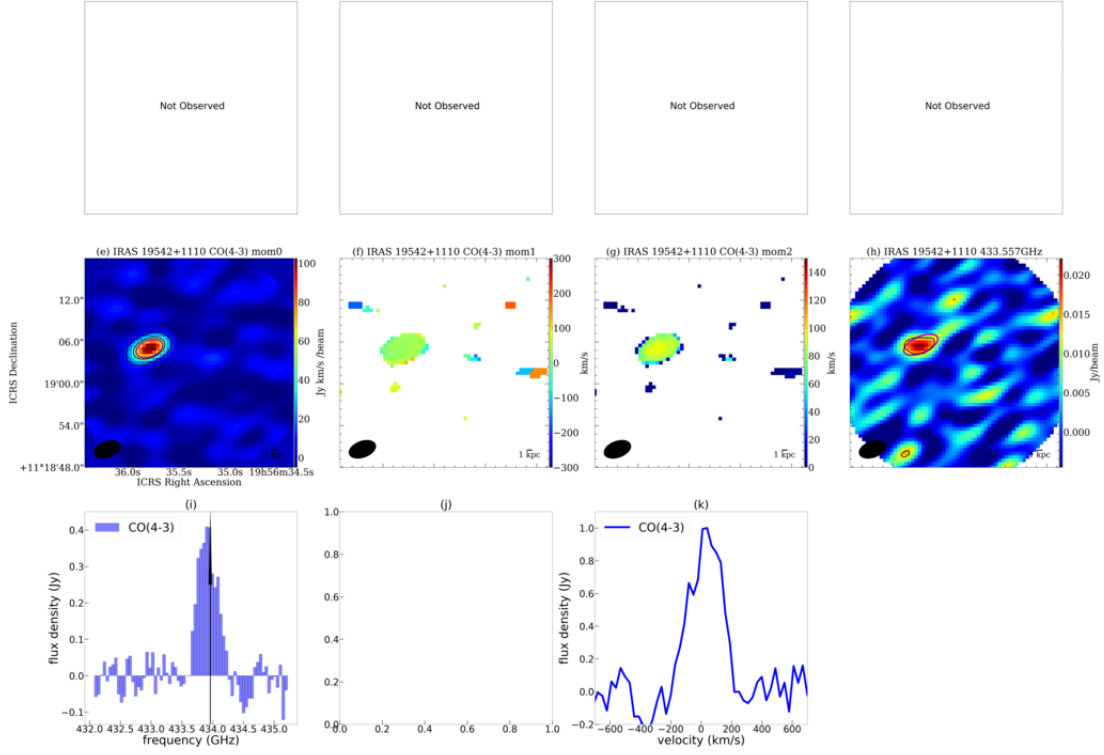


Figure A2.30. Same as Figure A2.1.

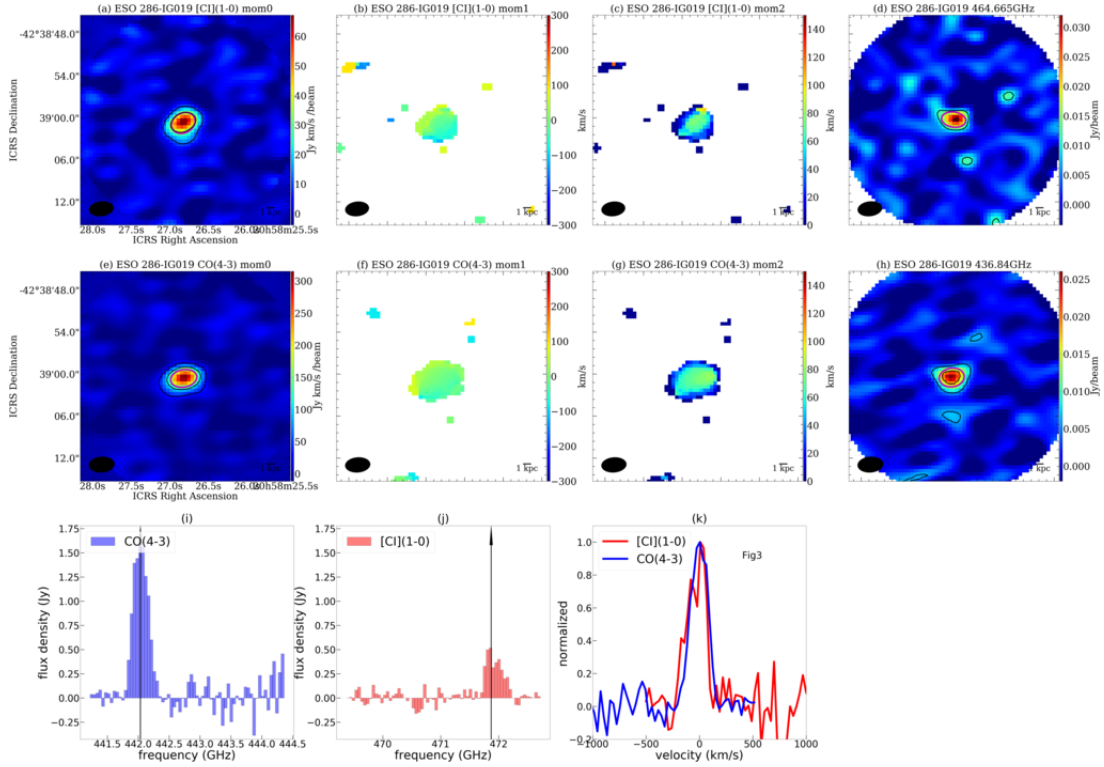


Figure A2.31. Same as Figure A2.1.

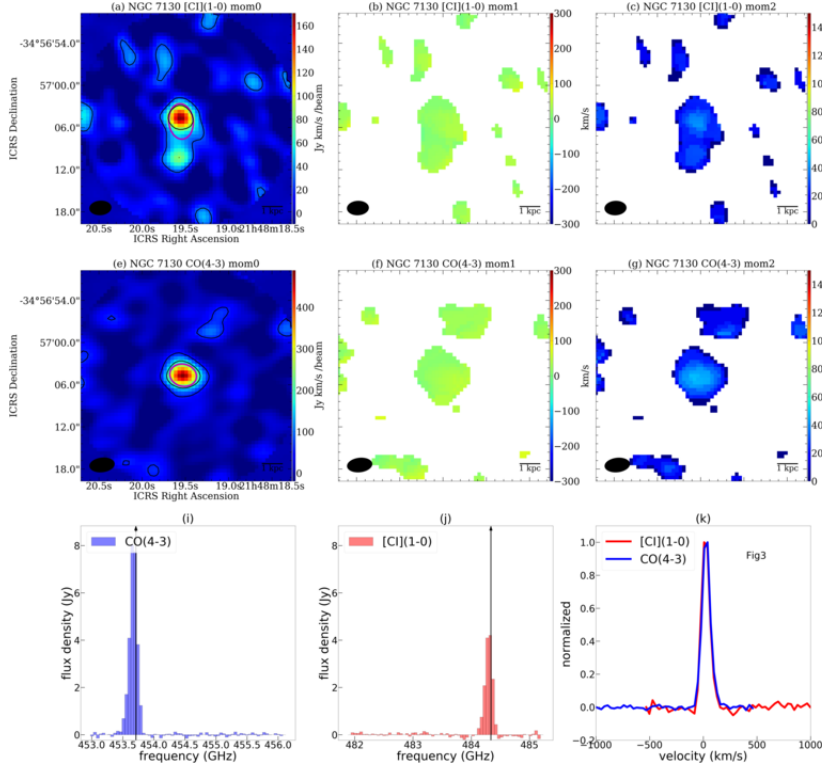


Figure A2.32. Same as Figure A2.1.

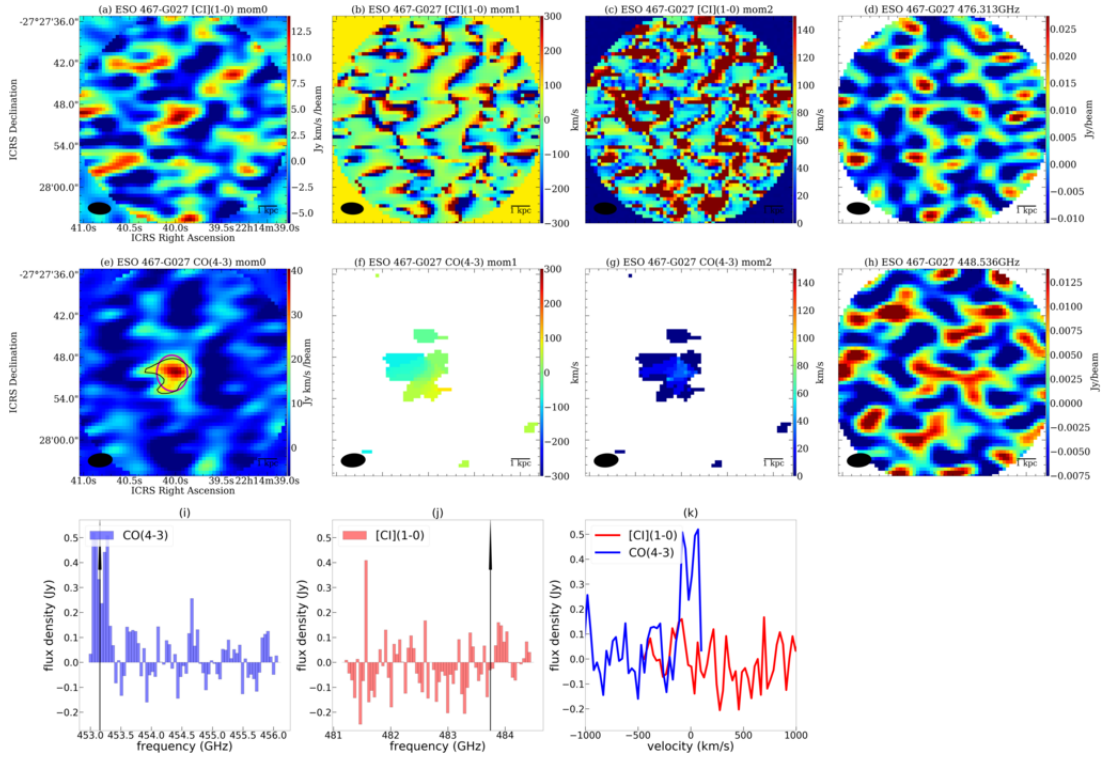


Figure A2.33. Same as Figure A2.1.

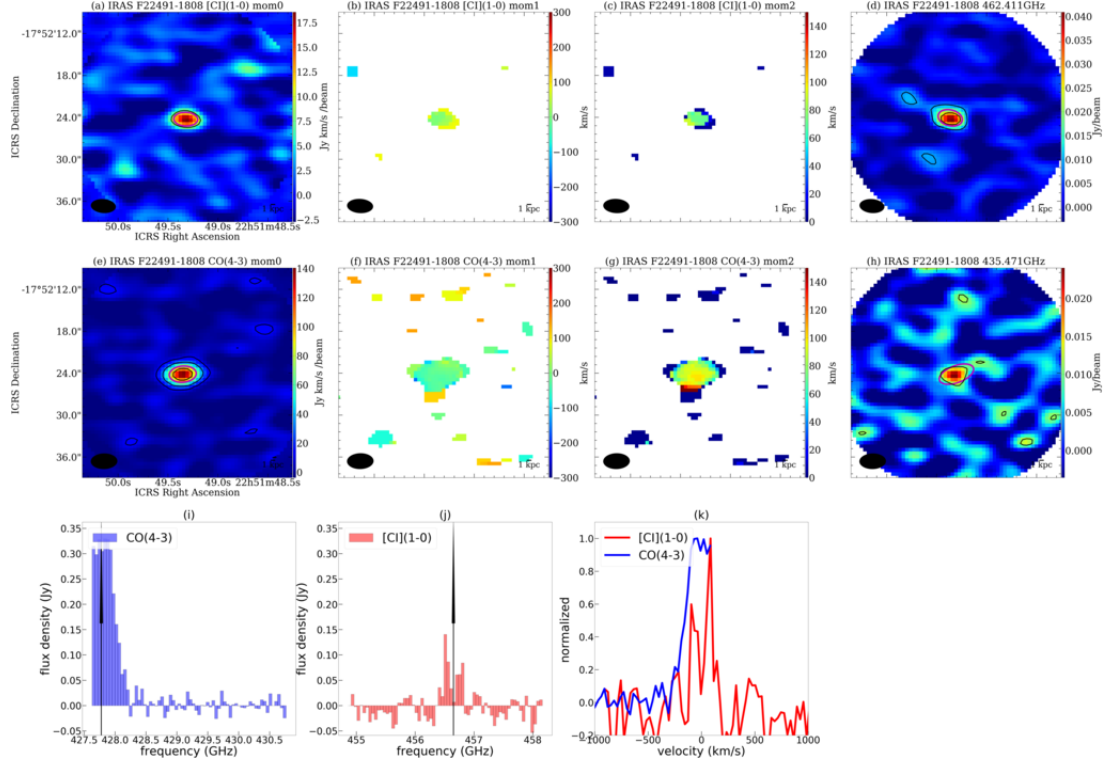


Figure A2.34. Same as Figure A2.1.

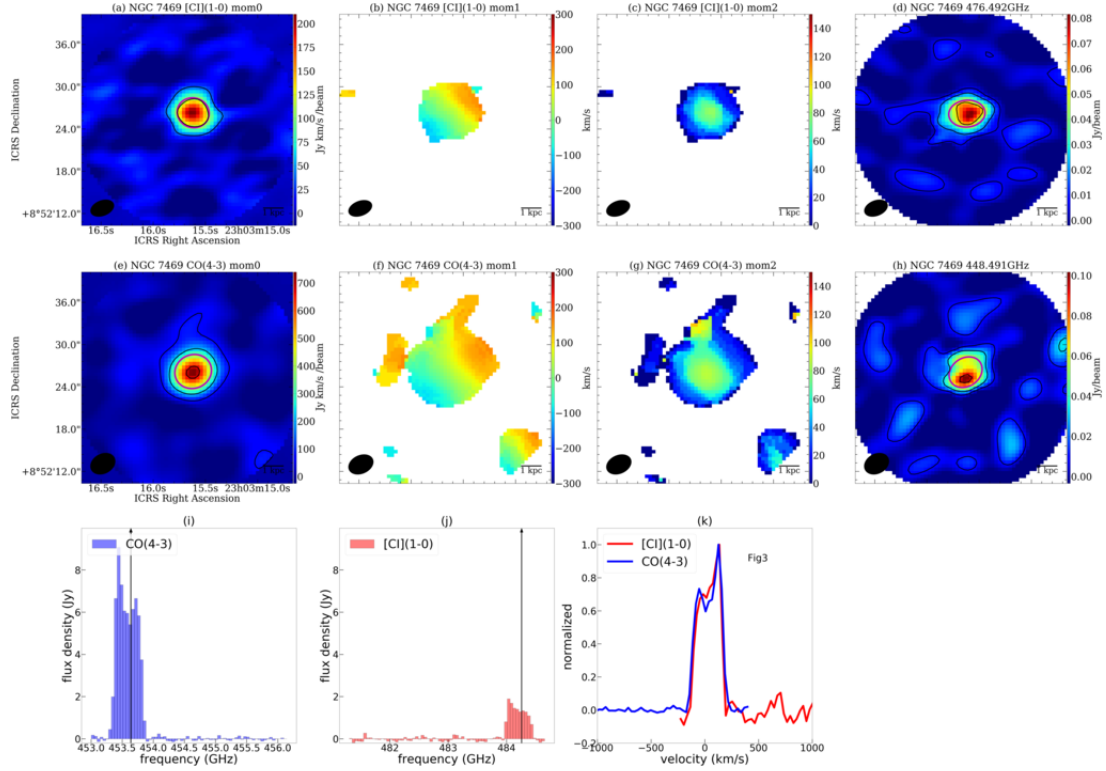


Figure A2.35. Same as Figure A2.1.

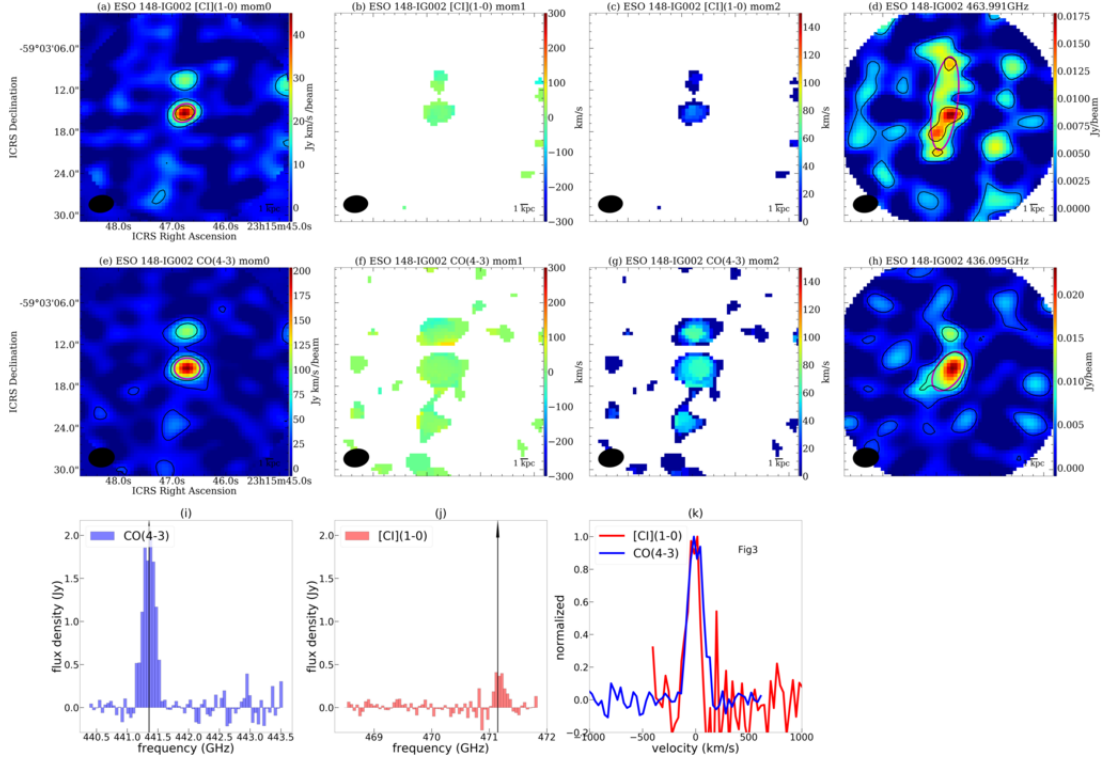


Figure A2.36. Same as Figure A2.1.

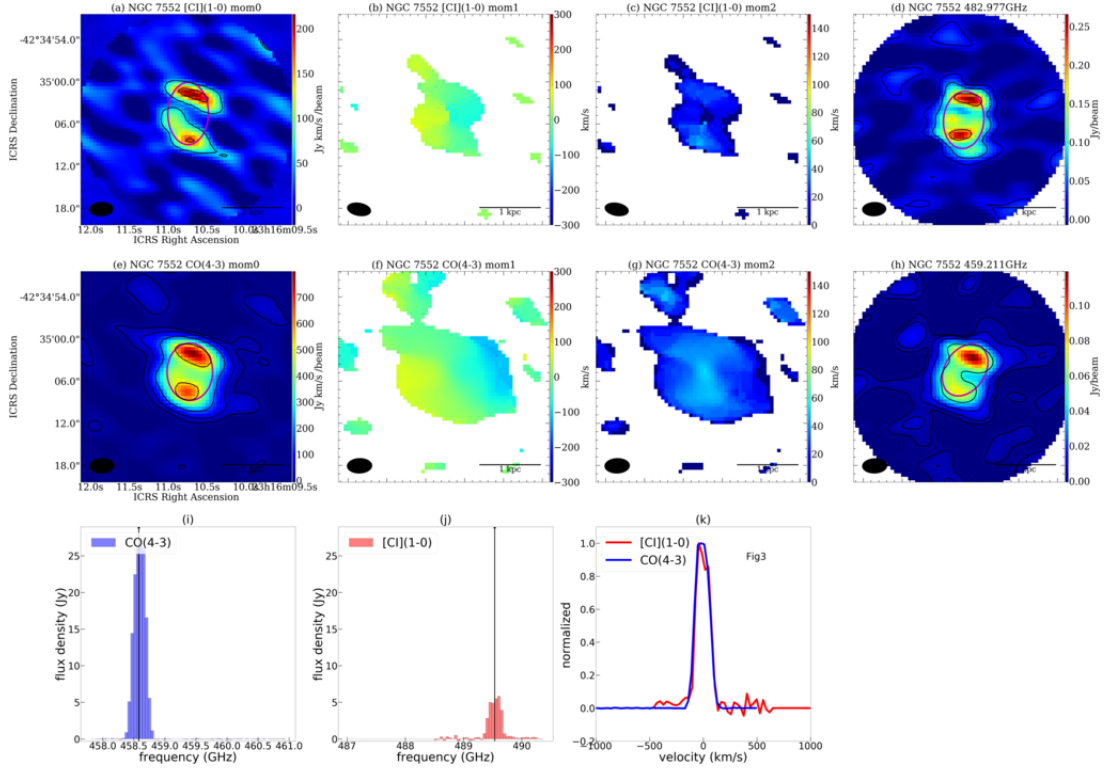


Figure A2.37. Same as Figure A2.1.

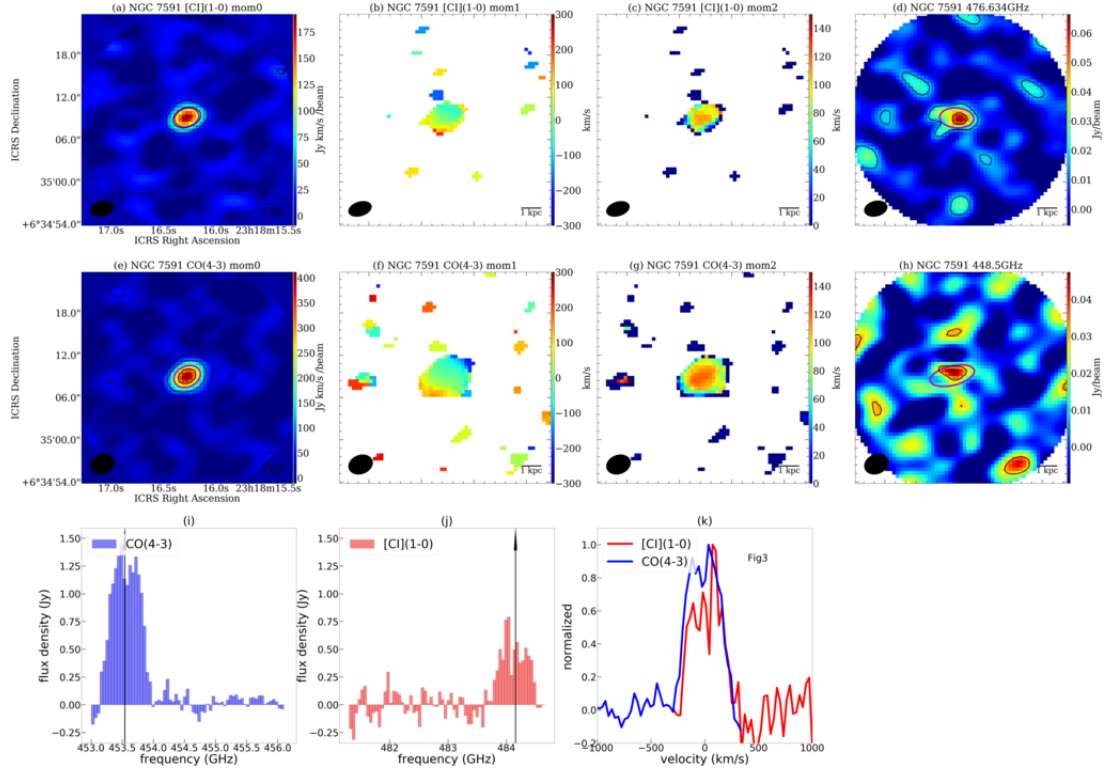


Figure A2.38. Same as Figure A2.1.

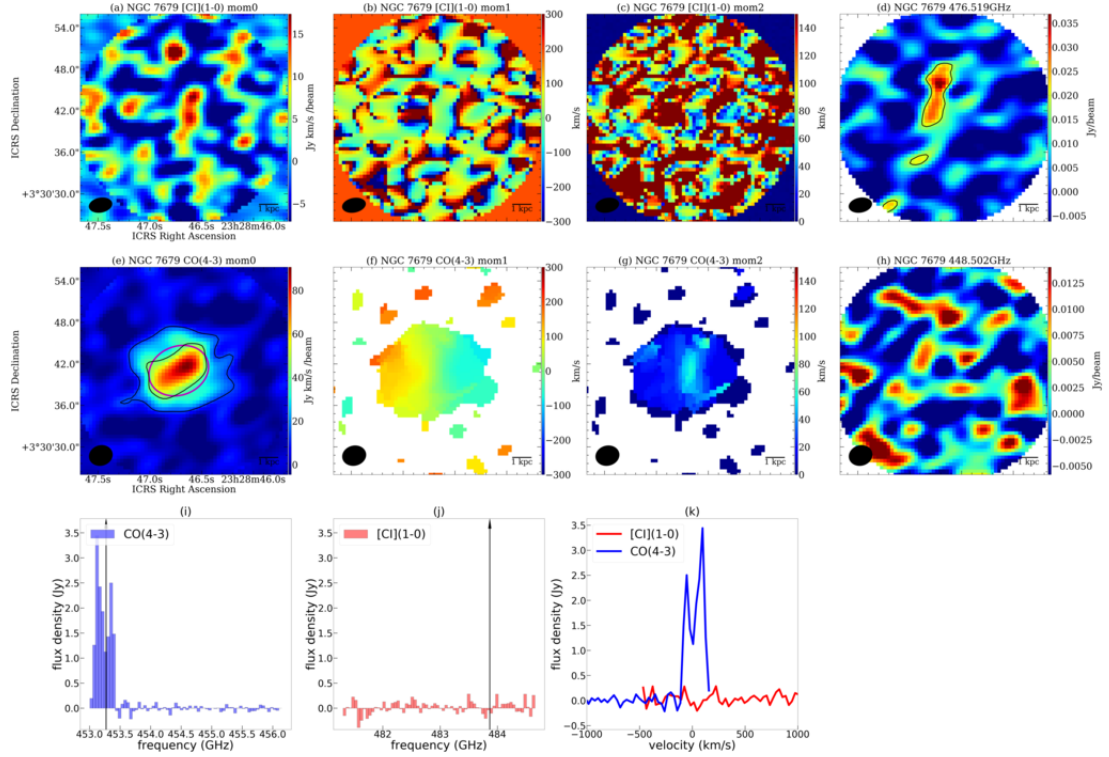


Figure A2.39. Same as Figure A2.1.



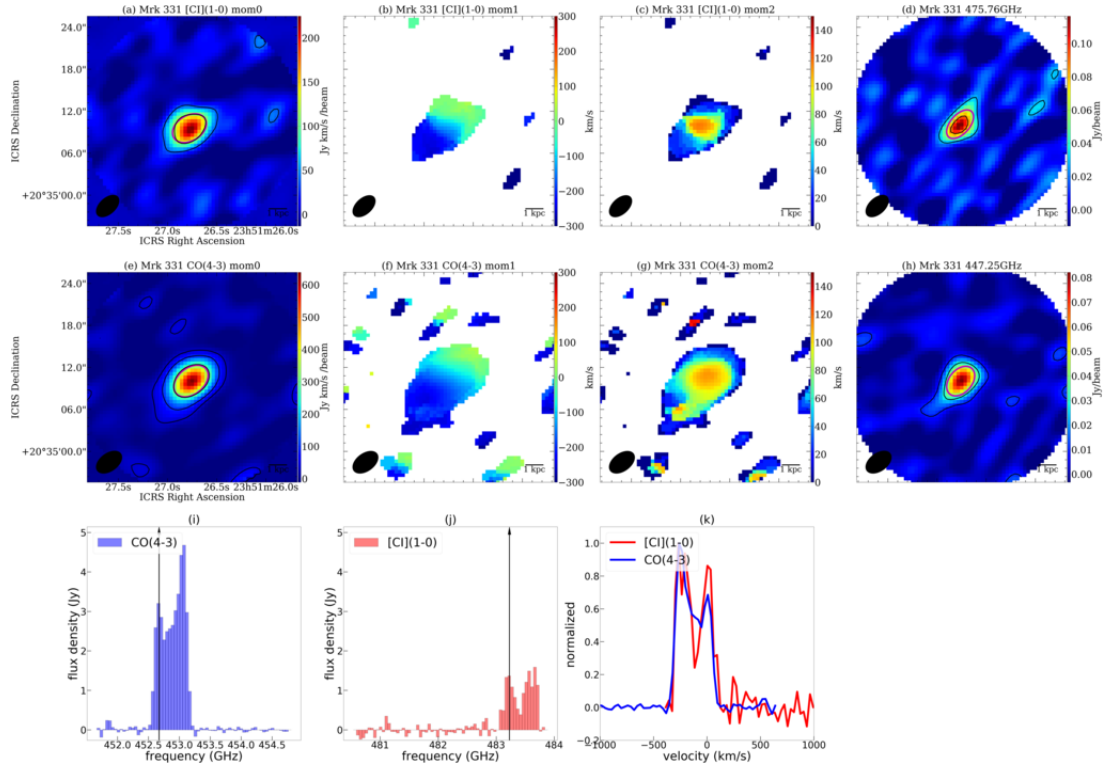


Figure A2.40. Same as Figure A2.1.

## A.2. Tables

Table A.1. Target list

Target Name	coordinates (ICRS)	redshift	$D_L$	$1''$	$V_{\text{sys}}$	CO (4-3) sky	[CI] (1-0) sky
	hmsdms		Mpc	kpc	km s $^{-1}$	GHz	GHz
(1)	(2)	(3)	(4)	(5)	(6)	(7)	(8)
NGC 232	00h42m45.8s -23d33m40.7s	0.0226	102	0.47	6637	450.8	481.3
NGC 232-2 (NGC 235)	00h42m52.9s -23d32m29.4s	—	—	—	—	—	—
NGC 232-3 (PGC 2570)	00h42m53.8s -23d32m44.3s	—	—	—	—	—	—
IC 1623	01h07m46.8s -17d30m25.7s	0.0201	90	0.42	5898	452.0	482.5
UGC 02982	04h12m22.7s +05d32m49.1s	0.0177	79	0.37	5213	453.0	483.6
NGC 1614	04h34m00.0s -08d34m44.6s	0.0159	71	0.34	4703	453.8	484.4
IRAS F05189-2524	05h21m01.4s -25d21m45.4s	0.0426	194	0.87	12239	442.2	472.1
IRAS 09022-3615	09h04m12.7s -36d27m00.8s	0.0596	276	1.19	16874	435.1	464.5
IRAS F09111-1007	09h13m36.4s -10d19m29.6s	0.0541	249	1.09	15397	437.4	466.9
NGC 3110	10h04m02.1s -06d28m29.1s	0.0169	76	0.35	4970	453.4	484.0
IRAS F10565+2448	10h59m18.1s +24d32m34.5s	0.0431	197	0.88	12387	442.0	471.8
IRAS F10565+2448-2	10h59m19.9s +24d32m45.7s	—	—	—	—	—	—
IRAS F12112+0305	12h13m46.1s +02d48m41.5s	0.0733	342	1.44	20478	429.5	458.5
NGC 4418	12h26m54.6s -00d52m39.5s	0.007	32	0.15	2094	457.7	488.6
ESO 507-G070	13h02m52.4s -23d55m17.7s	0.0217	98	0.45	6368	451.2	481.7
NGC 5104	13h21m23.1s +00d20m33.4s	0.0186	83	0.39	5476	452.6	483.2
NGC 5135	13h25m44.1s -29d50m01.2s	0.0137	61	0.29	4050	454.8	485.5
IC 4280	13h32m53.4s -24d12m25.8s	0.0163	73	0.34	4811	453.6	484.3
IRAS F14378-3651	14h40m59.0s -37d04m32.2s	0.0681	314	1.34	19112	431.8	461.0
CGCG 049-057	15h13m13.1s +07d13m31.9s	0.013	58	0.27	3847	455.1	485.8
NGC 5936	15h30m00.8s +12d59m21.6s	0.0134	60	0.28	3951	455.0	485.7
Arp 220	15h34m57.2s +23d30m11.6s	0.0181	81	0.38	5337	452.8	483.4
NGC 5990	15h46m16.4s +02d24m55.8s	0.0128	57	0.27	3791	455.2	485.9
NGC 6052	16h05m12.9s +20d32m32.6s	0.0158	71	0.33	4665	453.9	484.5
ESO 069-IG006	16h38m11.9s -68d26m09.8s	0.0464	213	0.94	13304	440.6	470.3
ESO 069-IG006-2	16h38m13.8s -68d27m20.9s	—	—	—	—	—	—
IRAS F17207-0014	17h23m22.0s -00d17m00.9s	0.0428	195	0.87	12307	442.1	472.0
IRAS F18293-3413	18h32m41.1s -34d11m27.2s	0.0182	81	0.38	5352	452.8	483.4
IC 4734	18h38m25.7s -57d29m25.8s	0.0156	70	0.33	4608	454.0	484.6
IRAS 19542+1110	19h56m35.4s +11d19m03.0s	0.0624	301	1.29	17608	432.9	462.1
ESO 286-IG019	20h58m26.8s -42d39m00.3s	0.043	196	0.87	12359	442.0	471.9
NGC 7130	21h48m19.5s -34d57m04.7s	0.0162	72	0.34	4765	453.7	484.3
ESO 467-G027	22h14m39.9s -27d27m50.2s	0.0174	78	0.37	5127	453.2	483.7
IRAS F22491-1808	22h51m49.3s -17d52m24.0s	0.0778	364	1.52	21630	427.8	456.7
NGC 7469	23h03m15.7s +08d52m25.3s	0.0163	73	0.34	4813	453.6	484.3
ESO 148-IG002	23h15m46.8s -59d03m15.9s	0.0446	204	0.91	12800	441.4	471.1
NGC 7552	23h16m10.8s -42d35m05.4s	0.0054	24	0.11	1600	458.6	489.5
NGC 7591	23h18m16.3s +06d35m08.8s	0.0165	74	0.35	4875	453.5	484.2
NGC 7679	23h28m46.7s +03d30m41.0s	0.0171	77	0.36	5052	453.3	483.9
Mrk 331	23h51m26.7s +20d35m10.6s	0.0185	83	0.39	5441	452.7	483.2

NOTE— (1) Target names. If the galaxy is the pair phase of a merger process, the companion's names are described as “-2” and “-3.” (2) Pointing center of the ACA observation. (3) The redshift is based on NED. In the case of IRAS F14378-3651, NGC 4418, and IRAS 19542+1110, the redshifts are based on [Rose et al. \(2018\)](#), [González-Alfonso et al. \(2012\)](#), and [Veilleux et al. \(2013\)](#), respectively. (4) Luminosity distance. (5) Physical scale corresponding to  $1''$ . (6) The systematic velocity calculated by  $V_{\text{sys}} = cz/(1+z)$ , where  $c$  is the speed of light). In the case of a pair of galaxies, we apply the same systematic velocity to identify the line emission. (7), (8) Observed sky frequencies of [C I] (1-0) and CO (4-3).



**Table A.2.** Supplemental data

Target Name	log SFR	log $M_{\text{dust}}$	$T_{\text{dust}}$	log $L_{\text{TIR}}$	AGN	Merger	$L'_{\text{CO}(1-0)}$
	$M_{\odot} \text{ yr}^{-1}$	$M_{\odot}$	K	$L_{\odot}$			$10^6 \text{ K km s}^{-1} \text{ pc}^2$
(1)	(2)	(3)	(4)	(5)	(6)	(7)	(8)
NGC 232	–	–	–	–	Y	Y	–
NGC 232-2 (NGC 235)	–	–	–	–	–	–	–
NGC 232-3 (PGC 2570)	–	–	–	–	–	–	–
IC 1623	1.67±0.02	8.27±0.02	27.5±0.7	11.6±0.02	N	Y	505±53
UGC 02982	1.27±0.04	8.31±0.09	23.6±0.6	11.21±0.05	N	Y	486±121
NGC 1614	1.76±0.03	7.91±0.04	32.1±1.0	11.7±0.03	N	Y	143±35
IRAS F05189-2524	1.89±0.05	8.19±0.05	34.4±1.1	11.82±0.05	Y	Y	1173±234
IRAS 09022-3615	2.28±0.03	8.6±0.04	34.4±1.0	12.22±0.04	Y	Y	–
IRAS F09111-1007	2.07±0.02	8.76±0.03	27.1±0.7	12.02±0.02	Y	Y	–
NGC 3110	–	–	–	–	N	Y	420±84
IRAS F10565+2448	2.14±0.03	8.45±0.01	31.2±0.8	12.09±0.01	N	Y	853±171
IRAS F10565+2448-2	2.14±0.03	8.45±0.01	31.2±0.8	12.09±0.01	–	–	–
IRAS F12112+0305	2.33±0.03	8.66±0.03	32.0±0.9	12.28±0.03	Y	Y	–
NGC 4418	–	–	–	–	Y	N	–
ESO 507-G070	1.59±0.04	8.03±0.05	30.1±0.8	11.52±0.04	–	Y	366±73
NGC 5104	1.32±0.02	8.22±0.03	25.4±0.6	11.27±0.02	N	N	317±71
NGC 5135	1.34±0.01	8.31±0.01	24.8±0.6	11.28±0.01	Y	N	516±103
IC 4280	1.21±0.01	8.3±0.03	24.1±0.5	11.15±0.02	–	N	373±93
IRAS F14378-3651	2.16±0.06	8.44±0.05	32.1±0.9	12.06±0.07	Y	Y	–
CGCG 049-057	1.39±0.04	8.02±0.06	28.0±0.8	11.34±0.05	Y	N	103±20
NGC 5936	1.2±0.01	8.17±0.02	24.6±0.6	11.14±0.01	N	N	232±46
Arp 220	2.35±0.07	8.82±0.08	28.6±1.6	12.29±0.08	Y	Y	1065±212
NGC 5990	1.16±0.01	7.98±0.02	25.3±0.6	11.1±0.02	Y	Y	239±59
NGC 6052	1.13±0.02	7.91±0.03	25.7±0.6	11.03±0.02	N	Y	180±44
ESO 069-IG006	–	–	–	–	–	Y	1861±372
ESO 069-IG006-2	–	–	–	–	–	–	–
IRAS F17207-0014	2.47±0.07	8.82±0.05	31.7±0.9	12.4±0.05	Y	Y	2296±460
IRAS F18293-3413	1.96±0.04	8.59±0.08	27.8±0.7	11.9±0.05	N	Y	1155±231
IC 4734	1.43±0.03	8.2±0.05	26.4±0.6	11.36±0.03	N	N	299±60
IRAS 19542+1110	2.06±0.04	8.36±0.04	33.7±1.0	11.99±0.04	Y	N	–
ESO 286-IG019	1.85±0.05	8.2±0.05	34.6±1.1	11.8±0.05	N	Y	670±13
NGC 7130	1.48±0.03	8.23±0.03	25.4±1.3	11.37±0.02	Y	N	231±26
ESO 467-G027	1.13±0.02	8.21±0.03	23.9±0.5	11.07±0.02	N	N	237±59
IRAS F22491-1808	–	–	–	–	–	–	716±142
NGC 7469	–	–	–	–	Y	Y	292±43
ESO 148-IG002	1.93±0.03	8.24±0.03	35.2±1.2	11.88±0.04	Y	Y	443±88
NGC 7552	–	–	–	–	–	–	77±7
NGC 7591	–	–	–	–	Y	N	300±60
NGC 7679	1.17±0.02	7.83±0.04	27.1±0.7	11.11±0.02	Y	Y	152±25
Mrk 331	–	–	–	–	Y	Y	109±21

NOTE— (1) Target names. (2)-(5) SFR,  $M_{\text{dust}}$ ,  $T_{\text{dust}}$ , and  $L_{\text{TIR}}$  estimated in [Shangguan et al. \(2019\)](#).  $L_{\text{TIR}}$  is for 8 - 1000  $\mu\text{m}$  and the AGN contribution has been subtracted. (6) Y and N represent AGN and non-AGN, respectively. (7) Y and N represent mergers and non-mergers, respectively. The classification of AGNs and mergers was from [Shangguan et al. \(2019\)](#). (8) CO (1–0) luminosity measured by [Kamenetzky et al. \(2016\)](#).

**Table A.3.** Observation log

Target Name	date	line	$T_{\text{sys}}$ (ave.)	$N_{\text{ant}}$	MRS (representative freq.)
	y/m/d		K		" (GHz)
(1)	(2)	(3)	(4)	(5)	(6)
Arp220, NGC 6052	2018/11/15	[C I] (1–0)	793	10	13.81 (484.53)
NGC 5104	2018/12/3	CO (4–3)	429	12	14.6 (452.66)
IRAS F14378-3651	2018/12/5	[C I] (1–0)	367	11	14.35 (460.62)
IRAS F22491-1808	2018/12/5	CO (4–3)	1243	12	15.42 (428.44)
IRAS 09022-3615	2019/1/12	[C I] (1–0)	949	11	14.23 (464.4)
NGC 5990	2019/1/13	CO (4–3)	1454	11	14.51 (455.25)
IRAS 09022-3615	2019/1/13	CO (4–3)	–	10	15.4 (434.32)
NGC 3110	2019/3/16	[C I] (1–0)	995	11	13.66 (483.84)
IRAS F12112+0305	2019/3/16	[C I] (1–0)	713	11	14.12 (458.48)
NGC 4418	2019/3/16	CO (4–3)	–	11	14.43 (457.76)
IRAS F10565+2448, IRAS F10565+2448-2	2019/3/20	[C I] (1–0)	525	12	14.03 (470.88)
NGC 4418	2019/3/20	[C I] (1–0)	–	12	13.52 (488.64)
IRAS F12112+0305	2019/3/20	CO (4–3)	470	12	15.38 (429.6)
IRAS 09022-3615	2019/3/24	[C I] (1–0)	1279	12	14.19 (465.82)
IRAS F14378-3651	2019/3/24	CO (4–3)	–	12	15.31 (431.6)
IRAS F18293-3413	2019/3/8	[C I] (1–0)	900	12	13.68 (483.16)
NGC 7552	2019/4/19	CO (4–3)	–	11	13.8 (458.25)
Arp220, NGC 6052	2019/4/21	[C I] (1–0)	1064	11	13.06 (484.53)
NGC 5990	2019/4/27	[C I] (1–0)	–	11	13.02 (485.96)
IRAS F09111-1007	2019/4/28	CO (4–3)	–	10	13.03 (435.72)
NGC 5990	2019/4/30	CO (4–3)	3808	9	12.47 (455.25)
IRAS F05189-2524	2019/5/12	[C I] (1–0)	325	11	13.43 (471.06)
NGC 1614	2019/5/12	CO (4–3)	544	11	13.94 (453.81)
CGCG 049-057, NGC 5936	2019/5/13	CO (4–3)	1014	11	13.91 (455.01)
IC 4734	2019/5/24	[C I] (1–0)	319	11	13.06 (484.5)
IRAS F09111-1007	2019/5/24	CO (4–3)	–	10	15.16 (435.72)
CGCG 049-057, NGC 5936	2019/5/24	[C I] (1–0)	789	11	13.03 (485.71)
IRAS F18293-3413	2019/5/24	[C I] (1–0)	264	11	13.1 (483.16)
IRAS F17207-0014	2019/5/24	[C I] (1–0)	216	11	13.43 (471.0)
IRAS F10565+2448, IRAS F10565+2448-2	2019/6/2	CO (4–3)	523	11	14.34 (441.12)
NGC 3110	2019/6/2	CO (4–3)	618	11	13.96 (453.26)
NGC 7469, NGC 7679, NGC 7591	2019/6/22	CO (4–3)	893	10	14.56 (453.74)
ESO 148-IG002	2019/6/22	CO (4–3)	680	11	14.34 (441.15)
UGC 02982	2019/6/22	[C I] (1–0)	587	10	13.67 (483.47)
NGC 1614	2019/6/22	[C I] (1–0)	702	10	13.64 (484.42)
NGC 1614	2019/6/22	CO (4–3)	896	10	14.56 (453.81)
UGC 02338	2019/6/22	CO (4–3)	742	10	14.55 (454.14)
NGC 7771, Mrk 331	2019/6/23	[C I] (1–0)	663	11	13.1 (482.96)
ESO 069-IG006, ESO_069-IG006-2	2019/6/23	CO (4–3)	715	11	14.38 (440.06)
NGC 5990	2019/6/23	CO (4–3)	4403	11	13.9 (455.25)
ESO 069-IG006, ESO 069-IG006-2	2019/6/23	[C I] (1–0)	600	11	13.47 (469.75)
NGC 7771, Mrk 331	2019/6/23	CO (4–3)	1079	11	13.99 (452.44)
IC 4734	2019/6/23	CO (4–3)	1998	11	13.94 (453.88)
NGC 5135, IC 4280, ESO 507-G070	2019/6/24	CO (4–3)	1256	11	13.91 (454.75)
NGC 5990	2019/6/24	CO (4–3)	2777	11	13.9 (455.25)
ESO 069-IG006, ESO 069-IG006-2	2019/6/24	[C I] (1–0)	420	11	13.47 (469.75)
NGC 7771, Mrk 331	2019/6/24	CO (4–3)	1566	11	13.99 (452.44)
IC 4734	2019/6/24	CO (4–3)	734	11	13.94 (453.88)
IRAS F18293-3413	2019/6/24	CO (4–3)	587	11	13.98 (452.62)
ESO 069-IG006, ESO 069-IG006-2	2019/6/24	CO (4–3)	771	11	14.38 (440.06)
NGC 7771, Mrk 331	2019/6/24	[C I] (1–0)	1197	11	13.1 (482.96)

**Table A.3** *continued*

**Table A.3** (*continued*)

Target Name	date	line	$T_{\text{sys}}$ (ave.)	$N_{\text{ant}}$	MRS (representative freq.)
	y/m/d		K		" (GHz)
(1)	(2)	(3)	(4)	(5)	(6)
NGC 5104	2019/6/3	[C I] (1–0)	682	11	13.68 (483.2)
NGC 5135, IC 4280, ESO 507-G070	2019/6/3	[C I] (1–0)	83	11	13.3 (485.42)
IRAS F17207-0014	2019/6/3	CO (4–3)	410	11	14.34 (441.24)
Arp 220, NGC 6052	2019/6/3	CO (4–3)	697	11	13.94 (453.91)
ESO 467-G027, NGC 7130	2019/6/6	[C I] (1–0)	734	10	11.74 (483.57)
IRAS 05442+1732	2019/6/6	[C I] (1–0)	674	9	11.75 (483.08)
ESO 286-IG019	2019/6/7	CO (4–3)	607	9	12.85 (441.99)
ESO 467-G027, NGC 7130	2019/6/7	CO (4–3)	625	9	12.51 (453.71)
ESO 148-IG002	2019/6/7	[C I] (1–0)	452	9	12.06 (470.91)
ESO 286 IG019	2019/6/7	[C I] (1–0)	445	9	12.03 (471.81)
IRAS 19542+1110	2019/6/8	CO (4–3)	–	9	13.12 (432.88)
NGC 232, NGC 232-2, NGC 232-3, IC 1623	2019/6/8	[C I] (1–0)	471	9	11.77 (482.22)
IRAS 19542+1110	2019/6/8	[C I] (1–0)	1062	9	12.3 (461.99)
NGC 7552	2019/6/8	CO (4–3)	–	9	12.38 (458.25)
IRAS F22491-1808	2019/6/8	[C I] (1–0)	417	9	12.42 (457.25)
NGC 7469, NGC 7679, NGC 7591	2019/6/8	[C I] (1–0)	650	9	11.74 (483.74)
NGC 7552	2019/6/8	[C I] (1–0)	–	9	11.6 (489.45)
IC 4734	2019/7/28	CO (4–3)	1642	11	13.94 (453.88)
IC 4734	2019/7/29	CO (4–3)	802	10	14.56 (453.88)
NGC 5135, IC 4280, ESO 507-G070	2019/7/31	[C I] (1–0)	1461	11	13.3 (485.42)
IRAS 05442+1732	2019/7/5	CO (4–3)	529	9	12.54 (452.55)
NGC 7771, Mrk 331	2019/7/5	CO (4–3)	739	10	14.61 (452.44)
NGC 5135, IC 4280, ESO 507-G070	2019/7/6	CO (4–3)	879	10	10.27 (454.75)
NGC 232, NGC 232-2, NGC 232-3, IC 1623	2019/7/6	[C I] (1–0)	379	10	9.68 (482.22)
NGC 5135, IC 4280, ESO 507-G070	2019/8/13	[C I] (1–0)	737	11	13.3 (485.42)
IRAS F05189-2524	2019/8/20	CO (4–3)	559	11	14.34 (441.29)
NGC 232, NGC 232-2, NGC 232-3, IC 1623	2019/8/5	CO (4–3)	640	10	12.57 (451.75)
NGC 232, NGC 232-2, NGC 232-3, IC 1623	2019/8/6	CO (4–3)	745	10	12.57 (451.75)

NOTE— (1) Target names. (2) Date of observation. (3) Observed line. (4) Typical systematic temperature. If the systematic temperature is not shown in QA0 report, the value is shown as “–.” (5) Number of antennas. (6) MRS scale shown in the QA0 report.

**Table A.4.** Imaging results

Target Name	Beam	Beam	rms (cube)	rms (cube)	rms	rms	rms	v-range	v-range
	CO (4–3)	[C I] (1–0)	CO (4–3)	[C I] (1–0)	CO (4–3)	[C I] (1–0)	cont	CO (4–3)	[C I] (1–0)
	( " , " )	( " , " )	*1	*1	*2	*2	*1	km s <sup>–1</sup>	km s <sup>–1</sup>
(1)	(2)	(3)	(4)	(5)	(6)	(7)	(8)	(9)	(10)
NGC 232	3.4×2.2	3.4×2.0	63	29	14	4	3.4,3.2	[–220,290]	[–190,350]
NGC 232-2 (NGC 235)	3.4×2.2	3.3×2.0	45	28	4	4	3.7,2.5	[–310,–160]	[–280,140]
NGC 232-3 (PGC 2570)	3.4×2.2	3.3×2.0	80	35	10	5	6.4,4.2	ND	ND
IC 1623	4.0×2.2	3.5×2.0	64	25	17	4	4.2,3.5	[–210,240]	[–190,170]
UGC 02982	–	3.2×2.7	–	33	–	4	–,5.7	–	[–150,210]
NGC 1614	3.5×2.4	3.3×2.6	56	47	11	7	4.5,5.4	[–190,200]	[–160,200]
IRAS F05189-2524	4.8×2.2	3.5×2.3	58	33	9	3	3.5,3.6	[–20,220]	[100,250]
IRAS 09022-3615	4.7×2.1	3.8×2.1	31	36	15	8	7.0,15.2	[–450,360]	[–220,260]
IRAS F09111-1007	3.6×2.3	3.6×2.1	58	21	10	1	3.9,3.3	[–50,190]	[120,240]
NGC 3110	3.5×2.3	3.5×1.8	46	57	11	8	2.4,10.4	[–130,230]	[–110,220]

**Table A.4** *continued*

Table A.4 (continued)

Target Name	Beam	Beam	rms (cube)	rms (cube)	rms	rms	rms	v-range	v-range
	CO (4–3)	[C I] (1–0)	CO (4–3)	[C I] (1–0)	CO (4–3)	[C I] (1–0)	cont	CO (4–3)	[C I] (1–0)
	( $''$ , $''$ )	( $''$ , $''$ )	*1	*1	*2	*2	*1	km s $^{-1}$	km s $^{-1}$
(1)	(2)	(3)	(4)	(5)	(6)	(7)	(8)	(9)	(10)
IRAS F10565+2448	3.6×3.1	3.5×2.8	60	34	12	2	5.8,2.2	[-150,180]	[60,150]
IRAS F10565+2448-2	3.8×3.0	3.4×2.9	45	38	6	4	4.1,3.2	ND	ND
IRAS F12112+0305	3.6×2.5	3.9×2.5	14	28	4	7	4.0,6.3	[-450,210]	[-350,370]
NGC 4418	4.1×2.1	3.2×2.1	25	33	6	4	2.5,3.0	[-280,290]	[-100,140]
ESO 507-G070	5.1×2.3	3.4×2.1	79	25	28	6	3.1,5.4	[-400,260]	[-360,240]
NGC 5104	3.8×2.2	3.6×2.0	27	33	4	7	2.6,5.7	[-320,340]	[-260,310]
NGC 5135	3.6×2.2	3.5×2.1	98	76	13	10	1.7,3.6	[-80,160]	[-60,120]
IC 4280	3.8×2.2	3.3×2.1	60	41	8	6	8.0,3.5	[-120,180]	[-150,180]
IRAS F14378-3651	3.9×2.4	3.8×2.0	23	17	5	2	5.4,2.8	[-140,220]	[-70,170]
CGCG 049-057	3.5×2.6	3.1×2.4	30	52	5	8	4.7,0.7	[-310,260]	[-100,230]
NGC 5936	3.5×2.8	3.1×2.5	52	84	4	9	3.9,0.7	[-50,130]	[-20,130]
Arp 220	4.4×2.6	3.5×2.6	141	101	73	36	9.4,20.7	[-390,420]	[-300,360]
NGC 5990	3.6×2.4	–	25	–	5	–	8.7,–	[-220,290]	–
NGC 6052	3.7×3.0	3.1×2.8	51	67	7	6	7.6,9.4	[-30,120]	ND
ESO 069-IG006	3.8×3.2	3.5×3.0	73	61	18	8	2.5,2.9	[-290,280]	[-170,250]
ESO 069-IG006-2	3.8×3.2	3.5×3.0	49	71	7	9	4.8,4.6	ND	ND
IRAS F17207-0014	3.5×2.5	3.4×2.4	36	16	8	3	2.1,1.4	[-350,430]	[70,400]
IRAS F18293-3413	3.6×2.3	3.3×2.1	174	31	33	5	3.2,0.5	[-120,300]	[-120,300]
IC 4734	3.7×2.8	3.4×2.4	56	29	10	3	4.1,0.9	[-170,190]	[-160,200]
IRAS 19542+1110	4.1×2.4	–	23	–	5	–	4.5,–	[-140,220]	–
ESO 286-IG019	3.6×2.1	3.4×2.1	53	32	12	4	2.0,3.5	[-150,150]	[-140,130]
NGC 7130	3.6×2.0	3.1×2.0	102	75	19	9	6.1,8.4	[-50,190]	[-20,160]
ESO 467-G027	3.6×2.0	3.3×1.7	57	51	6	6	7.5,10.9	[-50,130]	ND
IRAS F22491-1808	3.8×2.2	3.7×2.0	28	23	4	3	3.6,3.1	[-220,170]	[-70,110]
NGC 7469	3.7×2.6	3.5×2.1	86	64	25	13	3.4,2.1	[-110,250]	[-100,260]
ESO 148-IG002	3.7×2.6	3.6×2.5	59	52	8	3	0.9,1.2	[-80,160]	[-40,80]
NGC 7552	3.6×2.2	3.4×1.9	53	137	7	19	0.6,7.2	[-110,160]	[-100,140]
NGC 7591	3.5×2.7	3.4×2.0	59	61	11	9	9.9,5.6	[-240,270]	[-170,250]
NGC 7679	3.5×2.9	3.4×2.1	40	70	5	7	5.8,6.2	[-50,220]	ND
Mrk 331	4.1×2.6	3.9×2.3	45	69	11	13	3.3,9.7	[-320,130]	[-270,90]

NOTE— (1) Target names. (2) and (3) The achieved synthesized beam. (4) and (5) The achieved sensitivity of channel maps in units of mJy beam $^{-1}$  (\*1). (6) and (7) The achieved sensitivity of the velocity integrated intensity map in the unit of Jy beam $^{-1}$  km s $^{-1}$  (\*2). (8) The achieved sensitivity of continuum emission in units of mJy beam $^{-1}$  (\*1). The left value is for the CO (4–3) scheduling block and the right value is for the [C I] (1–0) scheduling block. (9) and (10) The velocity range for the velocity-integrated intensity map. The values represent relative velocities with respect to the systematic velocity. The “–” means that the emission is on the edge of the spectral window due to incorrect redshift. “ND” indicates the non-detection.

Table A.5. Line flux

Target Name	$S_{\text{line}}\Delta v$	$S_{\text{line}}\Delta v$	FWHM	FWHM	$S_{\text{line}}dv$	size (FWHM)	size (FWHM)
	CO (4–3)	[C I] (1–0)	CO (4–3)	[C I] (1–0)	CO (1–0)	CO (4–3)	[C I] (1–0)
	Jy km s $^{-1}$	Jy km s $^{-1}$	km s $^{-1}$	km s $^{-1}$	Jy km s $^{-1}$	( $''$ , $''$ , $^{\circ}$ )	( $''$ , $''$ , $^{\circ}$ )
(1)	(2)	(3)	(4)	(5)	(6)	(7)	(8)
NGC 232	905±272	461±138	380	390	–	(4.4,2.7,87)	(4.5,2.8,85)
NGC 232-2 (NGC 235)	69±22	99±30	100	500	–	(4.0,3.3,104)	(4.3,3.0,92)
NGC 232-3 (PGC 2570)	<28	<12	ND	ND	–	ND	ND
IC 1623	1655±501	632±191	270	270	230±24	(9.9,2.9,81)	(12.7,2.9,81)

Table A.5 continued

Table A.5 (*continued*)

Target Name	$S_{\text{line}}\Delta v$	$S_{\text{line}}\Delta v$	FWHM	FWHM	$S_{\text{line}}dv$	size (FWHM)	size (FWHM)
	CO (4–3)	[C I] (1–0)	CO (4–3)	[C I] (1–0)	CO (1–0)	CO (4–3)	[C I] (1–0)
	Jy km s <sup>−1</sup>	Jy km s <sup>−1</sup>	km s <sup>−1</sup>	km s <sup>−1</sup>	Jy km s <sup>−1</sup>	( <sup>''</sup> , <sup>''</sup> , <sup>°</sup> )	( <sup>''</sup> , <sup>''</sup> , <sup>°</sup> )
(1)	(2)	(3)	(4)	(5)	(6)	(7)	(8)
UGC 02982	–	187±58	–	280	289±72	–	(7.5,4.0,108)
NGC 1614	1481±447 ([1710,2410])	549±167 ([505,1080])	250	250	106±26	(4.6,4.0,58)	(4.5,4.1,68)
IRAS F05189-2524	221±67	83±25	150	230	103±20	(4.8,2.5,106)	(3.9,2.2,88)
IRAS 09022-3615	780±235	274±83	420	340	–	(4.9,2.5,84)	(3.9,2.6,91)
IRAS F09111-1007	226±69	183±55	180	170	–	(3.9,2.6,123)	(4.3,3.1,85)
NGC 3110	456±140	246±78	240	ND	277±55	(6.0,4.1,43)	(6.2,3.8,43)
IRAS F10565+2448	614±186	247±74	170	110	72±14	(3.9,3.3,65)	(3.8,3.0,110)
IRAS F10565+2448-2	<16	<13	ND	ND	–	ND	ND
IRAS F12112+0305	347±104	180±55	340	340	–	(4.1,3.1,76)	(4.8,3.0,65)
NGC 4418	1021±306	187±56	140	120	–	(4.2,2.6,97)	(3.6,2.6,102)
ESO 507-G070	715±221	357±107	400	440	141±28	(5.1,2.6,99)	(4.0,2.4,86)
NGC 5104	728±219	369±112	410	360	170±38	(4.0,3.3,75)	(4.1,3.3,90)
NGC 5135	1252±385 ([1850,2300])	1297±392 ([1590,1970])	100	100	526±105	(6.2,4.5,15)	(6.3,4.6,9)
IC 4280	204±68 ([536,1010])	111±36 ([69,406])	240	80	264±66	(5.4,4.3,61)	(4.9,3.5,75)
IRAS F14378-3651	190±57	71±21	180	190	–	(4.0,2.5,82)	(4.1,2.4,82)
CGCG 049-057	1079±324 ([523,959])	364±109 ([314,741])	280	250	118±23	(3.7,3.0,81)	(3.7,2.8,67)
NGC 5936	503±152 ([158,575])	192±59 ([70,426])	120	120	250±50	(4.5,3.6,86)	(4.0,3.1,83)
Arp 220	2864±895 ([2810,3530])	975±310 ([1110,1630])	370	400	602±120	(4.7,3.2,119)	(3.8,3.2,100)
NGC 5990	1188±357 ([87,553])	– ([178,680])	340	–	280±69	(20,20,0)*	–
NGC 6052	235±74 ([1030,1890])	<18 ([628,1300])	90	ND	136±33	(9.1,4.2,124)	ND
ESO 069-IG006	579±181	342±104	430	390	134±26	(5.0,3.4,148)	(4.5,3.5,133)
ESO 069-IG006-2	<17	<25	ND	ND	–	ND	ND
IRAS F17207-0014	1351±406	522±156	460	370	199±39	(3.7,2.9,103)	(3.5,3.0,84)
IRAS F18293-3413	2955±925 ([3180,3650])	1724±519 ([2100,2500])	310	300	649±130	(6.4,4.6,101)	(6.1,4.4,105)
IC 4734	970±297	764±229	230	230	232±46	(4.9,3.1,99)	(5.0,3.0,101)
IRAS 19542+1110	131±39	–	230	–	–	(4.0,2.4,111)	–
ESO 286-IG019	391±118	96±29	190	210	57±1	(3.8,2.5,100)	(3.5,2.8,118)
NGC 7130	784±240 ([1880,2610])	393±125 ([547,1080])	90	90	167±19	(3.8,3.1,75)	(5.0,3.5,5)
ESO 467-G027	121±40	<19	180	ND	146±36	(5.2,4.4,5)	ND
IRAS F22491-1808	154±46	18±6	300	190	15±3	(3.9,2.3,94)	(3.4,2.0,87)
NGC 7469	1933±585 ([2120,2590])	559±170 ([1130,1510])	240	210	206±30	(5.3,4.8,112)	(4.6,4.2,73)
ESO 148-IG002	343±105	53±16	160	120	35±7	(20,20,0)*	(20,20,0)*
NGC 7552	4896±1487 ([5410,6250])	1052±346 ([2200,2910])	140	150	543±55	(8.2,6.5,0)	(8.9,5.8,179)
NGC 7591	492±149 ([693,1390])	255±77 ([199,825])	340	280	206±41	(3.9,2.9,114)	(3.6,2.6,107)
NGC 7679	550±167 ([209,946])	<40 ([151,799])	200	ND	97±16	(8.8,7.0,111)	ND
Mrk 331	1239±373	483±147	280	310	59±11	(5.5,3.7,129)	(5.2,3.6,121)

NOTE— (1) Target names. (2) and (3) the velocity integrated flux. The SPIRE/FTS measurements are shown as ([A,B]), where A and B are the minimum and maximum values within the 3 $\sigma$  error. The SPIRE/FTS values were obtained from the study by [Kamenetzky et al. \(2016\)](#). (4) and (5), the FWHM of the spectrum shown in Figure A.1. (6) CO (1–0) velocity integrated flux density ([Kamenetzky et al. 2016](#)). (7) and (8), the source size is base on the FWHM value of the 2D Gaussian fitting by the `imfit` task. The “\*” indicates the manual aperture results (see the Section A.3).

**Table A.6.** Continuum flux density

Target Name	$S_{650}$	$S_{650}$	$S_{609}$	$S_{609}$	size (FWHM)	size (FWHM)
	ACA	SED	ACA	SED	650 $\mu m$	609 $\mu m$
	mJy	mJy	mJy	mJy	("", "", °)	("", "", °)
(1)	(2)	(3)	(4)	(5)	(6)	(7)
NGC 232	112±35	—	153±47	—	(4.5,2.7,75)	(4.5,2.5,78)
NGC 232-2 (NGC 235)	22±10	—	98±31	—	(3.6,3.0,155)	(5.1,3.4,97)
NGC 232-3 (PGC 2570)	(<33)	—	(<21)	—	—	—
IC 1623	109±38	[359,384]	153±49	[447,475]	(10.7,2.7,79)	(10.4,2.8,79)
UGC 02982	—	[340,436]	99±38	[433,551]	—	(12.1,2.7,97)
NGC 1614	148±50	[272,322]	188±63	[337,406]	(4.7,4.1,80)	(4.3,3.9,52)
IRAS F05189-2524	49±16	[71,89]	49±16	[89,110]	(4.9,2.3,110)	(3.5,2.1,102)
IRAS 09022-3615	49±18	[91,116]	88±29	[113,142]	(7,5,0)*	(7,5,0)*
IRAS F09111-1007	61±21	[142,162]	82±26	[178,196]	(4.6,2.3,86)	(3.9,2.2,99)
NGC 3110	71±25	—	(<51)	—	(5.7,3.7,65)	ND
IRAS F10565+2448	76±25	[140,147]	94±29	[172,181]	(3.6,3.4,52)	(3.6,3.0,123)
IRAS F10565+2448-2	(<21)	—	(<16)	—	—	—
IRAS F12112+0305	58±20	[73,84]	35±15	[93,104]	(3.7,2.8,62)	(3.5,2.0,67)
NGC 4418	379±114	—	402±121	—	(4.1,2.4,98)	(3.4,2.2,94)
ESO 507-G070	96±30	[191,223]	142±44	[229,277]	(4.6,2.4,101)	(3.7,2.1,92)
NGC 5104	128±41	[310,336]	160±53	[367,409]	(4.6,3.8,74)	(4.3,3.5,72)
NGC 5135	295±94	[681,730]	351±107	[849,900]	(5.6,4.8,67)	(5.5,4.0,39)
IC 4280	(<33)	[418,462]	152±57	[514,566]	—	(8.3,5.4,15)
IRAS F14378-3651	13±9	[48,62]	60±21	[59,74]	(6,6,0)*	(5.0,2.6,93)
CGCG 049-057	409±124	[470,566]	432±129	[596,708]	(3.7,2.8,87)	(3.5,2.7,84)
NGC 5936	73±28	[465,513]	70±21	[589,637]	(5.6,3.1,126)	(4.4,3.3,94)
Arp 220	1346±430	[1585,2101]	1311±435	[1746,2502]	(4.8,2.9,120)	(3.8,2.9,113)
NGC 5990	66±28	[393,424]	—	[483,525]	(3.4,2.9,173)	—
NGC 6052	(<39)	[217,235]	(<49)	[265,289]	—	ND
ESO 069-IG006	110±35	—	144±45	—	(4.7,3.5,140)	(4.5,3.6,130)
ESO 069-IG006-2	(<24)	—	(<23)	—	—	—
IRAS F17207-0014	330±99	[295,380]	350±105	[364,442]	(3.9,2.7,102)	(3.4,2.5,93)
IRAS F18293-3413	381±129	[830,1019]	556±168	[980,1227]	(6.8,4.4,109)	(5.9,3.6,113)
IC 4734	124±39	[437,520]	239±72	[522,642]	(4.1,2.7,99)	(4.2,2.7,92)
IRAS 19542+1110	34±13	[50,59]	—	[62,76]	(5.2,2.4,111)	—
ESO 286-IG019	30±10	[70,88]	32±12	[88,109]	(3.6,2.7,98)	(3.5,2.2,82)
NGC 7130	127±44	[440,489]	113±43	[544,597]	(4.3,3.2,102)	(3.3,2.6,60)
ESO 467-G027	(<39)	[296,333]	(<56)	[369,406]	—	ND
IRAS F22491-1808	30±14	—	47±15	—	(5.2,2.4,110)	(3.5,2.3,76)
NGC 7469	184±63	—	214±66	—	(5.0,4.0,124)	(5.2,3.8,95)
ESO 148-IG002	119±37	[75,89]	80±29	[96,111]	(20,20,0)*	(20,20,0)*
NGC 7552	572±175	—	1465±462	—	(8.0,5.7,146)	(8.2,5.7,174)
NGC 7591	67±41	—	110±41	—	(6.4,2.7,103)	(4.8,2.8,85)
NGC 7679	(<30)	[160,176]	(<32)	[195,215]	—	ND
Mrk 331	121±38	—	172±59	—	(4.8,3.3,139)	(4.9,2.7,138)

NOTE— (1) Target names. (2)-(5) The continuum flux density associated at 650 and 609  $\mu m$  for ACA in this work and SED fitting from infrared data. (6)-(7) The source size was base on the FWHM value of the 2D Gaussian fitting by the `imfit` task. The “\*” means the manual aperture results (see Section A.3).

**Table A.7.** Luminosity

Target Name	$L'_{\text{CO}(4-3)}$	$L'_{[\text{C I}](1-0)}$	$L_{630\mu\text{m}}$
	$10^6 \text{ K km s}^{-1} \text{ pc}^2$	$10^6 \text{ K km s}^{-1} \text{ pc}^2$	$10^{28} \text{ erg s}^{-1} \text{ Hz}^{-1}$
(1)	(2)	(3)	(4)
NGC 232	1607±484	718±216	166±52
NGC 232-2 (NGC 235)	123±40	154±48	76±26
NGC 232-3 (PGC 2570)	(<49)	(<19)	(<34)
IC 1623	2272±688	762±230	130±43
UGC 02982	—	172±53	68±27
NGC 1614	1249±377	406±124	104±35
IRAS F05189-2524	1579±481	519±158	223±73
IRAS 09022-3615	12132±3659	3744±1144	586±203
IRAS F09111-1007	2802±865	1987±598	511±169
NGC 3110	432±133	205±65	55±19
IRAS F10565+2448	4502±1369	1591±478	395±126
IRAS F10565+2448-2	(<115)	(<84)	(<88)
IRAS F12112+0305	8867±2672	4047±1252	581±218
NGC 4418	158±47	25±7	45±13
ESO 507-G070	1161±359	508±153	137±43
NGC 5104	851±256	379±115	122±40
NGC 5135	768±236	698±211	144±45
IC 4280	181±60	86±28	89±33
IRAS F14378-3651	4051±1223	1329±405	407±168
CGCG 049-057	594±178	175±53	173±52
NGC 5936	293±88	98±30	31±11
Arp 220	3168±991	946±301	1068±348
NGC 5990	634±190	—	29±12
NGC 6052	195±61	<13	<26
ESO 069-IG006	5029±1575	2612±796	684±217
ESO 069-IG006-2	(<147)	(<189)	(<130)
IRAS F17207-0014	9751±2934	3308±993	1555±468
IRAS F18293-3413	3289±1029	1684±507	380±120
IC 4734	784±239	541±162	108±33
IRAS 19542+1110	2271±688	—	—
ESO 286-IG019	2848±862	618±190	144±51
NGC 7130	680±208	299±95	76±27
ESO 467-G027	123±41	<16	<35
IRAS F22491-1808	4559±1383	473±155	541±212
NGC 7469	1713±519	434±132	129±42
ESO 148-IG002	2718±832	370±117	495±163
NGC 7552	437±132	82±27	69±21
NGC 7591	448±135	203±62	59±27
NGC 7679	540±164	<34	<22
Mrk 331	1429±431	488±149	123±40

NOTE— (1) Target names. (2) and (3)  $L'_{\text{line}}$  (equation 7) for CO (4–3) and [C I] (1–0), respectively.  
 (4) The specific luminosity in the rest frame 630  $\mu\text{m}$  in equation (8).



Table A.8. Ratios

Target Name	$L_{[\text{Cl}](1-0)}/L_{\text{CO}(4-3)}$	$L_{630\mu\text{m}}/L'_{[\text{Cl}](1-0)}$	$L_{630\mu\text{m}}/L'_{\text{CO}(4-3)}$	$L'_{[\text{Cl}](1-0)}/L'_{\text{CO}(1-0)}$
	$10^{20} \text{ erg s}^{-1} \text{ Hz}^{-1} (\text{K km s}^{-1} \text{ pc}^2)^{-1}$	$10^{20} \text{ erg s}^{-1} \text{ Hz}^{-1} (\text{K km s}^{-1} \text{ pc}^2)^{-1}$	$10^{20} \text{ erg s}^{-1} \text{ Hz}^{-1} (\text{K km s}^{-1} \text{ pc}^2)^{-1}$	
(1)	(2)	(3)	(4)	(5)
NGC 232	0.54±0.23	23±10	10±5	—
NGC 232-2 (NGC 235)	1.51±0.69	49±23	61±30	—
NGC 232-3 (PGC 2570)	ND	ND	ND	—
IC 1623	0.41±0.17	17±8	6±3	0.15±0.05
UGC 02982	—	40±20	—	0.04±0.01
NGC 1614	0.4±0.17	26±12	8±4	0.28±0.11
IRAS F05189-2524	0.4±0.17	43±19	14±6	0.04±0.02
IRAS 09022-3615	0.38±0.16	16±7	5±2	—
IRAS F09111-1007	0.86±0.37	26±12	18±8	—
NGC 3110	0.58±0.26	27±13	13±6	0.05±0.02
IRAS F10565+2448	0.43±0.18	25±11	9±4	0.19±0.07
IRAS F10565+2448-2	ND	ND	ND	—
IRAS F12112+0305	0.56±0.24	14±7	7±3	—
NGC 4418	0.2±0.08	180±77	29±12	—
ESO 507-G070	0.53±0.23	27±12	12±5	0.14±0.05
NGC 5104	0.54±0.23	32±14	14±6	0.12±0.05
NGC 5135	1.11±0.48	21±9	19±8	0.14±0.05
IC 4280	0.58±0.27	104±52	50±25	0.02±0.01
IRAS F14378-3651	0.4±0.17	31±16	10±5	—
CGCG 049-057	0.36±0.15	99±42	29±12	0.17±0.06
NGC 5936	0.41±0.18	32±15	11±5	0.04±0.02
Arp 220	0.36±0.16	113±51	34±15	0.09±0.03
NGC 5990	—	—	5±2	—
NGC 6052	<0.08	ND	<14	<0.007
ESO 069-IG006	0.63±0.28	26±12	14±6	0.14±0.05
ESO 069-IG006-2	ND	ND	ND	—
IRAS F17207-0014	0.41±0.18	47±20	16±7	0.14±0.05
IRAS F18293-3413	0.62±0.27	23±10	12±5	0.15±0.05
IC 4734	0.84±0.36	20±9	14±6	0.18±0.07
IRAS 19542+1110	—	—	—	—
ESO 286-IG019	0.26±0.11	23±11	5±2	0.09±0.03
NGC 7130	0.54±0.24	26±12	11±5	0.13±0.04
ESO 467-G027	<0.16	ND	<29	<0.007
IRAS F22491-1808	0.13±0.06	114±58	12±6	0.07±0.03
NGC 7469	0.31±0.13	30±13	8±3	0.15±0.05
ESO 148-IG002	0.17±0.07	134±61	18±8	0.08±0.03
NGC 7552	0.23±0.1	84±38	16±7	0.11±0.04
NGC 7591	0.55±0.24	29±16	13±7	0.07±0.02
NGC 7679	<0.08	ND	<4	<0.022
Mrk 331	0.42±0.18	25±11	9±4	0.45±0.16

NOTE— (1) Target names. (2)-(5) Ratio between luminosity.

**Table A.9.** Molecular gas mass

Target Name	$M_{\text{H2}}$	$M_{\text{H2}}$	$M_{\text{H2}}$	$M_{\text{H2}}$
	[C I] (1–0)	cont	CO(4–3)	CO(1–0)
	$10^7 M_{\odot}$	$10^7 M_{\odot}$	$10^7 M_{\odot}$	$10^7 M_{\odot}$
(1)	(2)	(3)	(4)	(5)
NGC 232	464±139	670±209	435±131	–
NGC 232-2 (NGC 235)	99±31	306±108	33±10	–
NGC 232-3 (PGC 2570)	(<12)	(<137)	(<13)	–
IC 1623	492±148	523±174	615±186	404±42
UGC 02982	111±34	276±108	–	388±97
NGC 1614	262±80	419±142	338±102	114±28
IRAS F05189-2524	335±102	898±296	427±130	938±187
IRAS 09022-3615	2419±739	2363±818	3284±990	–
IRAS F09111-1007	1284±386	2058±681	758±234	–
NGC 3110	132±42	223±80	117±36	336±67
IRAS F10565+2448	1028±309	1593±509	1219±370	682±136
IRAS F10565+2448-2	(<54)	(<355)	(<31)	–
IRAS F12112+0305	2615±809	2343±878	2401±723	–
NGC 4418	16±4	184±55	42±12	–
ESO 507-G070	328±99	555±174	314±97	292±58
NGC 5104	244±74	492±162	230±69	254±57
NGC 5135	451±136	583±181	208±63	413±82
IC 4280	55±18	361±136	49±16	299±74
IRAS F14378-3651	859±261	1641±677	1096±331	–
CGCG 049-057	113±34	699±211	160±48	83±16
NGC 5936	63±19	126±44	79±24	186±37
Arp 220	611±195	4305±1403	858±268	852±169
NGC 5990	–	118±50	171±51	191±47
NGC 6052	<8	<108	52±16	144±35
ESO 069-IG006	1688±514	2757±874	1361±426	1488±297
ESO 069-IG006-2	(<122)	(<524)	(<40)	–
IRAS F17207-0014	2137±641	6264±1888	2640±794	1837±368
IRAS F18293-3413	1088±327	1530±485	890±278	924±185
IC 4734	349±105	435±133	212±64	239±48
IRAS 19542+1110	–	–	615±186	–
ESO 286-IG019	399±123	580±207	771±233	536±10
NGC 7130	193±61	308±112	184±56	185±21
ESO 467-G027	<10	<142	33±11	189±47
IRAS F22491-1808	306±100	2181±854	1234±374	573±114
NGC 7469	280±85	523±170	463±140	233±34
ESO 148-IG002	239±76	1995±660	736±225	354±71
NGC 7552	53±17	280±87	118±35	62±6
NGC 7591	131±40	238±111	121±36	240±48
NGC 7679	<22	<90	146±44	122±20
Mrk 331	315±96	495±163	386±116	87±17

NOTE— (1) Target names. (2)–(4) Molecular gas mass inferred from [C I] (1–0), dust continuum, CO (4–3), and CO (1–0), respectively (See Section A.4).

## A.3. Notes for individual galaxies

**NGC 232, NGC 235, and PGC 2570:** NGC 232 interacts with NGC 235, which is located at  $\sim 53$  kpc northeast, with a velocity offset of approximately  $-123 \text{ km s}^{-1}$  (Larson et al. 2016; Espada et al. 2018). In addition, NGC 235 had a minor interaction pair (PGC 2570). In NGC 232 and

NGC 235, CO (4–3), [C I] (1–0), and dust continuum were detected. In NGC 235, CO (4–3) emission was detected only at the blue-shifted components (approximately  $-250 \text{ km s}^{-1}$  with a systematic velocity of approximately  $-123 \text{ km s}^{-1}$ ). Conversely, the [C I] (1–0) emission has a double

peak in both the red- and blue-shifted components.

**IC 1623 (VV 114):** The FoV centers do not match between CO (4–3) and [C I] (1–0) observations due to artificial mistakes when preparing the observation plans.

**UGC 2982:** CO (4–3) was not fully observed owing to the ALMA schedule.

**IRAS F05189-2524:** [C I] (1–0) emission was at the edge of the spectral window.

**IRAS 09022-3615:** Because the continuum maps are noisy, the “imfit” task does not work correctly. We manually chose a flux aperture of  $7'' \times 5''$  for the continuum photometries.

**IRAS F09111-1007:** [C I] (1–0) emission was at the edge of the spectral window.

**NGC 3110:** The 490GHz continuum emission associated with [C I] (1–0) was not detected due to poor observation conditions but a 460 GHz continuum associated with CO(4-3) was detected. This is due to the sky conditions during the observation.

**IRAS F10565+2448:** IRAS F10565+2448 consists of two colliding galaxies. In the main large galaxy, CO (4–3), [C I] (1–0), and dust continuum were detected. In the smaller pair galaxy (IRAS F10565+2448-2), emission were not detected. [C I] (1–0) emission was observed at the edge of the spectral window.

**NGC 4418:** The red-shifted emission associated with the [C I] (1–0) emission line is probably fake because of the bad atmospheric window.

**IC 4280:** Both CO (4–3) and [C I] (1–0) lines were detected. The continuum associated with [C I] (1–0) observation is detected, and the “imfit” shows that spatially extended structure (the FWHM of  $8''.3 \times 5''.4$ ) with the continuum flux density of  $152 \pm 57$  mJy. Because the extended structure is marginal ( $S/N \sim 3$ ), this flux density may be the upper limit of the continuum flux density. However, the continuum emission associated with CO (4–3) emission was not detected, and the upper limit was  $< 33$  mJy. The reason for the gap between  $650\mu\text{m}$  and  $609\mu\text{m}$  flux density by ACA is not clear; it is probably due to bad transmissivity around continuum emission. For this galaxy, the missing flux is difficult to determine. For example,  $S_{\text{CO}(4-3)}\Delta v = 361 \pm 74$  Jy km s $^{-1}$  for ACA

and  $S_{\text{CO}(4-3)}\Delta v = [531, 1010]$  Jy km s $^{-1}$  for SPIRE and  $S_{[\text{C I}](1-0)}\Delta v = 166 \pm 34$  Jy km s $^{-1}$  for ACA and  $S_{[\text{C I}](1-0)}\Delta v = [69, 406]$  Jy km s $^{-1}$  for SPIRE. This means that the line missions do not have a significant missing flux. However, in the case of continuum emission,  $S_{650} = 152 \pm 57$  mJy for ACA but  $S_{650} = [514, 566]$  mJy from SED fitting, suggesting that RF is approximately 30%. In the case of  $S_{609}$ , the situation is worsened. This means that only continuum emission has a large missing flux in this system, probably suggesting a different spatial structure between gas and dust. However, we do not know the reason for the large difference in RF for line and continuum emission.

**IRAS F14378-3651:** Both CO (4–3) and [C I] (1–0) lines were detected. Because the continuum maps associated with CO (4–3) emission are noisy, the “imfit” task does not work correctly. We manually chose a flux aperture of  $6'' \times 6''$  for the photometry.

**CGCG 049-057:** The spurious emission is observed at the edge of the [C I] (1–0) spectral windows but it does not affect the measurements.

**NGC 5936:** The spectral of the frequency  $> 486$  GHz is significantly affected by the bad sky but it does not affect the [C I] (1–0) measurements.

**Arp 220:** Owing to the strong emission line, the `tclean` process cannot remove all the sidelobe components, and some components are seen in the residual maps. Therefore, moments 1 and 2 maps have uncertain structures. However, the contribution of these structures to the total integrated intensity was negligible.

**NGC 5990:** The [C I] (1–0) observation has issues in calibration, and the data are declared as “QA2 semipass”. Because CO (4–3) emission is spatially extended, single 2D Gaussian fitting by the “imfit” underestimates the flux. Therefore, we used the  $20''$  aperture to measure the CO (4–3) continuum.

**NGC 6052:** While CO (4–3) was clearly detected, [C I] (1–0) was not detected. The details are discussed in [Michiyama et al. \(2020\)](#).

**ESO 069-IG006:** ESO 069-IG00 consists of two colliding galaxies. In the main galaxy, CO (4–3), [C I] (1–0), and dust continuum were detected. In the smaller pair galaxy (ESO 069-IG00-2), emission were not detected. [C I] (1–0) emission was observed at the edge of the spectral window.

**IRAS F17207-0014:** [C I] (1–0) emission was observed at the edge of the spectral window.

**IRAS 19542+1110:** Both CO (4–3) and [C I] (1–0) observations were done, but [C I] (1–0) emission is outside of the spectral window. The CO (4–3) and dust continuum peak consists with optical peak.

**NGC 7130:** An uncertain structure is seen in the souther part of the [C I] (1–0) emission. However, we use flux derived from the “imfit” which ignores the southern emission.

**ESO 467-G027:** CO (4–3) was robustly detected but the red-shifted components may have been outside of the spectral window. The [C I] (1–0) was marginally detected in the nuclear region. However, the measured flux is less than the upper limits, and we assume [C I] (1–0) to be non-detection. This galaxy is a candidate of C<sup>0</sup>-poor/CO-rich galaxy but the data quality is not very good; the upper limit of  $L'_{[C I](1-0)}/L'_{CO(4-3)}$  is  $> 0.1$ .

**IRAS F22491-1808:** In CO (4–3) observation, the spectral window does not fully cover the entire line emission. While the S/N of the spectrum spatially integrated within the FoV is not robust, a smaller aperture can boost the S/N.

**NGC 7469:** No comments regarding the ACA observations.

**ESO 148-IG002:** A double peak was observed in both CO (4–3) and [C I] (1–0) emission. The uncertain north-south structure is observed in the continuum emission. This could be due to the calibration issues, but the clear reason is unknown. Further sensitive observations are required. To avoid the uncertainty, we use  $20'' \times 20''$  aperture to measure continuum flux density.

**NGC 7679:** While CO (4–3) was clearly detected, [C I] (1–0) was not detected.

#### A.4. Molecular gas mass

- We use the CO (1–0) to H<sub>2</sub> conversion factor of  $\alpha_{CO} = 0.8 M_{\odot}(\text{K km s}^{-1} \text{ pc}^2)^{-1}$ , which is typically applied for U/LIRGs (Bolatto et al. 2013).

$$\begin{aligned} M_{H_2}^{CO(1-0)} &= \alpha_{CO} L'_{CO(1-0)} \\ \alpha_{CO} &= 0.8 \end{aligned} \quad (\text{A1})$$

- Papadopoulos & Greve (2004); Bothwell et al. (2017) provided an equation to calculate the total

molecular gas mass from [C I] (1–0) luminosity:

$$\begin{aligned} M_{H_2}^{[C I](1-0)} &= \alpha_{[C I]} L'_{[C I](1-0)} \\ \alpha_{[C I]} &= 6.5 \left( \frac{R_{CI}}{5 \times 10^{-5}} \right)^{-1} \\ &\times \left( \frac{A_{10}}{7.93 \times 10^{-8} \text{ s}^{-1}} \right)^{-1} \left( \frac{Q_{10}}{0.4} \right)^{-1}, \quad (\text{A2}) \end{aligned}$$

where  $R_{CI}$  is the C<sup>0</sup>/H<sub>2</sub> abundance ratio,  $A_{10}$  is the Einstein A coefficient, and  $Q_{10}$  is the excitation factor. Jiao et al. (2017) showed that  $Q_{10}$  varies from 0.35 – 0.45, assuming that the molecular gas density is  $10^3 - 10^4 \text{ cm}^{-3}$  and the kinematic temperature is 20–40 K. Papadopoulos & Greve (2004) considered that the typical  $R_{CI}$  is  $3 \times 10^{-5}$ , but a relatively higher value ( $5 \times 10^{-5}$ ) was considered in starburst galaxy M82 (Bothwell et al. 2017). In addition, a relatively smaller value ( $1.6 - 1.9 \times 10^{-5}$ ) was reported for main-sequence galaxies at  $z=1-2$  (Valentino et al. 2018). We use  $\alpha_{[C I]} = 6.5 M_{\odot}(\text{K km s}^{-1} \text{ pc}^2)^{-1}$ , assuming that  $Q_{10} = 0.4$ ,  $R_{[C I]} = 5 \times 10^{-5}$ , and  $A_{10} = 7.93 \times 10^{-8}$ . We note that the determination of  $\alpha_{[C I]}$  is uncertain because of the unknown  $R_{CI}$ ,  $Q_{10}$ , and  $A_{10}$ . For example, Crocker et al. (2019) modeled the [C I] and CO line emission using large-velocity gradient models and demonstrated that  $\alpha_{[C I]} = 7.3 M_{\odot}(\text{K km s}^{-1} \text{ pc}^2)^{-1}$  and  $\alpha_{CO} = 0.9 M_{\odot}(\text{K km s}^{-1} \text{ pc}^2)^{-1}$  using the Herschel SPIRE results. In the case of Israel (2020), the [C I] to H<sub>2</sub> conversion factor at the central molecular zone in galaxies is calculated as  $X([C I]) = (9 \pm 2) \times 10^{19} \text{ cm}^{-2}/\text{K km s}^{-1}$ , which corresponds to  $\alpha_{[C I]} \sim 2 M_{\odot}(\text{K km s}^{-1} \text{ pc}^2)^{-1}$  (they also calculate CO (1–0) to H<sub>2</sub> conversion factor  $X(\text{CO}) = (1.9 \pm 0.2) \times 10^{19} \text{ cm}^{-2}/\text{K km s}^{-1}$ , which is a factor of ten below the standard solar neighborhood Milky Way factor of  $\sim 2 \times 10^{20} \text{ cm}^{-2}/\text{K km s}^{-1}$ ). Conversely, a relatively higher value of  $\alpha_{[C I]} \sim 18.8 M_{\odot}(\text{K km s}^{-1} \text{ pc}^2)^{-1}$  and  $\alpha_{CO} \sim 3.0 M_{\odot}(\text{K km s}^{-1} \text{ pc}^2)^{-1}$  was calculated by Dunne et al. (2021). We note that determining the conversion factor is outside the scope of this study. We fixed the conversion factor and attempted to understand the scatter among each method.

- Scoville et al. (2016) derived an empirical mass to luminosity ratio between 850  $\mu\text{m}$  specific luminosity to molecular gas mass ( $L_{\nu(850\mu\text{m})}/M_{\text{mol}} = 6.7\text{e}+19 M_{\odot}^{-1}(\text{erg s}^{-1} \text{ Hz}^{-1}) = \alpha_{850\mu\text{m}}$ , where  $M_{\text{mol}} = 1.36 M_{H_2}$ ) based on the comparison between CO (1–0) single-dish observations, SPIRE

photometry, and SCUBA 850  $\mu\text{m}$  photometry. We note that this  $L_{\nu(850\mu\text{m})}/M_{\text{mol}}$  was experimentally estimated by assuming a single standard Galactic  $\alpha_{\text{CO}}$ . We convert our observed continuum flux density  $S_\nu$  into  $M_{\text{H}_2}$  using the formulation of [Scoville et al. \(2016\)](#)

$$M_{\text{H}_2}^{\text{cont}} = 1.78 S_\nu (1+z)^{-4.8} \left( \frac{\nu_{850\mu\text{m}}}{\nu_{\text{obs}}} \right)^{3.8} \quad (\text{A3})$$

$$\times \left( \frac{6.7 \times 10^{19}}{\alpha_{850}} \right) \frac{\Gamma_{\text{RJ}}(T_{\text{dust}}, \nu_{850\mu\text{m}}, 0)}{\Gamma_{\text{RJ}}(T_{\text{dust}}, \nu_{\text{obs}}, z)}$$

$$\times D_{\text{L}}^2 \times \frac{M_{\text{H}_2}}{M_{\text{mol}}} [10^{10} M_\odot].$$

We note that the unit of  $S_\nu$  is mJy and the unit of  $D_{\text{L}}$  is Gpc in this equation. We assume the dust temperature of  $T_{\text{dust}} = 25$  K for simple analyses.

- From CO (4–3), we use

$$M_{\text{H}_2}^{\text{CO(4-3)}} = \alpha_{\text{CO}} L'_{\text{CO(4-3)}} / \left( \frac{L'_{\text{CO(4-3)}}}{L'_{\text{CO(1-0)}}} \right)_{\text{med}}$$

$$\left( \frac{L'_{\text{CO(4-3)}}}{L'_{\text{CO(1-0)}}} \right)_{\text{med}} = 0.3 \quad (\text{A4})$$

where  $\left( \frac{L'_{\text{CO(4-3)}}}{L'_{\text{CO(1-0)}}} \right)_{\text{med}}$  is the median value of  $L'_{\text{CO(4-3)}}/L'_{\text{CO(1-0)}}$ . However, the ratio varies for each galaxy population. For example,  $L'_{\text{CO(4-3)}}/L'_{\text{CO(1-0)}}$  is  $\sim 0.1$  in low excitation galaxies like the Milky Way ([Fixsen et al. 1999](#)),  $\sim 0.8$  in starbursts like M82 ([Weiß et al. 2005](#)), and  $\sim 0.8$  in some high- $z$  SMGs ([Carilli & Walter 2013](#); [Casey et al. 2014](#)).